2022

Development Of A Ph-Sensitive Probe For In Vivo Cerenkov Imaging Of The Tumor Microenvironment

Andrea Estefania Rodríguez-Ríos
University of Pennsylvania

Development Of A Ph-Sensitive Probe For In Vivo Cerenkov Imaging Of The Tumor Microenvironment

Abstract

Acidity in the tumor microenvironment (TME) is related to invasion, metastasis, and chemotherapeutic resistance, all of which are contributors to poor prognoses in cancer patients. In this thesis, we propose the application of Cerenkov radiation as a tool for imaging pH in vivo through the measurement of Selective Bandwidth Quenching (SBQ) and Cerenkov Radiation Energy Transfer (CRET) in triple negative human breast cancer models MDA-MB-231 and 4175-Luc+. To test the hypothesis that SBQ and CRET signals could provide measurements of TME pH in vivo, a Cerenkov-active molecule, NFbD, was conjugated and chelated with 68Ga. Cerenkov imaging was performed with NFbD-Ga in vitro to construct pH titration curves, later used to interpolate in vivo Cerenkov pH values. In vivo Cerenkov imaging was performed on athymic nude mice bearing 4175-Luc+ triple negative breast cancer xenografts after intratumoral injections of NFbD-Ga (40 μCi). CRET values obtained from in vivo Cerenkov imaging were used to estimate TME pH values, which were validated by 31P Magnetic Resonance Spectroscopy (31P MRS) following i.p. injection of 3-APP. Tissue scattering, and absorption effects were evaluated in vitro with tissue phantoms. NFbD maintained its pH-sensitivity after conjugation (pKa= 7.8, λex= 599 nm, λem= 669 nm at pH 9). SBQ and CRET were observed in vitro inter-and intramolecularly, at 600 nm and 700 nm, respectively. SBQ and CRET were also observed in vivo. CRET measurements following intratumoral injections of NFbD-Ga yielded a tumor pHCerenkov= 6.90 ± 0.16, 31P-MRS on the same tumors yielded a pHMRS= 6.92 ± 0.04. Chicken tissue phantoms provided insight on tissue attenuation effects, showing that 1 mm of tissue can attenuate 64% of the Cerenkov signal, in the absence of naphthofluorescein and further attenuation to 17% is achieved with the addition of naphthofluorescein. The synthesis and development of this Cerenkov-active, pH sensitive probe for the determination of TME pH provided detectable CRET signals in vivo, allowing Cerenkov to be used as a potential technique for non-invasive pH imaging.

Degree Type

Dissertation

Degree Name

Doctor of Philosophy (PhD)

Graduate Group

Pharmacology

First Advisor

E. James Delikatny

Subject Categories

Oncology | Pharmacology

DEVELOPMENT OF A pH-SENSITIVE PROBE FOR *IN VIVO* CERENKOV IMAGING OF THE TUMOR MICROENVIRONMENT

Andrea Estefania Rodríguez Ríos

A DISSERTATION

in

Pharmacology

Presented to the Faculties of the University of Pennsylvania

In

Partial Fulfillment of the Requirements for the

Degree of Doctor of Philosophy

2022

Supervisor of Dissertation

E. James Delikatny, Ph.D.
Research Professor of Radiology

Graduate Group Chairperson

Julie Blendy, Ph.D.
Professor of Pharmacology

Dissertation Committee:
Ian Blair, Ph.D. - A. N. Richards Professor of Pharmacology
Sean Carlin, Ph.D. - Professor of Radiology
Robert Mach, Ph.D. - Britton Chance Professor of Radiology
Andrew Tsourkas, Ph.D. – Professor of Bioengineering

ACKNOWLEDGMENTS

I would like to thank my advisor Dr. Jim Delikatny, for being supportive and kind. Thank you for all your patience and for believing in myself when I did not. I am so grateful for the opportunity to have been part of your lab. I would also like to thank my second mentor, Dr. Alejandro Arroyo. Thank you for all your guidance, history lessons and dad jokes. Most importantly, thank you for your friendship. You were and will always be an inspiration to me. Thank you to Dr. Anatoliy Popov, who was always eager to help in any way he could. I noticed Tolya, as we call him, hums songs while he works. I don't think he knows that this small thing brought me a lot of joy and peace when I was in lab. To Sofya Osharovich and Michael Hart, who were colleagues and became friends. I am grateful for all our discussions, related to science and to life. I learned so much from you both and I'm glad we were able to share this experience and be there for each other.

I would like to thank Eric Blankemeyer, Dr. Karl Ploessl and Dr. David Alexoff for helping me with every experiment that required radioactivity. Without their help, this project would not have been possible. I am beyond grateful.

I would like to thank Dr. Sharon Lee, Dr. Prashanth Padakanti, Lawrence Toto, Rahul Poria and Dr. Alexander Schmidt, from the Cyclotron facility, for their insight, guidance, and training. I would also like to thank Dr. Kavindra Nath, for being kind enough to collaborate with us on some of our seminal experiments.

I would like to thank those friends who helped me miss Puerto Rico a bit less, especially Dr. Arnaldo Díaz, Kiara Berríos, José Gorbea and Ambar Cajigas. Thank you

for your company throughout this journey. I am so thankful for your love, support, and friendship.

I would like to take some lines to thank my dear psychologist, Dr. Downie. This might be an odd addition to some, but Dr. Downie brought me “back to life” as I say half-jokingly, more than once during these years. I am immensely grateful for your care and advice. I have learned so much about life and about myself, thanks to you. Thank you for being understanding and empathetic, and for helping me see that all the colors of the spectrum apply to life too. I was lucky to be under your care.

I would like to thank my best friends, mis nenas: Fabiola and Yemaiza, for being my truest cheerleaders. You make all of life’s journeys an adventure worth pursuing. Thank you for more than a decade of friendship. Doing life with you is a blessing.

I would like to thank my husband, Daniel, for his love, support, and encouragement. When I had trouble writing, he would tell me to just put down a word or a sentence, because doing a little was better than doing nothing at all. Those sentences turned into grant proposals, abstracts, presentations, and this thesis. Thank you for helping me move forward in all facets of life and for bringing me love, joy and laughter.

Finally, I would like to thank my parents Marie and Valentino. Words fail to describe how much they mean to me. They have been there every second of every day, loving me and cheering me on. We went on this journey together and we were faced with many challenges, the first of which was living 1,585 miles apart. Mami, thank you for all your care packages, visits, and phone calls. I am so grateful to have such a loving and caring Mamá. Papi, thank you for adopting me even before a judge called it so. I am honored to close this chapter of my life with your last name. Gracias.

ABSTRACT

DEVELOPMENT OF A PH-SENSITIVE PROBE FOR *IN VIVO* CERENKOV IMAGING OF THE TUMOR MICROENVIRONMENT

Andrea E. Rodríguez Ríos

E. James Delikatny

Acidity in the tumor microenvironment (TME) is related to invasion, metastasis, and chemotherapeutic resistance, all of which are contributors to poor prognoses in cancer patients. In this thesis, we propose the application of Cerenkov radiation as a tool for imaging pH in vivo through the measurement of Selective Bandwidth Quenching (SBQ) and Cerenkov Radiation Energy Transfer (CRET) in triple negative human breast cancer models MDA-MB-231 and 4175-Luc+. To test the hypothesis that SBQ and CRET signals could provide measurements of TME pH in vivo, a Cerenkov-active molecule, NFbD, was conjugated and chelated with ^{68}Ga. Cerenkov imaging was performed with NFbD-Ga *in vitro* to construct pH titration curves, later used to interpolate in vivo Cerenkov pH values. *In vivo* Cerenkov imaging was performed on athymic nude mice bearing 4175-Luc+ triple negative breast cancer xenografts after intratumoral injections of NFbD-Ga (40 μCi). CRET values obtained from *in vivo* Cerenkov imaging were used to estimate TME pH values, which were validated by ^{31}P Magnetic Resonance Spectroscopy (^{31}P MRS) following i.p. injection of 3-APP. Tissue scattering, and absorption effects were evaluated *in vitro* with tissue phantoms. NFbD maintained its pH-sensitivity after conjugation (pK_a= 7.8, λ_{ex}= 599 nm, λ_{em}= 669 nm at pH 9). SBQ and CRET were observed *in vitro* inter-and intramolecularly, at 600 nm and 700 nm,

respectively. SBQ and CRET were also observed *in vivo*. CRET measurements following intratumoral injections of NFbD-Ga yielded a tumor $pH_{Cerenkov}$= 6.90 ± 0.16, ^{31}P-MRS on the same tumors yielded a pH_{MRS}= 6.92 ± 0.04. Chicken tissue phantoms provided insight on tissue attenuation effects, showing that 1 mm of tissue can attenuate 64% of the Cerenkov signal, in the absence of naphthofluorescein and further attenuation to 17% is achieved with the addition of naphthofluorescein. The synthesis and development of this Cerenkov-active, pH sensitive probe for the determination of TME pH provided detectable CRET signals *in vivo*, allowing Cerenkov to be used as a potential technique for non-invasive pH imaging.

TABLE OF CONTENTS

LIST OF ILLUSTRATIONS

LIST OF EQUATIONS

LIST OF ABBREVIATIONS

3-APP	3-Aminopropylphosphonate
ATCC	American Type Culture Collection
ATP	Adenosine Triphosphate
BCA	Bicinchonic Acid
CCD	Charged-Couple Device
CEST	Chemical Exchange Saturation Transfer
CHCA	α-Cyano-4-hydroxycinnamic acid
Ci	Curie
CLI	Cerenkov Luminescence Imaging
CNF-SE	Carboxynaphthofluorescein Succinimidyl Ester
CO2	Carbon Dioxide
CRET	Cerenkov Radiation Energy Transfer
DCM	Dichloromethane
DMEM	Dulbecco's Modified Eagle Medium
DOTA	1,4,7,10-Tetraazacyclododecane-1,4,7-tris(acetic acid)-10-(4-aminobutyl)acetamide
ER	Estrogen Receptor
ECM	Extracellular Matrix
FBS	Fetal Bovine Serum

FDG	Fluorodeoxyglucose
FOV	Field of View
GLUT1	Glucose Transporter Isoform 1
HER2	Human Epidermal Growth Receptor 2
HIF	Hypoxia-Inducible Factor
HK	Hexokinase
HPLC	High Performance Liquid Chromatography
IgG	Immunoglobulin G
II	India Ink
IL	Intralipid
ISIS	Image Selected In vivo Spectroscopy
IT	Intratumorally
IV	Intravenously
keV	Kilo Electron Volt
LDH	Lactate Dehydrogenase
LDHA	Lactate Dehydrogenase A
LDHi	Lactate Dehydrogenase inhibitor
MALDI	Matrix-Assisted Laser Desorption/Ionization
MCT4	Monocarboxylate Transporter 4
MMP	Matrix Metalloproteinases

MRI	Magnetic Resonance Imaging
MRS	Magnetic Resonance Spectroscopy
MTT	3-(4,5-Dimethylthiazol-2-yl)-2,5-diphenyl-2H-tetrazolium bromide
NF	Naphthofluorescein
NFbD	Naphthofluorescein-butyl-DOTA
NIR	Near Infrared
NMR	Nuclear Magnetic Resonance
OXPHOS	Oxidative Phosphorylation
P/S	Penicilin/Streptomycin
PBS	Phosphate Buffered Saline
PET	Positron Emission Tomography
PR	Progesterone Receptor
PRESS	Point Resolved Spectroscopy Sequence
ROI	Region of Interest
SBQ	Selective Bandwidth Quenching
SCIFI	Secondary Cerenkov Induced Fluorescence Imaging
TEA	Triethylamine
TME	Tumor Microenvironment
TNBC	Triple Negative Breast Cancer

ULAR	University Laboratory Animal Resources

Chapter 1

Introduction

1.1 Breast Cancer

Breast cancer is the most common cancer affecting women. In 2022, the American Cancer Society estimates that almost 288,000 new cases of invasive breast cancer will be diagnosed and around 43,000 women will die from this disease (2022a). Breast cancer is considered curable when it is *in situ*, contained within the breast tissue or only spread to axillary lymph nodes. Metastatic breast cancer is treatable, however, it is considered incurable with currently available therapeutic options (Harbeck et al., 2019). Treatment of metastatic breast cancer mainly focuses on prolonging survival and improving quality of life.

Breast cancer is considered a heterogeneous disease and can be classified by the presence of estrogen receptor (ER), progesterone receptor (PR), human epidermal growth receptor 2 (HER2) or by the absence of these receptors, as presented in Figure 1.1 (Costa et al., 2020). When breast cancer is ER, PR and HER2 negative, it is referred to as Triple Negative Breast Cancer (TNBC), which is aggressive and lacks targeted therapies (Anders and Carey, 2008). Tissue samples resected from breast cancer patients are tested for these markers to provide a framework for therapeutics and next steps (Harbeck et al., 2019). Understanding disease pathology and its molecular mechanism aids in the development of new and better therapeutics, enhancing patient prognosis.

	ER	PR	HER2	Ki-67	Notes
Luminal A	+ +/−	+/− +	−	Low	• Low-grade cancer and with the best prognosis
Luminal B	+ +/−	+/− +	+ −	Any High	• Higher expression of proliferation-associated genes • Worse prognosis than Luminal A
HER2 Enriched	−	−	+	High	• Faster growth and worse prognosis than Luminal cancers • Successfully treated with HER2 targeted therapies
Triple-Negative A ≡ Basal-like	−	−	−	High	• More common in women with BRCA1 mutations • Enriched in cytokeratins and integrins • Associated with metastasis and poor prognosis
Triple-Negative B ≡ Normal-like	−	−	−	Low	• Claudin-low cancers, overexpressing genes associated with tumor invasiveness and aggressivity

Figure 1.1. Molecular classification of breast cancer. Table adapted from (Costa et al., 2020) shows breast cancer markers used to classify breast cancers clinically. Ki-67 is a proliferation marker.

In vitro and *in vivo* models of breast cancer have been developed to mimic the microenvironment and molecular characteristics of this disease. In research studies, breast cancer cell lines are chosen , according to the aims of the study, to elucidate specific information based on their metabolic profiles (Kao et al., 2009). The most common breast cancer cell lines used in research are MCF7 (ER+, PR+), T47D (ER+, PR+) and MDA-MB-231(TNBC) (Dai et al., 2017), all of which were originally isolated from patients (2022b; 2022c; 2022f).

MDA-MB-231 is a metastatic TNBC that is used to model late-stage breast cancer. This cell line grows well *in vitro* and produces breast cancer tumor xenografts when implanted in mice (Welsh, 2013). In 2005, Andy Minn et al. developed a metastatic variant of MDA-MB-231 by injecting MDA-MB-231 cells into the tail vein of immunodeficient mice, harvesting lung metastases, expanding them in tissue culture and injecting them again (Minn et al., 2005). This process was repeated several times,

followed by transfection with luciferase and GFP to produce the bioluminescent cell line 4175-Luc+. Both MDA-MB-231 and its metastatic variant 4175-Luc+ cell lines are currently used as *in vitro* and *in vivo* breast cancer models in our lab (Arlauckas et al., 2017; Arroyo et al., 2019).

1.2 Hallmarks of Cancer

Hanahan and Weinberg described the Hallmarks of Cancer in 2000, six categorized processes that occur in the development of all cancerous tissues, allowing malignant cells to survive, proliferate and spread (Hanahan and Weinberg, 2000). These hallmarks include: sustaining proliferative signaling, evading growth suppressors, activating invasion and metastasis, enabling replicative immortality, inducing angiogenesis, and resisting cell death (Figure 1.2.A). The Hallmarks of Cancer were revised in 2011, and four additional hallmarks were included, also called "emerging hallmarks", which include: genome instability and mutation, deregulating cellular energetics, avoiding immune destruction and tumor-promoting inflammation (Hanahan and Weinberg, 2011), described in Figure 1.2.B. Identifying and conducting research

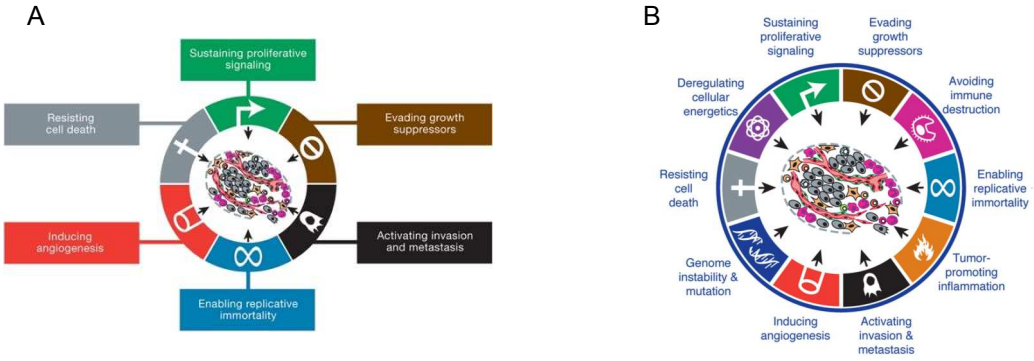

Figure 1.2 Hallmarks of Cancer. Adapted from (Hanahan and Weinberg, 2011; Hanahan and Weinberg, 2000). *A.* Scheme showing the original Hallmarks of Cancer. *B.* Scheme including the original Hallmarks of Cancer and Emerging hallmarks.

addressing these processes have aided in the development of novel targeted therapeutics (Senga and Grose, 2021).

Hanahan and Weinberg correctly predicted the further evolution of the Hallmarks of Cancer, due to advances in research. In 2021, Sasi Senga and Richard Grose proposed including four additional hallmarks to the ones already defined. These are as follows: dedifferentiation and transdifferentiation, epigenetic dysregulation, altered microbiome and altered neuronal signaling (Senga and Grose, 2021). Some of these new hallmarks were also addressed by Hanahan himself in his latest publication "Hallmarks of Cancer: New Dimensions" (Hanahan, 2022). He refers to dedifferentiation and transdifferentiation as "unlocking phenotypic plasticity", epigenetic dysregulation is referred to as "nonmutational epigenetic reprogramming", and touches on altered microbiome in terms of "polymorphic microbiomes". Hanahan includes an additional hallmark, where he proposes cell senescence as a characteristic that promotes malignant progression.

1.3 Deregulation of Cellular energetics

The deregulation of cellular energetics was described as an emerging hallmark of cancer in 2011, and is now considered a core hallmark (Hanahan, 2022). Malignant cells undergo dysregulated division, which requires altering the way in which these cells obtain energy to sustain their fast proliferative rates. Cancer cells do this by increasing their rates of glycolysis, even when there is oxygen available. This phenomenon is called the Warburg Effect and has been described as aerobic glycolysis (Warburg et al., 1927) .

Relying on glycolysis for energetic production is not as efficient as oxidative phosphorylation (OXPHOS). Glycolysis produces 2 molecules of ATP, while OXPHOS produces up to 36 ATP molecules (Vander Heiden et al., 2009). Cells compensate by upregulating glucose transporters, such as glucose transporter isoform 1 (GLUT1), to increase glycolytic rates (Barbosa and Martel, 2020; Ooi and Gomperts, 2015). Increased glycolytic rates also occur due to hypoxic conditions frequently observed in tumors, which activates the transcription factor hypoxia-inducible factor (HIF). Activation of HIF can upregulate GLUT1, hexokinase (HK), lactate dehydrogenase A (LDHA) and monocarboxylate transporter 4 (MCT4) (Kroemer and Pouyssegur, 2008). As previously mentioned, GLUT1 is a glucose transporter that aids in glucose transfer into the cytosol, from the extracellular milieu. Hexokinase catalyzes the first step of glycolysis, phosphorylating glucose and converting it into glucose-6-phosphate (Mathupala et al., 2006). LDHA catalyzes the conversion from pyruvate to lactate, in the last step of glycolysis (Jafary et al., 2019), while MCT4 releases lactate from the cells with a proton as a counterion (Contreras-Baeza et al., 2019).

Although inefficient, glycolysis with a high enough rate can produce an amount of ATP that exceeds the amount of ATP produced from oxidative phosphorylation (DeBerardinis et al., 2008). In addition, glycolysis provides cells with byproducts required for biosynthesis, such as ribose sugars (nucleotides), glycerol and citrate (lipids), and NADPH (pentose phosphate pathway), aiding in cell proliferation (DeBerardinis et al., 2008). It is important to note that oxidative phosphorylation still occurs in cancer cells. It is possible that the function of the Warburg effect is to allow cells to maintain a

steady stream of glycolytic intermediates to be used for biosynthesis (DeBerardinis and Chandel, 2020). This machinery benefits cancer cells by playing a role in both bioenergetics and biosynthesis. LDHA and MCT4 upregulation, for example, produce and excrete lactate, respectively, that will become part of the tumor microenvironment. Lactate had been previously considered a glycolytic byproduct that is excreted from cells as waste (Vander Heiden et al., 2009), but emerging evidence has shown that lactate can be consumed by stromal cells in the tumor microenvironment to regenerate pyruvate as a source of energy (Pérez-Tomás and Pérez-Guillén, 2020), resulting in a symbiotic interaction between glycolytic tumor cells and oxidative stromal cells (Rattigan et al., 2012).

1.4 pH modulation in tumors

Increased glycolytic rates due to the deregulation of cellular energetics result in increased lactate production. This lactate accumulates in the cytosol and must be excreted from the cell to prevent intracellular acidification and to maintain the glycolytic gradient (Pérez-Tomás and Pérez-Guillén, 2020). Lactate secretion occurs through MCTs, particularly MCT4, which is a H+ coupled symporter (Contreras-Baeza et al., 2019). This means that lactate excretion occurs with a proton as a counter ion, whose extracellular accumulation increases acidity in the TME. Cancer cells overexpress other enzymes in addition to MCTs that are able to transport protons to the extracellular milieu as well, such as H^+-ATPases and the Na^+-H^+ exchanger NHE1, which also contribute to acidification (Webb et al., 2011). Conversion of CO_2 to H^+ and HCO_3 by carbonic

anhydrases, also plays a role in increased extracellular acidity (Pavlova and Thompson, 2016).

Physiological pH is highly controlled and maintained at around pH 7.4, whereas local pH in the TME ranges from 6.5 to 6.9 (Estrella et al., 2013). This decrease in pH results in a "reverse pH gradient" in which the extracellular pH is lower than the intracellular pH in the TME (Webb et al., 2011). Since many cellular processes are dependent on pH, TME acidification has important implications in cancer progression and therapeutic options (Pérez-Tomás and Pérez-Guillén, 2020).

Increased acidity of the TME aids in the immune escape of malignant cells and proteolytic degradation of the extracellular matrix (Pérez-Tomás and Pérez-Guillén, 2020). Acidic TME is able to suppress some immune cells such as cytolytic T cells (Hashim et al., 2011). In addition, matrix metalloproteinases (MMP) and cathepsins are examples of enzymes whose function is to degrade the extracellular matrix, facilitating tumor cell invasion and subsequent cell migration from the tumor to other sites of the body. These enzymes are activated by a lower pH and their activity fosters invasion and metastasis (Hashim et al., 2011).

Low pH in the TME is also related to chemotherapeutic resistance through various mechanisms. Firstly, acidic conditions correlate with increased expression of the efflux transporter p-glycoprotein, which transports foreign substances out of cells (Hamaguchi et al., 2020). Inhibition of this transporter has improved efficacy of some

chemotherapeutics (Abumanhal-Masarweh et al., 2019; Thews et al., 2006). Second, decreased pH in the TME can have an "ion trapping" effect on weak base chemotherapeutics, such as doxorubicin, which become ionized extracellularly and become cell impermeable, reducing chemotherapeutic efficiency (Gerweck et al., 2006; Wojtkowiak et al., 2011). Increased acidity can also cause changes to the expression of target proteins, decreasing therapeutic efficiency (Kolosenko et al., 2017).

1.5 Optical Imaging

Optical imaging is a non-invasive technique in which visible light is detected for the identification of molecular markers *in vivo* and *in vitro*. It mainly refers to light detection through fluorescence or bioluminescence (Fokong et al., 2014). Its use has been widely beneficial in pre-clinical and clinical settings.

Fluorescence occurs when an excited molecule transitions from an excited state to a relaxed state, emitting light. Fluorescent molecules, also called fluorophores, absorb light in the visible range, and emit some of this light at a longer, less energetic wavelength (Luker and Luker, 2008). Not all excited molecules emit light when reaching the ground state. Most undergo a non-radiative vibrational relaxation, with only a small portion of excited molecules emitting light. The efficiency of this process, the fraction of excited molecules releasing photons during relaxation, is referred to as the quantum yield (Birks, 1976). A simplified schematic showing these transitions can be found in the Jablonski-Perrin diagram in Figure 1.3, as well as the original Jablonski diagram can also be found (Jablonski, 1933; Valeur and Berberan-Santos, 2011).

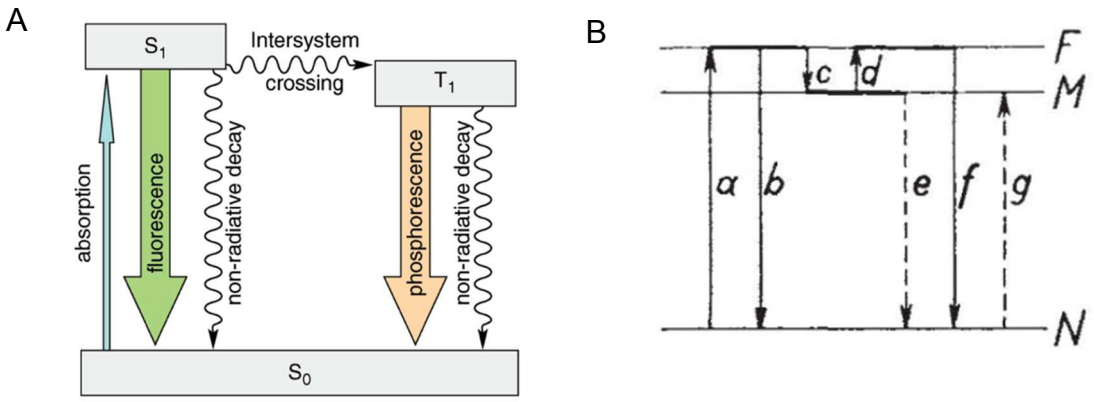

Figure 1.3 Jablonski diagram for energetic transitions. Adapted from (Jablonski, 1933; Valeur and Berberan-Santos, 2011). *A.* Scheme showing a simplified Jablonski-Perrin diagram. *B.* Jablonski diagram from his 1933 Nature publication.

Fluorescence imaging relies on this principle to obtain information on tissues, after light from an exogenous or endogenous fluorophore is detected. This imaging can be *direct imaging* in which fluorophores are administered to target a specific biological marker or *indirect imaging*, where transgenic specimens express a fluorescent marker (Ntziachristos, 2006; Soubret and Ntziachristos, 2006). Direct imaging fluorophores can be activated by a biological or metabolic response in tissue, such as enzyme cleavage (Chiorazzo et al., 2015) or pH changes (Arroyo et al., 2019).

Although beneficial due to its wide range of applications, fluorescence imaging is challenging in tissues because of tissue absorption and scattering, which occur on the visible range, and because of autofluorescence of biomolecules such as flavins and lipofuscins (Alves et al., 2017; Li et al., 2020). These problems have been partially circumvented through the use of fluorophores in the near-infrared region (NIR) ranging

from 650 nm to 1700 nm, which include the NIR-I and NIR-II region, where tissue is essentially transparent (Feng et al., 2021; Li et al., 2020).

Light detection through bioluminescence occurs when photons are produced after a chemical reaction. For bioluminescence imaging, the most commonly used substrate is the oxidation of luciferin by luciferase (Arranz and Ripoll, 2015; Ottobrini et al., 2016). Bioluminescence is highly sensitive and does not require an external excitation source, minimizing autofluorescence *in vivo* and increasing signal to noise ratio (Liu et al., 2011).

An additional modality of optical imaging which does not require an external excitation source is Cerenkov Imaging, also referred to as Cerenkov Luminescence. Cerenkov imaging bridges the gap between optical and nuclear techniques and present several advantages for pre-clinical and clinical applications, such as radiation therapy tracking. Cerenkov imaging can even be coupled with chromophores (Czupryna et al., 2015) or fluorophores, creating a true multimodal imaging approach (Arroyo et al., 2019; Das et al., 2014; Ottobrini et al., 2016).

1.6 Naphthofluorescein and Derivatives

Naphthofluorescein is a pH-dependent naphthoxanthene fluorophore that has a maximum absorption λ_{abs}= 595 nm and a maximum emission of λ_{em}= 660 nm, which falls within the NIR-I range (Lavis and Raines, 2008). The pK_a of naphthofluorescein has been reported to be 8.0 (Lavis, 2022; Lavis and Raines, 2008) and 7.6 (2022d; Chiorazzo, 2016) which is slightly above the physiological range for *in vivo* applications. 5(6)-

Carboxynaphthofluorescein is a naphthofluorescein derivative, which is also pH-dependent, with highly similar optical properties as naphthofluorescein, with a maximum absorption λ_{abs}= 572 nm and a maximum emission of λ_{em}= 668 nm and a pK_a of 7.6 (Han and Burgess, 2010).

The pH-sensitivity of carboxynaphthofluorescein, like naphthofluorescein, relies on the equilibrium between protonated and deprotonated species, as seen in Figure 1.4, and described by the Henderson-Hasselbalch equation (Po and Senozan, 2001; Radić and Prkić, 2022). The protonated species exhibits a carboxylic function in the 5(6) position, while the deprotonated species exhibits a lactone in the same position, resulting in photophysical changes. These photophysical changes allow fluorescence when the predominant species is the deprotonated molecule, which has a blue color. In acidic conditions, there is no fluorescence (Le Guern et al., 2020; Martin and Lindqvist, 1975).

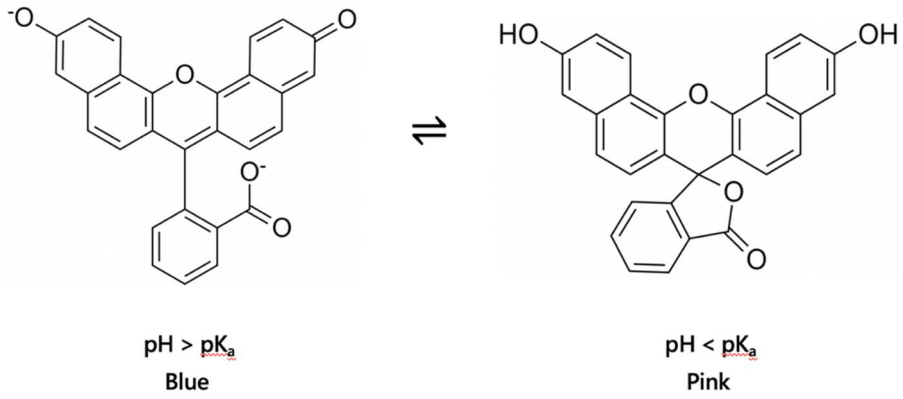

Figure 1.4 pH equilibrium of 5(6)-carboxynaphthofluorescein. 5(6)-carboxynaphthofluorescein exhibits photophysical changes based on the equilibrium between its protonated (not-fluorescent) and deprotonated species (fluorescent).

1.7 Cerenkov Radiation

Cerenkov Radiation, also spelled Cherenkov, is a phenomenon that occurs when charged particles travel faster than the speed of light in a dielectric medium (L'Annunziata, 2016). In simple terms, a charged particle, generated through the decay of a radionuclide, traveling faster than the speed of light in a specific medium is able to transfer kinetic energy to that medium, which then relaxes though the emission of light (Das et al., 2014).

Cerenkov radiation was first observed by Madame Curie in 1910, where she described a faint blue glow coming from the bottles she kept, which contained radium (Jennings, 1962). It wasn't until 1933 that this phenomenon was formally described by Pavel Cerenkov. He won the Nobel Prize in 1958, alongside Ilya Frank and Igor Tamm, who proposed the mathematical framework for Cerenkov radiation (2022e; Čerenkov, 1937; Frank and Tamm, 1937; Pratt et al., 2021). In the present day, Cerenkov radiation

may be observed by the naked eye in the pools where radioactive spent fuel is stored, which emit a blue light as seen in Figure 1.5 (radioactivity.eu.com, 2022).

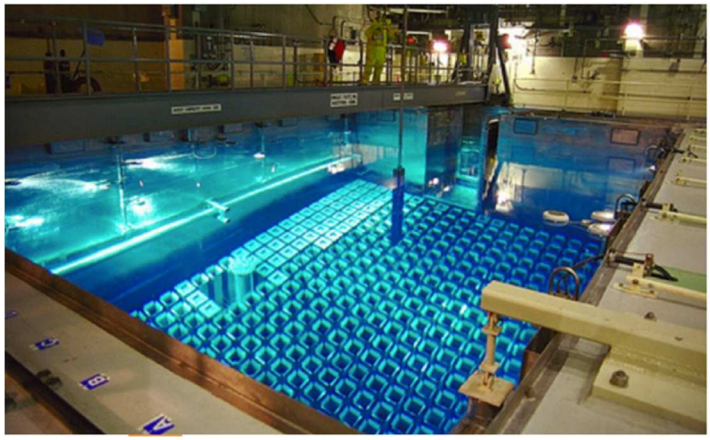

Figure 1.5 Cerenkov radiation in nuclear pool. Cerenkov radiation seen with the naked eye in a nuclear reactor pool, where radioactive spent fuel is stored. Adapted from (radioactivity.eu.com, 2022) "Radioactivity: Cherenkov Effect." from https://www.radioactivity.eu.com/site/pages/Cherenkov_Effect.htm.

Cerenkov radiation has several properties that must be described and explained. The particles that can produce Cerenkov radiation are charged subatomic particles such as high energy β^+ positrons or β^- electrons. Cerenkov radiation can also be seen from α emitters, but this radiation mainly comes from β emission from daughter radionuclides (Das et al., 2014). As mentioned before, these fast particles polarize the medium, which in turn emits photons as it undergoes relaxation. This light emission occurs in a wavefront that travels in a cone (Figure 1.6), following the Huygens construction (Das et al., 2014), with an angle described by equation 1.1. β is the velocity of the charge and *n* is the refractive index of the medium (Ciarrocchi and Belcari, 2017; Jelley, 1955).

$$\cos\theta = 1/\beta n \qquad \text{Equation 1.1}$$

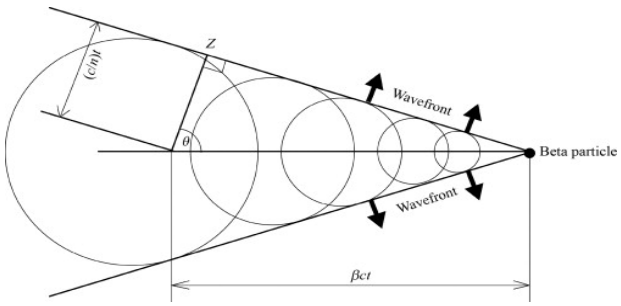

Figure 1.6 Huygens propagation of light waves. The Huygens construction can be applied to the wavefront produced by Cerenkov emission (Jennings, 1962). Adapted from (Das et al., 2014).

In Cerenkov radiation, the number of photons emitted within a spectral range is described by the Frank-Tamm formula (Equation 1.2), where α is the fine structure constant (1/137) (Daniel LJ Thorek, 2012; Frank and Tamm, 1937). This equation explains why Cerenkov radiation is blue-weighted, since its intensity is proportional to the inverse of wavelength squared. As mentioned previously, Cerenkov radiation also

$$\frac{dN}{dx} = 2\pi\alpha\left(1 - \frac{1}{\beta^2 n^2}\right)\int_{\lambda_1}^{\lambda_2}\frac{1}{\lambda^2}\,d\lambda \qquad \text{Equation 1.2}$$

has an inverse relationship to the refractive index of the medium in which the charged particles are traveling through. A larger refractive index corresponds to increased Cerenkov emission. However, for Cerenkov radiation to be produced in a medium, the traveling particles must meet the threshold energy for that medium, according to its refractive index. For example, for Cerenkov emission to occur in water (n= 1.33) the kinetic energy of the traveling particles must be at least 263 keV (threshold energy) (Beattie et al., 2012; Das et al., 2014; L'Annunziata, 2016).

Cerenkov emitters have different end point energies, or maximum kinetic energy, which relate to the probability of the Cerenkov emitters of producing enough energy to reach the threshold energy (Das et al., 2014; Mitchell et al., 2011). The efficiency of Cerenkov Radiation production can be summarized as $^{90}Y > ^{68}Ga > ^{15}O > ^{11}C > ^{124}I > ^{89}Zr > ^{18}F > ^{64}Cu$ (Thorek et al., 2012). This information aids in choice of Cerenkov emitter for specific applications.

1.8 Cerenkov imaging

Cerenkov radiation is continuous and includes the visible spectrum (Thorek et al., 2012). It can be detected with sensitive charge-couple device (CCD) cameras, allowing it to be used as an optical imaging modality. In 2009, Robertson et al. described the use of ^{18}F-FDG, a clinical PET tracer, for Cerenkov imaging (also known as Cerenkov Luminescence Imaging (CLI)), *in vivo* (Das et al., 2014; Robertson et al., 2009). The first

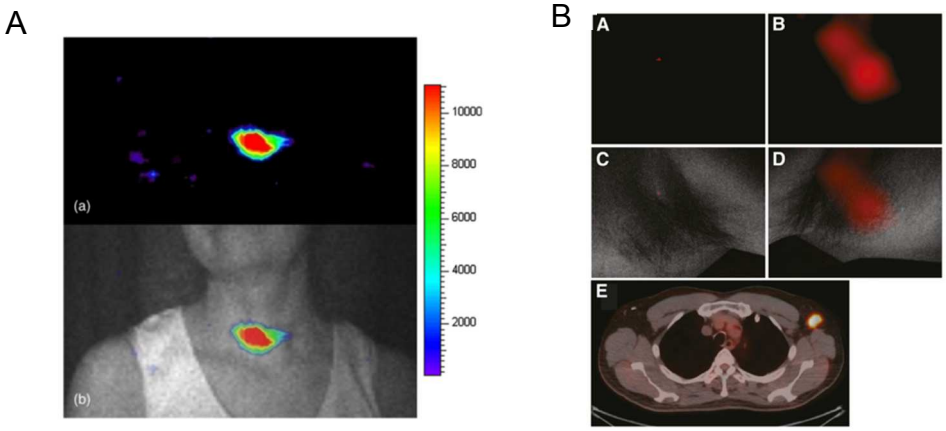

Figure 1.7 Clinical Cerenkov imaging. *A.* First human Cerenkography of patient with hyperthyroidism treated with ^{131}I. Adapted from (Spinelli et al., 2013). *B.* Cerenokv imaging of axillary lymph node malignancy in a patient with lymphoma treated with ^{18}F-FDG. Adapted from (Thorek, Riedl et al. 2014).

report of clinical use of Cerenkov imaging was in 2013, where Cerenkov was used to monitor ^{131}I in a patient being treated for hyperthyroidism, seen in Figure 1.7.A (Spinelli et al., 2013). The Grimm group also demonstrated clinical Cerenkov imaging, identifying an axillary lymph node in a patient with lymphoma treated with ^{18}F-FDG, seen in Figure 1.7.B (Thorek et al., 2014a).

Cerenkov imaging provides an avenue to visualize clinically approved radiotracers, merging nuclear imaging with optical imaging (Das et al., 2014). These radiotracers have been modified with targeting moieties, nanoparticles and small molecules for tumor identification, tumor margin delineation, and assessment of metabolic markers (Arroyo et al., 2019; Bagguley et al., 2020; Boschi et al., 2011; Czupryna et al., 2015; Holland et al., 2011; Lewis et al., 2018; Lohrmann et al., 2015; Thorek et al., 2013). This imaging modality has several advantages: it is inexpensive, high-throughput and does not require an external light source (Daniel LJ Thorek, 2012). Additionally, CLI can produce a measurable signal quickly and it is proportional to PET signal (Desvaux et al., 2018).

There are some challenges associated with CLI. The intensity of the Cerenkov signal depends on the radionuclide of choice since its endpoint energy and half-life will dictate the brightness and length of the signal. This choice must be made wisely. For example, ^{18}F has a half-life of 110 minutes, which is suitable for longer experimental procedures. On the other hand, ^{68}Ga has a half-life of only 68 minutes, which makes it suitable for shorter experimental procedures. ^{68}Ga, however, has a higher endpoint energy than ^{18}F (1899 keV and 633 keV, respectively), making the former a brighter emitter

(Ciarrocchi and Belcari, 2017; Jimenez-Mancilla et al., 2019). This is a trade-off that must be taken into account. Additionally, Cerenkov radiation produces relatively low light compared to fluorescence (Thorek et al., 2012) and it is a blue-weighted emission, which is highly absorbed by tissue (Ciarrocchi and Belcari, 2017; Soubret and Ntziachristos, 2006).

Cerenkov photons can be transferred to longer wavelengths through Cerenkov Radiation Energy Transfer (CRET) or Secondary Cerenkov Induced Fluorescence Imaging (SCIFI), minimizing attenuation effects by moving the emission to longer wavelengths where tissue is more permeable to light (Bernhard et al., 2014, 2017; Dothager et al., 2010; Thorek et al., 2013). CRET occurs when a Cerenkov emitter is coupled to a fluorophore. This fluorophore absorbs Cerenkov photons, provided by the Cerenkov emitter, and undergoes fluorescence emission at longer wavelengths. This process turns Cerenkov emitters into "internal lightbulbs", providing the fluorophores with the energy necessary to absorb and fluoresce, without the need of an external excitation source.

The first step of this process is the absorption of Cerenkov photons by the fluorophore, which results in a measurable signal attenuation. This attenuation is described as Selective Bandwidth Quenching (SBQ) and was first proposed by our lab in 2015 to obtain functional information regarding pH using chromophores as pH indicators (Czupryna et al., 2015). This attenuation is selective because it will occur at the wavelength at which the dye absorbs, and it will be based on a functional metabolic

response. For example, Czupryna et al. applied ^{18}F labeled cresol purple and phenolphthalein, to *in vitro* and *in vivo* models. These dyes showed selective attenuation at their maximum wavelengths of absorption, in response to pH (Czupryna et al., 2015). In another example, Arroyo et al. demonstrated SBQ using resazurin, which reports on redox status, absorbing and fluorescing only when it is in its reduced state (Arroyo et al., 2021). For Cerenkov signal modulation involving only SBQ, chromophores and not fluorophores should be used, to prevent photon transfer that results in CRET.

CRET has been explored to enhance signal in tissues by transferring Cerenkov photons to areas closer to the NIR window, where light is not as susceptible to tissue effects (Bernhard et al., 2017). This photon transfer will also be able to provide measurable information on a desired metabolic target, given that the correct reporter is used. In Figure 1.8, we give an example of pH dependent SBQ and CRET, adapted from (Arroyo, 2019; Arroyo et al., 2019). The spectrum in Figure 1.8.A shows the results from a Cerenkov imaging study where the average radiance signal is plotted as a function of wavelength at pH 6.4 and pH 8 for naphthofluorescein. An ^{18}F-FDG control is included. Robust SBQ is observed as a dip in the Cerenkov spectrum at 600 nm, at pH 8. CRET is observed at 700 nm, as an increase in signal at pH 8. pH dependent SBQ and CRET can be visualized directly as a change in brightness as a function of pH, as seen in Figure 1.8.B.

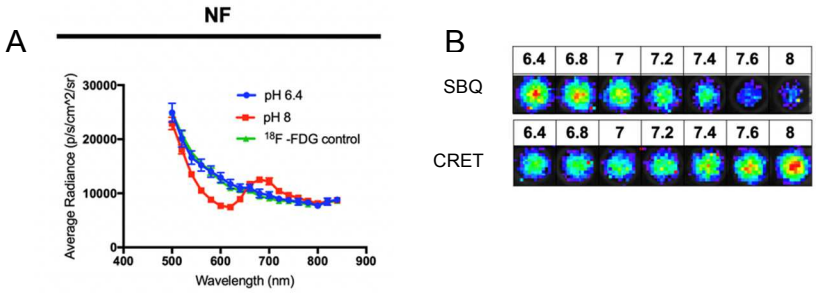

Figure 1.8. Naphthofluorescein pH dependent SBQ and CRET. *A.* Cerenkov spectra of naphthofluorescein at pH 6.4 and pH 8. ^{18}F-FDG control is included. SBQ is observed at 600 nm. CRET is observed at 700 nm. *B.* pH titration of naphthofluorescein with ^{18}F-FDG shows signal decrease as a function of pH for SBQ and signal increase as a function of pH for CRET, seen as darker and brighter wells, respectively.

1.9 Scope of thesis

The main focus of this thesis is the development and application of a Cerenkov-active pH sensitive probe that can report on tumor microenvironment pH *in vivo*. This thesis presents the continuation of methods previously explored in our lab (Arroyo et al., 2021; Arroyo et al., 2019; Czupryna et al., 2015; Kachur et al., 2017) for the application of Cerenkov imaging for pH determination. This was done by developing a molecular construct which includes ^{68}Ga, a higher-endpoint energy emitter than ^{18}F, chelated to a carboxynaphthofluorescein based conjugate.

The second aim of this thesis is to understand the particular tissue effects that play a role in the detection of pH sensitive SBQ and CRET, and how this data can be interpreted and applied to obtain accurate Cerenkov pH values. Experimental Cerenkov pH titration curves were interpolated to obtain *in vivo* pH values using CRET ratios (Dothager et al., 2010). Efforts were dedicated to elucidating whether this technique can

be accurately described as quantitative, in its current stage, and progress was done to determine depth penetration and signal contributions from our fluorophore vis-à-vis ^{68}Ga.

Cerenkov imaging provides an exciting framework within optical imaging due to its expansive potential as a pre-clinical and clinical tool. With this work, we hope to contribute to this field by providing a new application.

Chapter 2

Methods

2.1 Materials

Acetonitrile, triethylamine, trifluoroacetic acid and naphthofluorescein were purchased from Sigma-Aldrich. Dichloromethane, methanol, hydrochloric acid (1.0 N) and sodium hydroxide (0.1 N) were purchased from Fisher Scientific. Ethanol was purchased from Decon Laboratories, Inc. Millipore water was generously donated by Dr. Robert Mach. 5(6) Carboxynaphthofluorescein succinimidyl ester was purchased from Setareh Biotech. 4-Aminobutyl-DOTA was purchased from Macrocyclics.

Radioactive Gallium was obtained from the Cyclotron Facility at the University of Pennsylvania, and later from Five Eleven Pharma, Inc.

MDA-MB-231 cell lines were purchased from the American Type Culture Collection (ATCC). 4175-Luc+ cell lines were generously donated by Dr. Andy Minn (Minn et al. 2005).

LDHA and LDHB rabbit polyclonal antibodies were purchased from AbCam. IRDye ® 800 CW goat anti-rabbit IgG was purchased from LI-COR. Hoechst 33342 was purchased from Invitrogen. Athymic NCR nu/nu 01B74 were purchased from Charles River, Production. Lactate Dehydrogenase Inhibitor (LDHi), GSK 2837808A was purchased from TOCRIS.

2.2 High Performance Liquid Chromatography (HPLC)

Purification of non-radioactive compounds synthesized in-house was performed on a Waters Alliance e2695 HPLC with a reverse-phase column (Phenomenex Synergy 4µ Hydro-RP 80 A 10x250 mm). The product was resuspended in 1 mL 50% acetonitrile-water solution and injected into the HPLC. Elution was completed with a 95%-5% solution of water-acetonitrile with 0.1% trifluoroacetic acid for 40 minutes with UV absorption detection at 230 nm and fluorescence detection at 600 nm/660 nm. The peak of interest was collected from minute 30 to minute 36. Acetonitrile was removed from the collected fraction by rotary evaporation or by nitrogen gas. The remaining volume was lyophilized for 24 hours using a Labconco FreeZone 4.5 lyophilized.

2.3 ^{1}H Nuclear Magnetic Resonance (NMR) Spectroscopy

Proton NMR Spectroscopy was performed to characterize NFbD after synthesis. This was done on a Bruker DMX 500 by dissolving 10 mg of NFbD in 600 µL of deuterated water buffered to pH 14 using NaOD. NMR spectra were acquired using the TopSpin software. After running a standard (D_2O), the sample was inserted into the NMR and locked in. Shimming on this instrument was automatic. Proton MR spectra were collected using the pulse sequence zgpr following acquisition parameters: relaxation delay (D1): 6, number of scans: 128. Line broadening of 0.5 Hz was performed before Fourier transformation. Data was analyzed using MestreNova Software (Mestrelab Research), using the residual water solvent peak as reference.

2.4 Mass Spectrometry

Mass spectrometric analysis of synthesized products was performed using a Bruker MALDI-TOF at the Mass Spectrometry Facility of the Department of Chemistry. A 10 mg/mL solution of alpha-cyano-4-hydroxycinnamic acid (CHCA) mixed with a 50:50 solution of acetonitrile and water and 0.1% trifluoroacetic acid was prepared. Samples were placed on an MTP AnchorChip TM 600/384 TF MALDI target by adding 1 µL of CHCA solution to the plate. Once the CHCA was dry, 1 µL of sample was added to the dried CHCA and allowed to dry. Finally, a last 1 µL of CHCA was added on top of the sample. This was mixed and let dry to form crystals. The target was inserted into a Bruker Ultraflex MALDI-TOF/TOF mass spectrometer and irradiated by a Smartbeam II laser at 200 Hz.

2.5 Cell Culture

MDA-MDA-231, a triple negative breast cancer cell line, and 4175-Luc+, a metastatic variant of MDA-MB-231 generously donated by Dr. Andy Minn, were cultured with Dulbecco's Modified Eagle Medium (DMEM) supplemented with 10% fetal bovine serum (FBS) (GE HyClone Laboratories), 1% penicillin-streptomycin (P/S) (Mediatech) and 1% L-glutamine (Mediatech). In addition, for 4175-Luc+ cell culture, 5 µg/mL blasticidin (Invitrogen) was added for selection of the luciferase transfected cells. Cells were maintained in a humidity-controlled incubator at 37º C under 95% air:5% CO_2. Cell passage was done when confluence reached 90% by aspirating media, washing with

Phosphate Buffered Saline (PBS), adding 1 mL of 0.25% Trypsin (Thermo Fisher), and neutralizing with culture media. Cell passage was done in a 1:10 ratio.

2.6 Cell Metabolism Experiments

To evaluate cell acidification, MDA-MB-231 cells and 4175-Luc+ cells were plated at $5x10^4$, $1x10^5$ and $5x10^5$ cells per well in 3 separate 6-well plates in 3 mL DMEM. These cells were incubated for 5 days, media was collected, and media pH was measured with an Orion Star A111 (Thermo Fisher) pH meter.

To evaluate cell acidification in phenol red free media, MDA-MB-231 cells and 4175-Luc+ cells were plated at $5x10^5$ cells per well in separate 6-well plates using 3 mL regular DMEM. After allowing for adhesion, media was aspirated from each well, cells were washed with PBS, and 3 mL Seahorse XF Media (Agilent) was added, and cells were incubated for 24 hours. The Seahorse XF Media was prepared with 10% FBS, 1% P/S, 10% L-glutamine, 5 mM HEPES and either no glucose, low glucose (1 g/L) or high glucose (4.5 g/L). Media from each condition was collected and pH was measured using an Orion Star A111 pH meter.

To evaluate cell acidification in unbuffered media, MDA-MB-231 cells and 4175-Luc+ cells were plated at 1 $x10^6$ cells per well in separate 6-well plates using 3 mL regular DMEM. After allowing for adhesion, media was aspirated from each well, cells were washed with PBS, and 3 mL Seahorse XF Media was added. The Seahorse XF Media was prepared with 10% FBS, 1% P/S, and 25 mM glucose. Cells were allowed to

incubate in Seahorse XF Media for 24 hours and then media was collected to measure pH using an Orion Star A111 pH meter. This media was later injected into a YSI 2300 STAT PLUS Glucose & L-Lactate Analyzer to evaluate glucose and lactate levels.

To evaluate the effects of LDH inhibitors on glucose and lactate concentration, 4175-Luc+ cells were plated in triplicate at $3x10^5$ cells per well in 4 mL of regular DMEM in a 6-well plate. Cells were left to adhere overnight; media was aspirated and cells were treated with 2-(3-phenyl-5-(trifluoromethyl)-1H-pyrazol-1-yl)thiazole-4-carboxylic acid (Rai et al. 2017) or GSK 2837808A at 50 μM. Media was collected every hour for 6 hours and after 24 hours. Collected media was injected into a YSI2950 immobilized enzyme analyzer (YSI Life Sciences) to evaluate glucose consumption and lactate production.

2.7 Cellular Uptake Experiments

2.7.1 Fluorescence Microscopy

4175-Luc+ cells were plated in triplicate in 1 mL regular DMEM at $1x10^4$ cells per well in a 24-well plate. After 48 hours, and 3 hours before analysis, the media was changed to phenol red free, full DMEM media. 681 μL of 8.1 μM NFbD was added to the cells to a final concentration of 3.3 μM and incubated for 45 minutes. Hoechst stain was used as a positive control, with a 3.5 μM final concentration. After treatment, the media was removed, wells were rinsed with PBS and 1 mL fresh media was added. For microscopy the ThermoFisher EVOS FL Auto 2 at the Cell & Developmental Biology (CDB) Microscopy Core was used. NFbD was visualized under the Cy5 LED light cube, and

Hoechst was visualized under the DAPI LED light cube. Images were obtained with light at 25, exposure at 0.015 seconds and a gain of 1.0.

2.7.2 Absorbance Spectroscopy

4175-Luc+ cells were plated in triplicate in regular DMEM at 1 x10^4 cells per well in a 96-well plate. Cells were allowed to adhere for 24 hours; media was aspirated, and cells were washed with PBS. After washing, cells were treated with a 4 μM, 2.8 μM or 1.6 μM NFbD and incubated for 30 minutes. The medium was then aspirated, and cells were washed with 0.5 mL of PBS twice. Cells were treated with 100 μL Triton X-100 0.5% or PBS for 5 or 10 minutes. Absorbance was measured at 600 nm.

2.8 Cell Survival Experiments

To evaluate effects of NFbD on MDA-MB-231 and 4175-Luc+ cell survival, cells were plated in triplicate at 7.5x10^4 cells per well in 96-well plates. A 0.5 mM stock solution of NFbD was prepared in PBS. 5 μM, 1 μM 500 nM, 50 nM, 10 nM or 5 nM solutions in media were prepared from the 0.5 mM stock to treat MDA-MB-231 or 4175-Luc+ cells. Cell survival was evaluated through a thiazolyl blue tetrazolium bromide (MTT) assay.

To evaluate effects of LDH inhibitors on 4175-Luc+ cell survival, cells were plated in triplicate at 1x10^4 cells per well in regular DMEM in a 96-well plate. Cells were left to adhere overnight; media was aspirated, and cells were treated with 2-(3-phenyl-5-(trifluoromethyl)-1H-pyrazol-1-yl) thiazole-4-carboxylic acid (Rai et al. 2017) or GSK 2837808A. A 1 mM solution of each LDHi was prepared in 1% DMSO dissolved in PBS.

Cells were treated with 200 μM, 100 μM, 50 μM, 25 μM and 12.5 μM and cell survival was evaluated through a Cell Titer Glo assay.

2.9 In vivo *Experiments*

2.9.1 Anesthesia

Prior to *in vivo* experiments, female Athymic NCR nu/nu mice were placed inside an induction chamber and were anesthetized using 4% isoflurane. Mice were kept under anesthesia at 2% isoflurane during optical and nuclear imaging experiments.

2.9.2 Euthanasia

Mice were placed in a container and put inside a closed CO_2 chamber for 4 minutes. The chamber and CO_2 systems were provided by the University Laboratory Animal Resources (ULAR). Euthanasia was confirmed by cervical dislocation.

2.9.3 Tumor Inoculation

MDA-MB-231 or 4175-Luc+ cells were grown in regular DMEM until confluent and counted after trypsinization. The cells were centrifuged, media were aspirated and cells were resuspended in PBS at a concentration of 2 $x10^7$ cells/ml. Matrigel ® (Corning) was added in a 1:1 volume ratio to the cell solution. 100 μL of the final solution containing $1x10^6$ cells was injected subcutaneously into either the right shoulder flank or the right thigh of the mice. Mice were monitored to assess health and tumor growth. MDA-MB-231 tumors were palpable after 3 weeks, while 4175-Luc+ tumors were palpable after 1-2 weeks post inoculation.

2.9.4 Intratumoral Injections

Mice were anesthetized, the area was sterilized with an alcohol wipe (70% isopropanol) and the specified solutions were injected into the middle of the tumor. The plunger of the syringe was pushed slowly to prevent effects from the interstitial pressure of the tumor, such as treatment release due to back pressure.

2.9.5 Intravenous Injections

Mice were anesthetized, the tail was sterilized with an alcohol wipe (70% isopropanol) and the specified solutions were injected into the tail vein. To aid with injection, the tail was covered with warm compresses for a few seconds, causing vasodilation. The plunger on the syringe was pushed carefully, when no resistance was felt, to guarantee intravenous delivery.

2.9.6 ^{31}Phosphorus-Magnetic Resonance Spectroscopy (MRS)

Magnetic Resonance spectroscopy was performed in collaboration with Dr. Kavindra Nath. These experiments were done on a 9.4 T/31 cm horizontal bore Bruker system. *In vivo* ^{31}P MR spectra (MRS) were acquired with a custom-built dual-frequency (^{1}H/^{31}P) slotted-tube resonator (10 mm in diameter). To monitor mouse heart rate and core body temperature, sub-dermal needle electrodes and a rectal thermistor were placed in the mouse. The animal's core body temperature was maintained at 37 ± 1°C. This was done by blowing warm air into the bore of the magnet during the scan with heating controlled by a thermal regulator system. A respiration pillow was placed under the thorax to

monitor respiration. A 26-gauge intraperitoneal catheter was inserted into the peritoneum prior to placing the mouse in the magnet, for 3-APP injection.

The magnet was shimmed until the ^{1}H water line width of the subcutaneous tumor reached 60–70 Hz. A point resolved spectroscopy (PRESS) sequence was obtained with the following parameters: TR of 2 sec; TE of 20 ms; number of averages equal to 4. A scan time of 8 sec, was used to shim a tumor voxel of 250-300 mm^3 size to 30-40 Hz line width. ^{31}P MR spectra were obtained using an ISIS (Image Selected In vivo Spectroscopy) sequence on this volume. The ISIS sequence employed slice-selective hyperbolic secant inversion pulses with the following parameters: length of 0.59 ms; 256 scans with a 7 μs radiofrequency pulse width at 200 watts, corresponding to approximately a 90º flip angle; acquisition band width of 7978.2 Hz; 512 acquisition points; TR of 4 s; total acquisition time of 7 minutes 4 seconds.

Following acquisition of baseline ^{31}P MR spectra, 3-aminopropylphosphoninc acid (APP; 300 mg/ml) was injected intraperitoneally through the intraperitoneal catheter without removing the animal from the magnet. ^{31}P spectra were collected again as described above, 20 minutes after 3-APP injection.

2.9.7 Dynamic Positron Emission Tomography Scan

NFbD-^{68}Ga (up to 1.48 MBq), was injected intravenously via tail vein into mice bearing 4175-Luc+ breast cancer tumor xenografts. Mice were imaged dynamically in the

Molecubes β-Cube for 2 hours. This was followed by a CT-Scan that was run for 3 minutes using the Molecubes X-Cube (Ghent, Belgium).

PET images (24 frames at 5 minutes per frame) were reconstructed into 192 x 192 x 384 (x,y,z) slices with 0.4 mm voxels with frame lengths of 24 x 300 seconds. All corrections were applied using a manufacturer supplied reconstruction program. CT images (50 kVp and 100 μA) were reconstructed into 200 x 200 x 550 (x,y,z) slices with 0.2 mm voxels with a manufacturer supplied reconstruction program.

2.10 Protein Immunoblot

To determine LDHA and LDHB expression *ex vivo,* MDA-MB-231 and 4175-Luc+ tumors were excised from euthanized mice when they were around 1 cm^3. These tumors were weighed, flash frozen and homogenized using 1 mL of RIPA buffer per 100 mg of tissue in a Potter-Elvehjem Tissue Homogenizer. Homogenized samples were subjected to 3 freeze/thaw cycles using liquid nitrogen and a 37º C water bath, respectively. Finally, the samples were sonicated for 15 minutes, let sit on ice for 15 minutes and centrifuged for 10 minutes at 14,000 g. The supernatant from this step (cell lysate) was saved and protein concentration measured using a bicinchonic acid (BCA) protein assay kit (Pierce). Samples were diluted in a 1:1 ratio with Laemmli Loading Buffer (Bio-rad), containing 5% 2-mercaptoethanol and then heated at 95º C for 5 minutes. 10% Mini-PROTEAN SDS-PAGE gels (Bio-rad) were loaded with 30 μL of each sample and electrophoresis was ran at 300V for 18 minutes on a PowerPac Basic electrophoresis system (Bio-rad). This gel was transferred to a nitrocellulose membrane (0.45 μm) (Invitrogen) using a

Trans-Blot SD Semi-Dry Transfer Cell (Bio-rad). Ponceau S solution 0.1% w/v in 5% v/v acetic acid (Sigma) was used to confirm the transfer and the gel was then washed with PBS. The membranes were blocked using Odyssey Blocking Buffer (LI-COR) for one hour and then incubated overnight with primary antibodies (LDHA, LDHB or β-tubulin (Abcam)). Primary antibodies were diluted 1:1,000 in a blocking buffer solution with 0.2% Tween 20. After 24 hours, the membranes were washed and secondary antibodies, diluted 1:15,000 in a blocking buffer solution with 0.2% Tween 20 (Sigma), were added (goat anti-rabbit conjugated with IRDye ® 800 CW from LI-COR). Membranes were imaged using the LI-COR Odyssey ® Clx Imaging System and analyzed with ImageStudio Lite.

2.11 Optical Imaging

Optical imaging studies were performed using the PerkinElmer IVIS Spectrum. For phantom studies, 96-black well plates with a flat clear bottom were used. Plates were placed carefully inside the IVIS system, aligned with the field of view outline (seen as a green light inside the chamber) in order to aid in grid ROI measurement. The LivingImage software for the IVIS Spectrum, the system was initialized, and then the Cerenkov imaging parameter was chosen in the Imaging Wizard, followed by "Spectral Unmixing". For our purposes, the following bandwidth emission filters were chosen: 580 nm, 600 nm, 680 nm, 700 nm and 840 nm. Images were acquired with a Binning of 8 (M), Field of View (FOV) of 13.1, f1 and exposure of 60 seconds.

For *in vivo* experiments, mice were placed on the heated stage inside the chamber, after intratumoral injections of the appropriate solutions. Each mouse was placed on its side with the tumor facing the camera, and ensuring that their snout was comfortable and securely inside the nose cones for continued anesthesia. Acquisition parameters were as following: Binning: 8 (M), FOV: 22.3, f1 and exposure time of 300 seconds. The images were acquired using the same bandwidth filters as with the plate experiments.

2.12 Determination of Tissue Effects

To determine the effects of tissue on Cerenkov imaging, several tissue phantom models were explored.

A black well, clear bottom 96-well plate was prepared with varying concentrations of intralipid and/or India ink, 40 μM napthofluorescein, 50 μL ^{68}Ga (~30 μCi/well) and 10 μL NaOH (1 N) to keep the conditions basic. Saline was added to each well to obtain a 250 μL volume per well. Conditions were plated in triplicate. This plate was imaged in the IVIS Spectrum and analyzed using LivingImage Software.

A black well, clear bottom 96-well plate was prepared with 240 μM naphthofluorescein, 10 μL NaOH (1 N), 50 μL ^{68}Ga and saline (added to achieve a final volume of 250 μL). Conditions were plated in triplicate, with no naphthofluorescein as a control. This plate was imaged in the IVIS Spectrum, then bologna slices (ACME) 2.5 mm, 3 mm or 6 mm thick were placed on top of the wells, to determine tissue effects and depth penetration. Imaging was repeated after bologna slices were placed on top of the wells.

A black well, clear bottom 96-well plate was prepared with 240 μM naphthofluorescein, 50 μL ^{68}Ga and citrate/borate/phosphate buffer (0.05 M) at pH 4, 7.4 or 8, added to achieve a final volume of 250 μL. Conditions were plated in triplicate. This plate was imaged in the IVIS Spectrum, and then tumor or skin slices excised from mice bearing 4175-Luc+ tumors were placed on top of the wells containing activity. Tumor slices were around 2 mm thick and skin slices were around 1 mm thick. Imaging was repeated when tissue was placed on top of the wells.

A black well, clear bottom 96-well plate was prepared with 240 μM naphthofluorescein, 50 μL ^{68}Ga and citrate/borate/phosphate buffer (0.05 M) at pH 4, 7.4 or 8, added to achieve a final volume of 250 μL. Conditions were plated in triplicate. This plate was imaged in the IVIS Spectrum. 1 mm chicken slices were placed on top of wells containing activity in an additive manner, until reaching 4 mm thickness. Chicken slices were obtained from frozen chicken breast (ACME), sliced using a meat slicer set to 1 mm thickness. Imaging was repeated with each addition of a chicken slice, for a total of 5 imaging cycles.

To determine tissue effects *in vivo* mice bearing 4175-Luc+ tumors were injected intratumorally with 20 μL NFbD-^{68}Ga (~27 μCi). These mice were imaged in the IVIS Spectrum and euthanized. After euthanasia, the skin over the tumors was removed, and imaging was repeated. Tumors were then excised and imaged, and finally, tumors were sliced and imaged.

2.13 **In vivo** ***pH modulation***

Mice bearing 4175-Luc+ tumors were injected with 20 μL NFbD-^{68}Ga (~35 μCi) intratumorally and in the right thigh to evaluate pH response of NFbD in the acidic tumor milieu, using the muscle as an internal control. Injected mice were imaged in the IVIS Spectrum.

Mice bearing 4175-Luc+ tumors were injected intratumorally with 100 μL solution of naphthofluorescein (110 μM) and ~22 μCi of ^{68}Ga (pH adjusted with NaOH 0.1 N). Mice were imaged in the IVIS Spectrum. After imaging, mice were injected intratumorally with $NaHCO_3$ (200 mM) to increase tumor pH. Imaging was repeated.

2.14 Statistical Analysis

Data was processed using Microsoft Excel and GraphPad PRISM. Data are presented as mean ± standard deviation of triplicate values (n = 3), unless otherwise noted. Non-linear regressions to obtain pH values were performed with GraphPad PRISM. Statistical significance is defined as p-values lower than 0.05.

Chapter 3

Naphthofluorescein-butyl-DOTA (NFbD)

3.1 Introduction

This chapter describes the synthesis of a pH-sensitive, Cerenkov-active imaging molecule, capable of attenuating Cerenkov signal and producing subsequent CRET. This probe, NFbD, is a naphthofluorescein derivative, which is pH-dependent and exhibits a robust color change from fuchsia in the acidic or protonated form ($pH < pK_a$) to bright blue in the basic or deprotonated form ($pH > pK_a$). This change in color can be exploited to modulate Cerenkov radiation to enable relevant pre-clinical molecular imaging studies.

Cerenkov emitters such as ^{68}Ga and ^{90}Y emit Cerenkov radiation in a broad and continuous frequency spectrum, with an intensity proportional to $1/\lambda^2$, which includes visible light. These emitters, when coupled to a fluorophore like NFbD, act as an "internal lightbulb" providing them with the energy necessary to absorb and fluoresce. This kind of absorption and fluorescence selectively affect the continuous emission of the Cerenkov spectrum. Selective Bandwidth Quenching, or SBQ is observed as a decrease or attenuation of the signal in the Cerenkov spectrum at the wavelength at which the fluorophore absorbs. Cerenkov Radiation Energy Transfer or CRET is observed as an increase of the signal in the Cerenkov spectrum at the wavelength at which the fluorophore fluoresces (Figure 3.1). These changes in signal can be detected with a sensitive camera such as the CCD camera present in the PerkinElmer IVIS Spectrum.

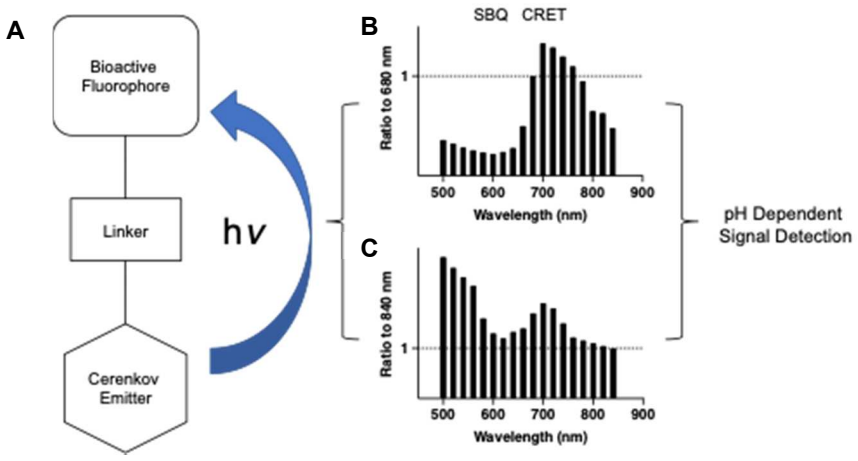

Figure 3.1 ***Scheme for the detection of pH dependent Cerenkov signals.*** *A.* A Cerenkov emitter supplies the required energy to excite a linked fluorophore, acting as an "internal lightbulb". This absorption leads to Selective Bandwidth Quenching (SBQ) near the absorption maxima of the fluorophore of choice. Cerenkov Radiation Energy Transfer (CRET) or Cerenkov-induced fluorescence is observed near the emission maxima of the fluorophore. *B.* Example Cerenkov spectra normalized to the 680 nm filter (isosbestic point of NFbD), exhibiting SBQ and CRET. *C.* Example Cerenkov spectra normalized to the 840 nm filter (increased tissue penetration). pH dependent signals can be obtained from SBQ and CRET measurements, when linking the Cerenkov emitter to a pH sensitive fluorophore.

NFbD was designed as a second-generation Cerenkov active probe, which incorporates a brighter Cerenkov emitter than the ones previously used in our lab, ^{18}F (Arroyo et al., 2019; Czupryna et al., 2015; Kachur et al., 2017; Kachur et al., 2013a; Kachur et al., 2013b). The molecular structure of NFbD includes a fluorophore, a linker, and a chelator, all of which could be fine-tuned or replaced to obtain optimal properties for the desired application. For this project, naphthofluorescein was our fluorophore of choice because of its optical properties, price, and availability. DOTA was chosen as our chelator because it can create coordination complexes with ^{68}Ga and ^{90}Y (Baranyai et al., 2020). These Cerenkov emitters produce a brighter Cerenkov signal than ^{18}F, due to their higher endpoint energies, aiding in signal detection (Ciarrocchi and Belcari, 2017).

3.2 Naphthofluorescein-butyl-DOTA (NFbD) Conjugation

Naphthofluorescein-butyl-DOTA (NFbD) results from the conjugation between the fluorophore, 5(6)-Carboxynaphthofluorescein succinimidyl ester (CNF-SE) and the chelator, 4-aminobutyl-DOTA (DOTA), which occurred through a nucleophilic substitution. For this synthesis, 4.5 mg CNF-SE were dissolved in 10 µL triethylamine (TEA) and 500 µL dichloromethane (DCM). 4.3 mg 4-aminobutyl-DOTA were dissolved in 30 µL H_2O and 480 µL methanol. The 4-aminobutyl-DOTA solution was added dropwise to the CNF-SE solution, and left stirring for one hour at 25º C (room temperature). The reagents in this reaction were added in a 1:1 molar ratio. This reaction occurs optimally in the absence of water which is the reason mostly organic solvents were used. 4-Aminobutyl-DOTA required water for dissolution, which was kept at a minimum.

The product was dried under N_2 to remove volatile organic solvents from solution, and then lyophilized overnight. The dried product was resuspended in a 50:50 mixture of acetonitrile/water and injected into a Waters Alliance e2695 HPLC with a reverse-phase column (Phenomenex Synergy 4µ Hydro-RP 80 Å 10 x 250 mm), which ran for 40 minutes in a 95%-5% solution of water-acetonitrile with 0.1% trifluoroacetic acid with collection from minute 30 to 36. This product was again dried under N_2 to remove acetonitrile and lyophilized, yielding a dark pink film. The product was weighed and dissolved in the appropriate volume of ethanol to obtain a 1 mg/mL solution. This

solution was divided into 1 mL aliquots and the ethanol was dried under N_2, obtaining aliquots of 1 mg NFbD per vial.

3.3 NFbD Chelation with Gallium

Chelation of NFbD was first done with ^{69,71} Gallium, which is non-radioactive, to prevent equipment contamination during characterization. 46 µL $GaCl_3$ (1.14 M in 6 N HCl) was added to NFbD (resuspended in 0.5 M ammonium acetate) in a 2:1 molar ratio, to a total of 2 mL. This solution was stirred for 5 minutes, then heated for 5 minutes at 85- 90º C, and stirred for 10 minutes. 100 µL 1 N HCl was added to this solution to obtain the product, which precipitated after 1 minute of centrifugation. Supernatant was removed and the remaining pellet was dissolved in 1% ethanol/saline solution. This solution was neutralized to pH 7 with NaOH before experimental applications.

The purpose of conjugating CNF-SE with DOTA was to create a pH sensitive fluorophore that could incorporate a Cerenkov emitter in its structure. For this project, our Cerenkov emitter of choice was ^{68} Gallium. To obtain this molecule, 1 mg NFbD was resuspended in 500 µL 0.5 M ammonium acetate and 10 µL 0.5 N NaOH (to aid in dissolution). 500 µL ^{68} Gallium was eluted in 4 mL 0.05 M HCl (~215 µCi), added to the NFbD solution, stirred, and heated at 85- 90º C for 5 minutes. This solution was divided into two 1.5 mL Eppendorfs tubes. 25 µL of 1 N HCl was added to each tube followed by centrifugation at 6000 rpm for 1-2 minutes. NFbD is insoluble in acidic conditions, so the addition of acid and further centrifugation resulted in the precipitation of the product,

NFbD-^{68} Ga. The supernatant was removed and the product dissolved in the desired volume of a 1% ethanol/saline solution for either *in vitro* or *in vivo* experiments.

3.4 Results

NFbD was obtained through a condensation reaction where the succinimidyl ester in the CNF-SE was replaced by the amino group of the 4-aminobutyl-DOTA (Figure 3.2). This reaction was completed in one hour and was confirmed by MALDI-TOF, where the parent ion peak was seen at 934 m/z$^+$ (Figure 3.3). A peak is seen at 477 m/z$^+$, which corresponds to unreacted carboxynaphthofluorescein. The 379 m/z$^+$ peak corresponds to the matrix, CHCA. NFbD showed a maximum absorbance at λ_{exc} = 600 nm and a maximum emission at λ_{em} = 669 nm at basic pH (Figure 3.4A). NFbD also maintained its pH sensitivity after conjugation, showing a pK_a of 7.8 (Figure 3.4B,C). The optical properties of NFbD are comparable to its parent compound

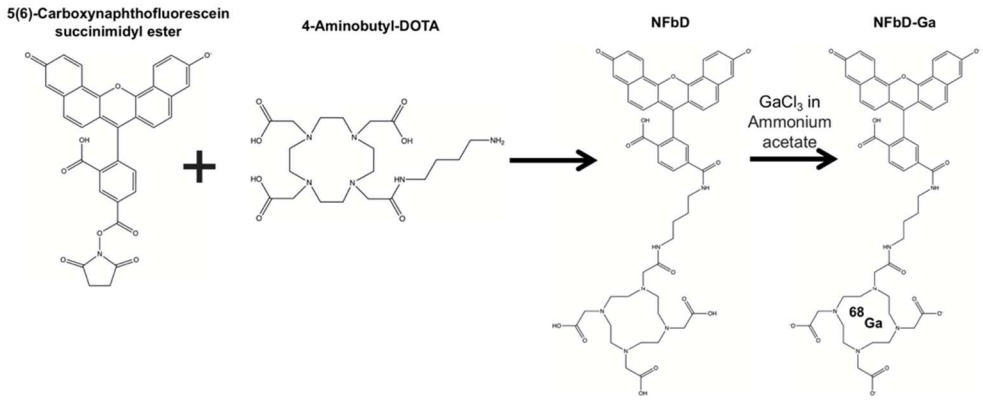

Figure 3.2 ***Synthetic scheme for NFbD and NFbD-Ga.*** 4-Aminobutyl-DOTA dissolved in methanol/water was added dropwise to 5(6)-carboxynaphthofluorescein succinimidyl ester dissolved in dichloromethane/TEA (1:1 molar ratio) and stirred for 1 hour to produce NFbD. NFbD was purified by HPLC, lyophilized, and dissolved in ammonium acetate 0.5 M. For chelation, $GaCl_3$ was added in excess, stirred, heated (85 ºC-90 ºC, 5 minutes), stirred for 10 minutes) and precipitated with HCl.

naphthofluorescein, which has an absorption maximum at λ_{exc} = 595 nm, maximum emission at λ_{em} = 660 nm and reported pK_a of 7.6-7.8 (2022d; Chiorazzo, 2016; Lavis, 2022; Lavis and Raines, 2008).

To determine photostability, fluorescence of NFbD was measured every 5 seconds for 18 hours at λ_{exc} = 600 nm/λ_{em} = 669 nm (Figure 3.4D). NFbD exhibited a higher photostability than naphthofluorescein alone, which was used as a control. At a concentration of 10.1 μM, NFbD had a photobleaching half-life ($t_{1/2}$) of 967 minutes, while naphthofluorescein at a concentration of 10.4 μM had a $t_{1/2}$ of 531 minutes. Even at higher concentrations, naphthofluorescein showed a decreased photobleaching half-life (17.8 μM, $t_{1/2}$= 851 minutes), as shown in Figure 3.4.

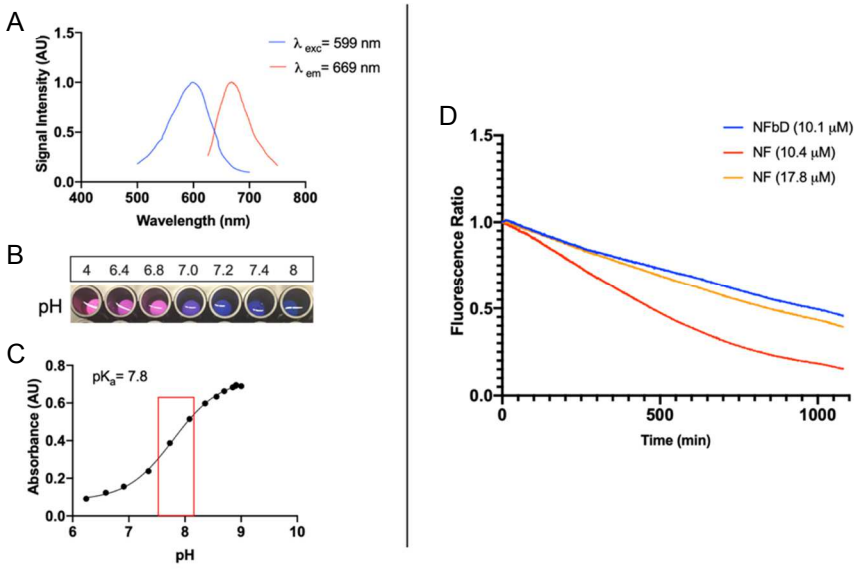

Figure 3.4 ***Spectroscopic properties of NFbD***. *A.* Absorbance and fluorescence spectra of NFbD at pH 9, λ_{exc} = 599 nm, λ_{em} = 669 nm. *B.* Visual representation of pH-dependent color change of NFbD, from its protonated (fuchsia) to unprotonated (blue) form. *C.* pH titration of NFbD confirms pH sensitivity at physiologically relevant pH values, pK_a = 7.8. *D.* Photostability assay of NFbD at pH 9. Fluorescence was measured every 5 seconds for 18 hours at λ_{exc} = 600 nm, λ_{em} = 669 nm. NFbD shows higher photostability compared with naphthofluorescein alone. NFbD (10.1 μM), $t_{1/2}$ = 966.6 minutes, NF (10.4 μM), $t_{1/2}$ = 531.4 minutes, NF (17.8 μM), $t_{1/2}$ = 851.1 minutes.

NFbD was chelated with gallium, through a hexacoordinated complexation with DOTA (Kubíček et al., 2010). This reaction was completed in less than 30 minutes and was confirmed by MALDI-TOF with peaks at 1000 m/z^+, 1002 m/z^+ (NFbD+ $^{69, 71}$Ga). MALDI-TOF also showed a significant peak at 547 m/z^+ corresponding to a hydrolyzation of NFbD with DOTA as a leaving group (Figure 3.5). NFbD-Ga maintained optical properties, with a maximum absorbance at λ_{exc} = 600 nm, a maximum emission at λ_{em} = 669 nm at basic pH. NFbD-Ga maintained pH sensitivity exhibiting a pK_a = 7.7 (Figure 3.6).

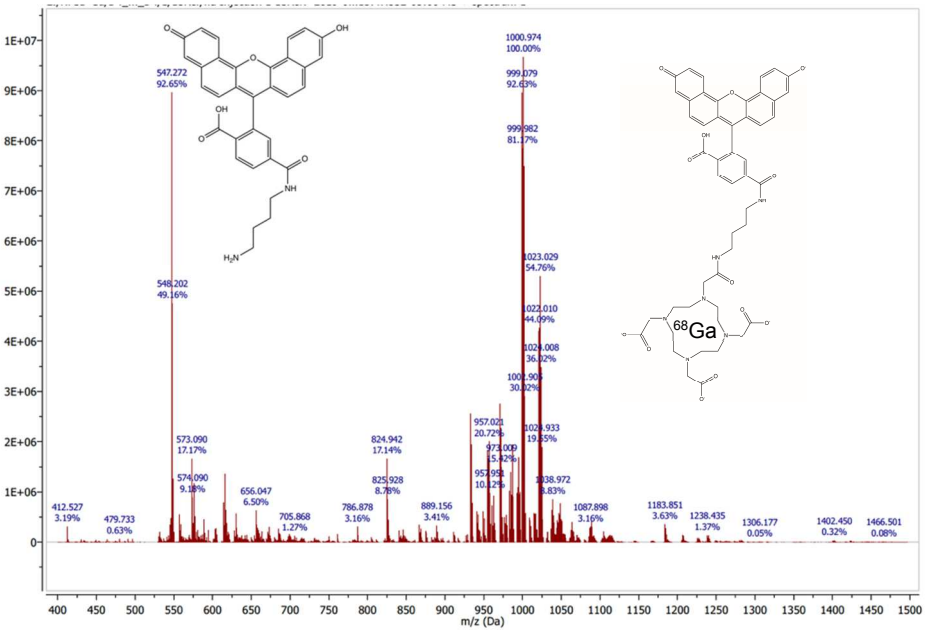

Figure 3.5 ***MALDI-TOF of NFbD-Ga***. NFbD-Ga peaks are seen at 1000.974 m/z$^+$ (100%), 999.079 (92.63%) and 1002.905 (30.02%). Peak at 547.272 m/z$^+$ (92.65%) corresponds to hydrolyzed NFbD, with DOTA as a leaving group.

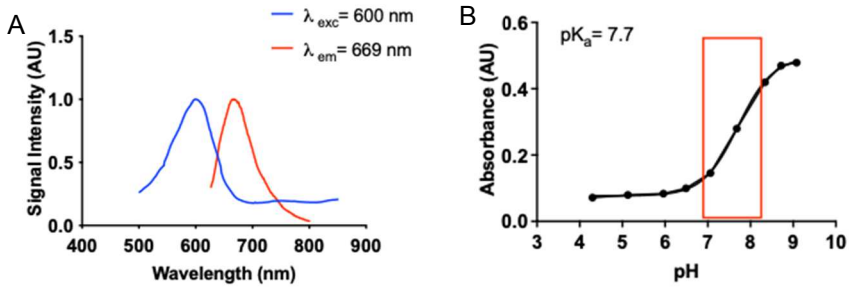

Figure 3.6 ***Spectroscopic properties of NFbD-Ga***. *A.* Absorbance and fluorescence spectra of NFbD at pH 9, λ_{exc} = 600 nm, λ_{em} = 669 nm. *B.* pH titration of NFbD-Ga confirms pH sensitivity at physiologically relevant pH values, pKa = 7.7.

3.5 Discussion

The purpose of this study was to develop a modifiable molecular scaffold which included a bioactive fluorophore, a linker, and a chelator to obtain a Cerenkov-active probe. A Cerenkov-active probe is defined as a molecule whose structure contains a fluorescent moiety that is capable of absorbing and/or fluorescing due to the energy provided by a Cerenkov emitter. Such a molecular construct would allow Cerenkov imaging to be used for tracking desired metabolic responses *in vitro* and *in vivo*, such as redox status and pH, without the need of an external energy source.

We were able to conjugate the fluorophore CNF-SE to the chelator 4-aminobutyl-DOTA, to obtain the pH-dependent, Cerenkov-active probe NFbD. This conjugation was achieved through a condensation reaction in a one-step reaction with commercially available reagents. While elucidating the optimal synthesis conditions for NFbD, we were able to identify MALDI peaks that corresponded to hydrolysis, which led to the determination of using only organic solvents in this reaction (data not shown). However, 4-aminobutyl-DOTA needed a small percentage of water to dissolve properly so the reaction could take place. The MALDI corresponding to NFbD-Ga showed a fractionation peak at 547 m/z^+, corresponding to hydrolysis of NFbD, with DOTA as a leaving group. This kind of spectroscopic analysis was greatly helpful in understanding our reaction conditions, ultimately allowing us to troubleshoot and optimize to increase efficiency.

As desired, NFbD maintained the optical properties of its parent fluorophore, naphthofluorescein, with absorption at λ_{exc} = 600 nm and emission at λ_{em} = 669 nm. Absorption and emission wavelengths for NFbD are closer to the far red, which makes it suitable for *in vivo* imaging. Additionally, NFbD maintained its pH sensitivity, crucial for the success and progression of this project. For the capability of obtaining *in vivo* pH measurements, the pK_a of the fluorophores used should be close to physiological pH, 7.2. Spectroscopic studies of NFbD showed a pK_a of 7.8, which is slightly higher than optimal. However, it has been shown that pK_a measured through Cerenkov imaging exhibits lower values (Arroyo, 2019; Arroyo et al., 2021; Arroyo et al., 2019; Czupryna et al., 2015), as will be demonstrated in upcoming chapters. Finally, NFbD showed increased photostability compared to naphthofluorescein, for reasons which are not currently understood.

We were able to chelate NFbD with Ga in 30 minutes. This reaction needed to be completed as quickly as possible since ^{68}Ga has a half-life of 68 minutes. The detectable signal obtained from Cerenkov imaging greatly depends on the amount of activity present, which in turn depends on the time it takes for the isotope to go from the generator to the IVIS Spectrum. Photoexcited molecules go through various relaxation pathways, the most common of which is a vibrational transition which does not produce fluorescence. If activity is low, the Cerenkov emitter will not be able to excite enough molecules to warrant detectable fluorescence, and pH dependent signals will not be measureable through CRET. We are interested in measuring CRET because it is a red-shifted signal, ideal for *in vivo* imaging.

Chelation with $^{69, 71}$Ga did not affect the pH sensitivity of NFbD nor its optical properties, yielding a successful product, with λ_{exc} = 600 nm, λ_{em} = 669 nm and a pK_a = 7.7. NFbD-Ga was characterized only in its non-radioactive form to prevent radioactivity contamination to any equipment, and it was assumed that its optical properties would be identical to those of its radioactive counterpart.

3.6 Conclusion

This chapter presented the one step synthesis of NFbD, followed by its "shake and shoot" chelation with gallium. This Cerenkov-active probe was synthesized with the purpose of expanding the applications of Cerenkov imaging in a pre-clinical setting. NFbD is a molecule that absorbs and fluoresces in a pH-dependent manner by excitation through an external energy source (laser) or by interacting with Cerenkov emitters, such as gallium. This allows us to use Cerenkov imaging for pH determination, which can be applied to studies of the tumor microenvironment *in vitro* and *in vivo.* In addition, NFbD presents a molecular construct that can be fine-tuned to fit the needs of the desired application, by substituting the bioactive fluorophore and/or the chelator, to obtain Cerenkov signals pertaining to a different molecular target.

Chapter 4

NFbD *in vitro*

4.1 Introduction

Cerenkov radiation occurs when a β-particle travels faster than the speed of light in a dielectric medium, transferring its kinetic energy to adjacent particles which undergo relaxation through light emission (Das et al., 2014). This light emission is continuous and multispectral with an intensity proportional to $1/\lambda^2$, which includes the visible spectrum. When a Cerenkov emitter is coupled with a fluorophore, it will act as an "internal lightbulb", providing the energy necessary for the fluorophore to absorb and fluoresce. This absorption and subsequent fluorescence cause a disruption to the continuous Cerenkov spectrum, resulting in measurable signals that can correspond to certain biological parameters such as pH, depending on the fluorophore of choice (Arroyo et al., 2019).

Attenuation resulting from absorption of Cerenkov radiation is called Selective Bandwidth Quenching (SBQ) and it occurs near the wavelength at which a chromophore absorbs (Czupryna et al., 2015). Fluorescent molecules will also show a Cerenkov-induced fluorescence or Cerenkov Radiation Energy Transfer (CRET), an emission following SBQ, near the wavelength at which the fluorophore emission occurs. CRET is a valuable phenomenon for *in vivo* imaging because it results in a red shift of Cerenkov photons, reducing the effects of tissue scattering and absorption in optical imaging (Bernhard et al., 2017). For this project, NFbD, a naphthofluorescein derivative, was

coupled with the Cerenkov emitter ^{68}Ga with the purpose of detecting tumor microenvironment (TME) pH *in vivo*. This probe was first tested *in vitro*, to confirm pH-dependence and to establish cellular models of acidification.

In this Chapter, we test the ability of NFbD-Ga to act as a pH sensor *in vitro* and in cell models. Our cell models consisted of the MDA-MB-231 and 4175-Luc+ cells, triple negative breast cancer cell lines with varying expression of lactate dehydrogenase A (LDHA), the enzyme responsible for catalyzing the conversion of pyruvate into lactate (Luo et al., 2021). 4175-Luc+ cells express increased levels of LDHA, compared to MDA-MB-231 cells, leading to the hypothesis that 4175-Luc+ would exhibit higher acidification *in vivo*, due to increased co-secretion of lactate with a proton (Arroyo, 2019). Lactate dehydrogenase inhibitors (LDHi) were used as an alternative method for pH modulation. TME acidification occurs after co-secretion of lactate with a proton (Manzo-Merino et al., 2019). If the enzyme converting pyruvate to lactate is inhibited, lactate production and secretion should decrease, decreasing acidification (Rai et al., 2017). Establishing acidification or alkalization models would allow appropriate controls to be considered when measuring pH through Cerenkov imaging.

4.2 Results

In vitro Cerenkov imaging was achieved with NFbD-Ga at physiologically relevant pH values. A 96-well plate containing a phosphate, borate, citrate buffer (0.05 M) (Kachur et al., 2017) at pH 4, 6.4, 6.8, 7.0, 7.4 and 8 was prepared in triplicate (pH adjusted with HCl or NaOH). ~100 μCi ^{68}Ga were added to each well to detect pH

dependent differences in Cerenkov radiation (Figure 4.1). pH-Dependent SBQ was observed between the 580 nm filter and the 660 nm filter, with maximum SBQ observed at 600 nm, close to the $\lambda_{max\ abs}$ for NFbD (600 nm). In Figure 4.1A, SBQ is visually identifiable as the dark wells, as pH increases. At longer wavelengths ($\lambda \geq 680$ nm), CRET can be observed as brighter wells with increasing pH, Figure 4.1.A. Maximum CRET occurs at 700 nm, which is red shifted from the $\lambda_{max\ em}$ for NFbD (669 nm). Images obtained through Cerenkov imaging were quantified using the LivingImage software from PerkinElmer, allowing pH-dependent Cerenkov spectra to be plotted, as shown in Figure 4.1.B-C. These spectra illustrate the pH-dependent signal attenuation and subsequent CRET that is produced when NFbD is in the presence of a Cerenkov emitter, ^{68}Ga. These data were normalized in two ways. First, ratios for the average radiance at each point were calculated relative to the 840 nm filter, which is the wavelength at most light penetration is expected in tissue (Figure 4.1.B). Additionally, the ratio of average radiance for each point was calculated relative to the wavelength at which maximum SBQ occurs, 600 nm, which greatly amplified the CRET signal, aiding in signal visualization (Figure 4.1.C).

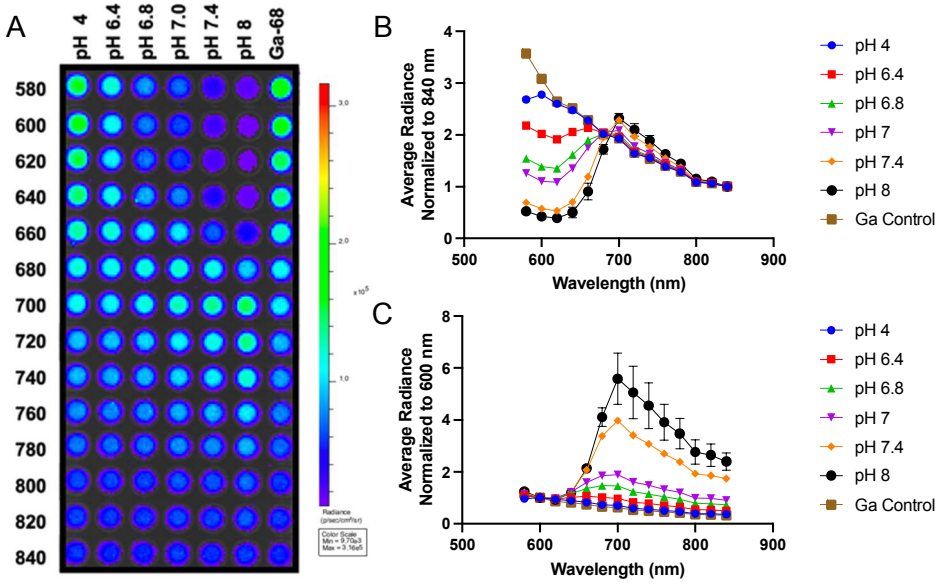

Figure 4.1 ***pH dependent intermolecular Cerenkov imaging of NFbD.*** *A*. Cerenkov image of NFbD mixed with ~100 µCi ^{68}Ga at various pH values. The maximum SBQ is observed at 600 nm due to absorption of Cerenkov radiation by NFbD in basic form. The maximum CRET is observed between 700 nm and 720 nm. *B*. Cerenkov spectrum at various pH values of NFbD mixed with ^{68}Ga, normalized to 840 nm filter. *C*. Cerenkov spectrum at various pH values of NFbD mixed with ^{68}Ga, normalized to 600 nm filter.

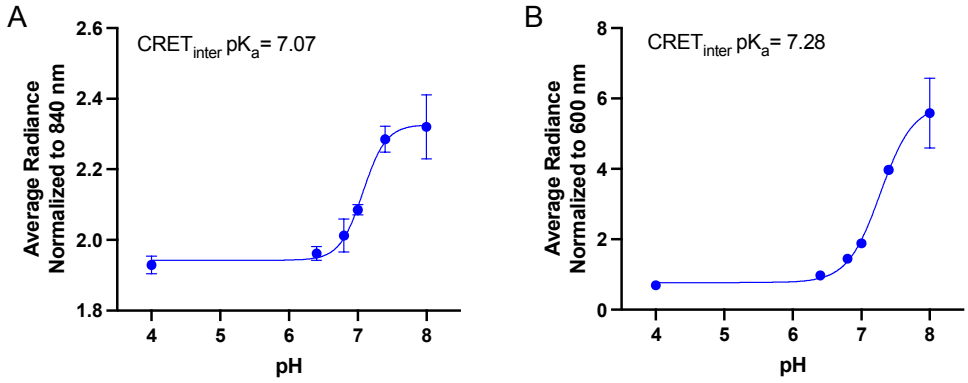

Figure 4.2 ***Intermolecular Cerenkov pH titration curve for NFbD with ^{68}Ga.*** *A*. pH titration curve at maximum CRET (700 nm), normalized to 840 nm filter. CRET$_{inter}$ pK$_{a\ (840nm)}$ = 7.07. *B*. pH titration curve at maximum CRET (700 nm), normalized to 600 nm filter. CRET$_{inter}$ pK$_{a\ (600\ nm)}$ = 7.28.

Cerenkov spectra were then plotted as the average radiance ratio as a function of pH, to allow for interpolation of *in vivo* pH values, as seen in Figure 4.2. These graphs were plotted using the Cerenkov signals obtained with the 700 nm filter, providing CRET pK_a values ($CRET_{inter}pK_{a\ (840\ nm)} = 7.07$, $CRET_{inter}pK_{a\ (600\ nm)} = 7.28$). As mentioned in the previous chapter, these pK_a values were lower compared to the pK_a vales obtained through spectroscopy.

The Cerenkov spectra and pH titration curves in Figures 4.1 and 4.2 showed intermolecular Cerenkov signals (NFbD mixed with ^{68}Ga). Figure 4.3 shows spectra and titration curves constructed using intramolecular Cerenkov signals, where ^{68}Ga was chelated into NFbD, producing NFbD-Ga. SBQ and CRET patterns were identical to those observed intermolecularly, with a decreased CRET intensity (Figure 4.3.A-B). This could be due to ^{68}Ga and NFbD molecules having less interactions resulting in fluorescence when chelated than when mixed. CRET pK_a values were obtained for intramolecular Cerenkov, as in the previous figure (Figure 4.3.C-D) ($CRET_{intra}pK_{a\ (840\ nm)} = 7.58$, $CRET_{intra}pK_{a\ (600\ nm)} = 7.50$). Although this phenomenon needs to be explored further, studies have shown that CRET is dependent on fluorophore concentration and the activity of the Cerenkov emitter, seen in Figure 4.4. CRET efficiency, defined as the ratio of the signal obtained at 700 nm to the signal obtained at 600 nm (CRET/SBQ), is proportional to fluorophore concentration and to Cerenkov emitter activity.

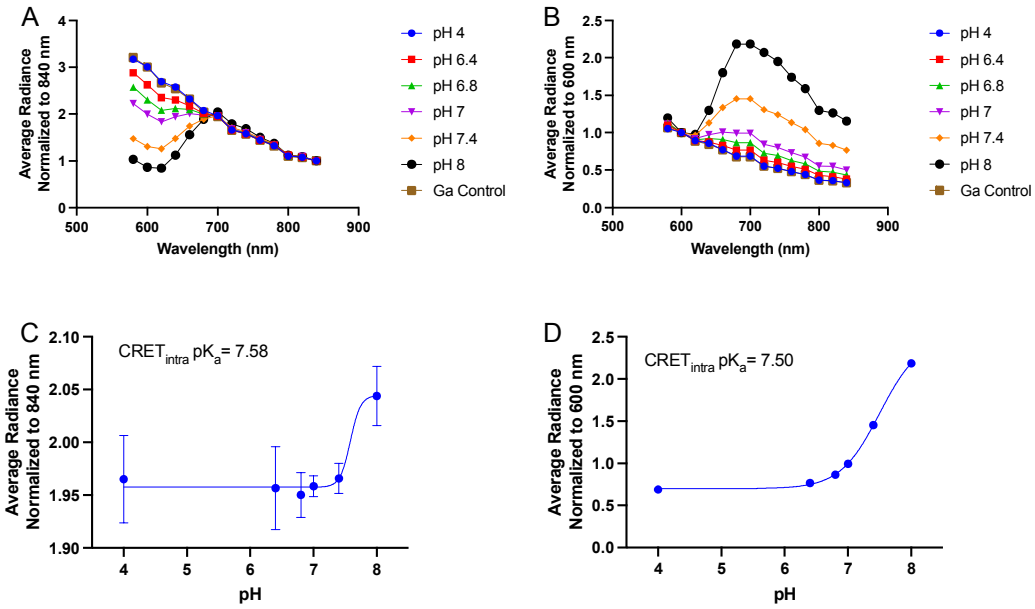

Figure 4.3 ***Intramolecular Cerenkov imaging of NFbD with ^{68}Ga.*** *A.* Intramolecular Cerenkov (chelated NFbD-^{68}Ga) spectrum of ~ 80 µCi NFbD-Ga at different pH values, normalized to 840 nm filter. *B.* Cerenkov spectrum normalized to 600 nm filter. SBQ and CRET are observed at 600 nm and 700 nm, respectively. *C.* Cerenkov pH titration curve of *A*. CRET$_{inter}$ pK$_{a\ (840nm)}$ = 7.58. *E.* Cerenkov pH titration curve of *B*. CRET$_{inter}$ pK$_{a\ (600nm)}$ = 7.50.

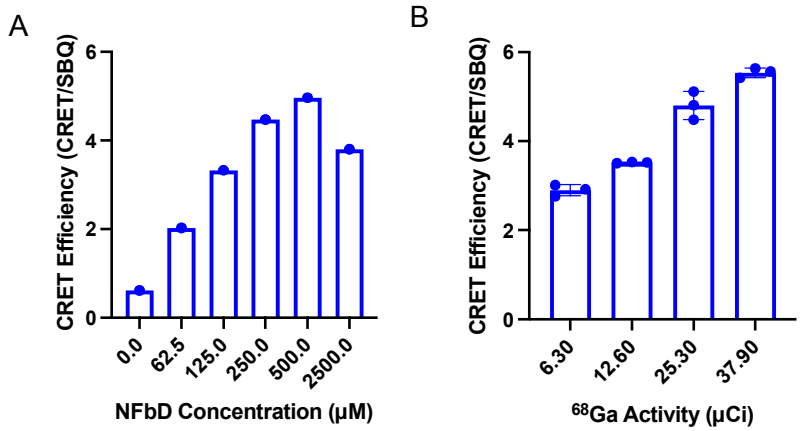

Figure 4.4 ***CRET is proportional to fluorophore concentration and Cerenkov emitter activity.*** *A*. CRET efficiency plotted as a function of NFbD concentration shows a maximum at 500 µM. *B*. CRET efficiency plotted as a function of ^{68}Ga activity, with 240 µM naphthofluorescein.

NFbD was characterized *in vitro* using two triple negative breast cancer cell lines: MDA-MB-231 and its metastatic variant, 4175-Luc+. As mentioned previously, these are aggressive cancer cell lines with varying expression of LDHA, which catalyzes the conversion of pyruvate to lactate and whose co-secretion with a proton decreases extracellular pH in tumors. 4175-Luc+ cells express higher LDHA levels compared to MDA-MB-231 cells (Arroyo, 2019). This difference in LDHA expression led to the hypothesis that 4175-Luc+ would have a higher acidification rate than MDA-MB-231, providing potential *in vitro* and *in vivo* models of acidification.

First, the toxicity of NFbD was determined. MDA-MB-231 and 4175-Luc+ cells were treated with increasing concentrations of non-radioactive NFbD-Ga and cell viablility was determined with the MTT assay. The results showed no changes in cell viability at concentrations up to 5 µM, as seen in Figure 4.5, suggesting that NFbD-Ga is not toxic to these cell lines.

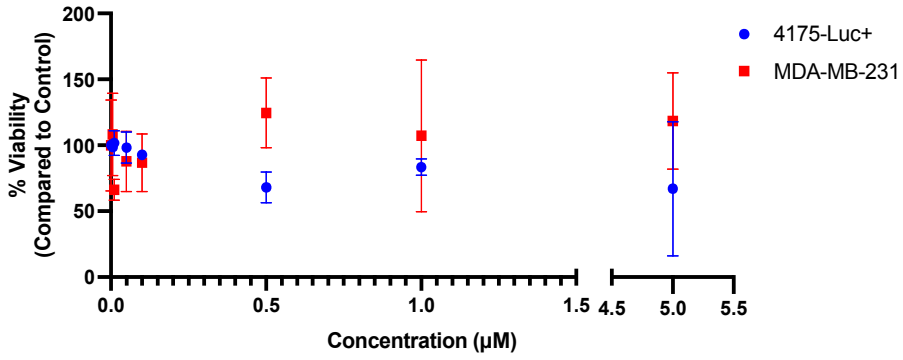

Figure 4.5 ***NFbD-Ga cell toxicity*** **in vitro.** MDA-MB-231 and 4175-Luc+ (7.5×10^4 cells/well) were treated with non-radioactive NFbD-Ga (5 nM -5 µM). Cell viability was measured using the MTT assay, which showed no cell toxicity.

After evaluating toxicity, cellular uptake of NFbD was assessed. Fluorescence microscopy was performed on 4175-Luc+ cells treated with NFbD (3 μM), which showed no intracellular uptake after a 45-minute incubation, Figure 4.6.A. Hoechst, a nuclear stain, was used as a positive control. These results were further confirmed by incubating 4175-Luc+ (1.0×10^4 cells/well) cells with varying concentrations of NFbD for 30 minutes, followed by rinsing with PBS and then treating them with Triton X-100 (0.5%) for 5 or 10 minutes, Figure 4.6.B. No changes in absorbance were observed after Triton treatment, suggesting no intracellular uptake.

Cell acidification was assessed after a 24-hour incubation in Seahorse XF unbuffered media (Agilent) containing glucose (25 mM), FBS (10%) and P/S (1%). Media was collected after incubation and pH was measured. 4175-Luc+ cells showed increased acidification compared to MDA-MB-231 (ratio to media control containing no cells), seen in Figure 4.7.A. Glucose consumption and lactate production were also evaluated in both cell lines, showing no significant differences, Figure 4.7.B & C.

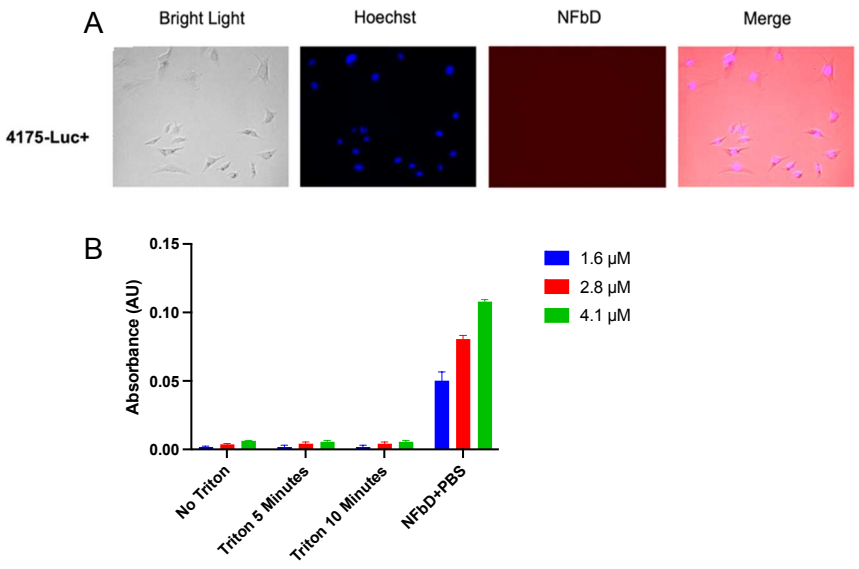

Figure 4.6 ***Intracellular uptake of NFbD*** **in vitro.** *A*. Fluorescence microscopy performed with 4175-Luc+ cells (1.0 x 10^4 cells/well) treated with NFbD showed no intracellular uptake (45 minute-incubation, 3 µM). *B*. Absorbance of 4175-Luc+ cells (1.0 x 10^4 cells/well) before and after triton treatment showed no difference in absorbance, suggesting no uptake.

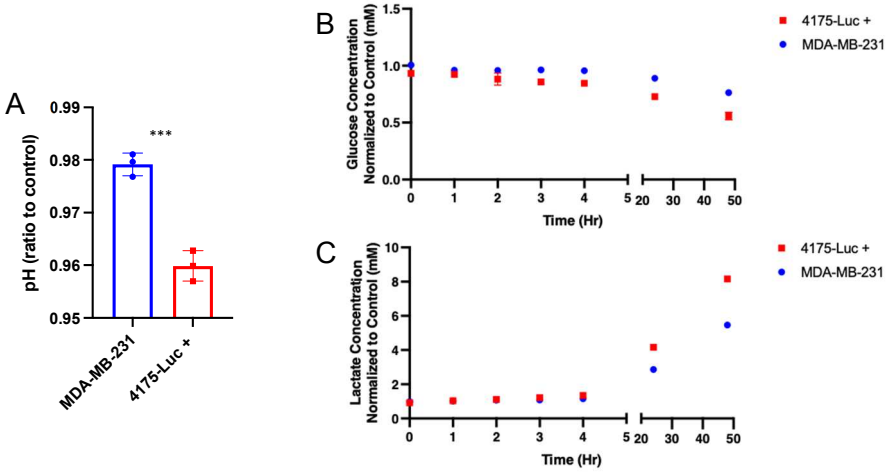

Figure 4.7 ***Evaluation of cell acidification, glucose consumption and lactate production.*** *A*. pH determination of MDA-MB-231 and 4175-Luc+ cell lines (1.0 x 10^6 cells/well) plotted as the ratio to control (media) shows decreased pH for 4175-Luc+ cells after a 24-hour incubation (P-value < 0.05, unpaired t-test). *B* & *C*. Glucose consumption and lactate production of MDA-MB-231 and 4175-Luc+ cell lines show no significant difference (P-value > 0.05, unpaired t-test).

Since glucose consumption and lactate production did not yield significant differences between cell lines, the use of LDH inhibitors was explored to obtain a more robust alkalization model. Two LDHis were studied, shown in Figure 4.8.A. 4175-Luc+ cells (1.0 x 10^4 cells/well) were treated with varying concentrations of each inhibitor, showing no changes in cell viability, Figure 4.8.B. 4175-Luc+ cells (3.0 x 10^5 cells/well) were treated with 50 µM of each LDHi and media was collected at different time points to analyze glucose consumption and lactate production, which did not yield significant differences Figure 4.8.C-F.

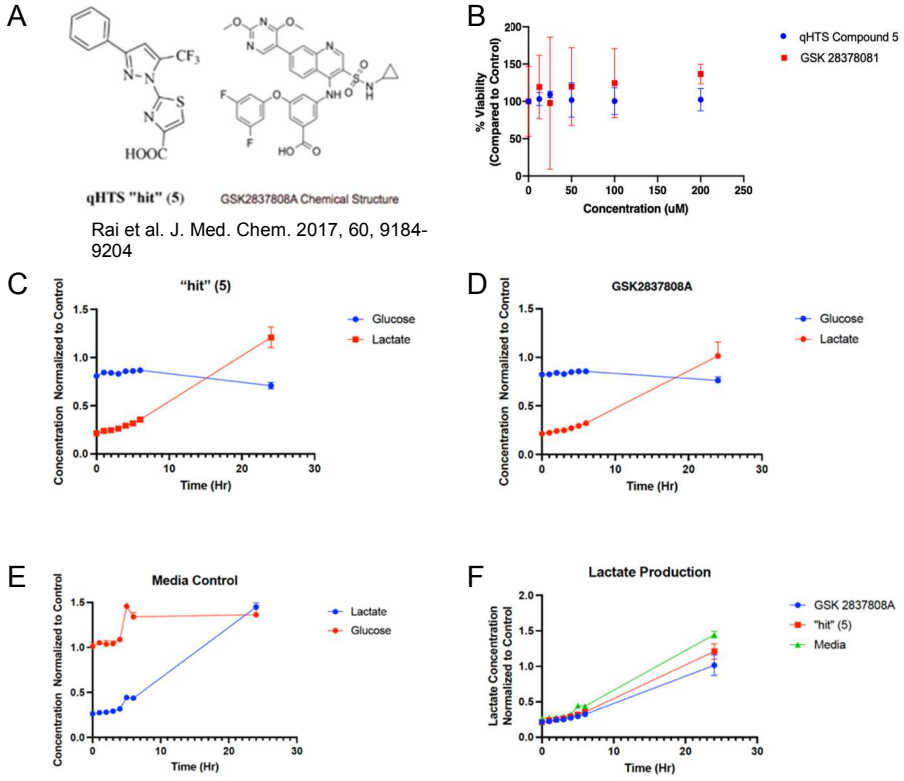

Figure 4.8 In vitro e*valuation of LDHi in 4175-Luc+ cells.* *A*. Molecular structures of LDHi: Compound 5 and GSK 2837808A. *B*. Cell viability plotted as a function of concentration evaluated for each LDHi using Cell Titer Glo assay. *C-E.* Glucose consumption and lactate production plotted as a function of time for each LDHi and media control. *F.* Comparison of lactate production for each LDHi and the media control showed no significant differences (P-value >0.05, unpaired t-test).

4.4 Discussion

This chapter describes the *in vitro* characterization of NFbD. Cerenkov imaging showed the ability to detect pH changes intermolecularly and intramolecularly through SBQ and CRET of NFbD. This detection was visualized as increasingly dark wells with increasing pH, corresponding to absorption or SBQ at 600 nm (max SBQ). At 700 nm, the previously dark wells become bright, corresponding to pH-dependent CRET. Cerenkov signals obtained at different wavelengths can be used to construct a Cerenkov spectrum for NFbD, as seen in Figure 4.1. The Cerenkov spectra presented are normalized either to signals obtained at 840 nm or at 600 nm. Since the goal of this project is to use NFbD for *in vivo* imaging of the TME, normalizing to 840 nm is of interest, due to the increased tissue penetration of light at this wavelength. Normalizing to the maximum SBQ value at 600 nm greatly amplifies the pH-dependent CRET signal, aiding in visualization.

Intramolecular Cerenkov emissions exhibit identical pH-dependent SBQ and CRET patterns but with decreased CRET. Although the reason for this needs further exploration, we propose a potential mechanism. It is possible that NFbD and ^{68}Ga have more fluorescence-inducing interactions when they are mixed than when they are part of the same molecule (chelated). Excited molecules undergo vibrational relaxation with a higher probability than fluorescence (Jaffe and Miller, 1966). If NFbD and ^{68}Ga are available to interact more freely without a determined molecular arrangement (such as with chelation), ^{68}Ga might be able to excite more NFbD molecules, increasing the probability of fluorescence. Another possibility could relate to the specific activity of

^{68}Ga (4.1 x 10^7 Ci/g) (Applications, 2022). Stoichiometric calculations for a 1:1 ratio of ^{68}Ga to NFbD for 100 µCi of ^{68}Ga, yields 0.036 pmoles of NFbD, equating to 3.6 x 10^{-4} µM in 100 µl in a 96-well plate. This is an extremely low amount of fluorophore, and it is unlikely that it will be detected by optical imaging methods. As seen in Figure 4.4, CRET is proportional to fluorophore concentration up to the concentration where quenching occurs. Because of this, it is necessary to have an excess of fluorophore, which could decrease through the chelation process, reducing CRET.

pH titration curves were constructed with inter- and intramolecular Cerenkov imaging signals, with normalization to the 840 nm and 600 nm filters. An important observation about these titration curves is that normalizations to signals from different filters yield different results, leading to variation in the calculated pK_a results. Additionally, experimental conditions such as slight differences in available ^{68}Ga activity could affect final signal, as could the phenomena described in the previous paragraph. These are limitations, which we believe could be further optimized to obtain consistent values. Nonetheless, pH-dependent SBQ and CRET patterns were identical for inter and intramolecular Cerenkov imaging, regardless of normalization, which allowed us to move forward.

In vitro studies were performed using triple negative breast cancer cell lines MDA-MB-231 and its metastatic variant 4175-Luc+. These cell lines were chosen as our model because they show differential expression of LDHA, which catalyzes the conversion from pyruvate to lactate, whose co-secretion with a proton decreases TME

pH. 4175-Luc+ cells have increased LDHA expression, compared to MDA-MB-231. Thus, we hypothesized that they would exhibit increased acidity *in vitro* and *in vivo*.

NFbD showed no cell toxicity and no intracellular uptake. These were considered positive observations for *in vivo* imaging, since we are interested in measuring a metabolic by-product excreted by cells into the extracellular milieu. To better understand acidification patterns for both cell lines, media pH was measured after incubation with each cell line. Media from 4175-Luc+ cells was significantly more acidic than media from MDA-MB-231s after a 24-hr incubation period. This result was promising, but when measuring glucose consumption and lactate production for each cell line there were no significant differences. This led us to explore other viable options for modeling pH changes that could be applied *in vivo*.

LDH inhibitors, Compound 5 (Rai et al., 2017) and GSK 2837808A were tested in 4175-Luc+ cells, showing no changes in cell viability nor significant changes in lactate production. We expected these LDHi to show significant decrease in lactate production, since they work by inhibiting lactate dehydrogenases, but this was not the case. It is possible that our chosen cell line was not sensitive to the effects of LDHi. Over expression of LDHA/B could have played a role. It is also possible that increased acidification of 4175-Luc+ cell media has contributions from other mechanisms, such as overexpression of carbonic anhydrase or Na^{+}-H^{+} exchanger (Contreras-Baeza et al., 2019; Pavlova and Thompson, 2016; Webb et al., 2011).

4.5 Conclusion

Cerenkov SBQ and CRET were observed *in vitro* intermolecularly and intramolecularly with NFbD in a pH-dependent manner, allowing for construction of Cerenkov pH titration curves. *In vitro* experiments with NFbD using triple negative breast cancer cell lines MDA-MB-231 and 4175-Luc+ showed no toxicity. Cell acidification studies showed a significant decrease in pH from 4175-Luc+ media after 24-hour incubation, compared to MDA-MB-231 but there was no significant difference in glucose consumption or lactate production. Treatment with LDHi also did not alter glucose consumption or lactate production. Although *in vitro* pH modulation proved challenging, we were able to demonstrate that NFbD-Ga was sensitive to pH changes and was a promising candidate for in vivo testing.

Chapter 5

NFbD *In Vivo*

5.1 Introduction

Tumor acidity has been linked to poor prognosis on disease progression, including increased invasion, metastasis, and chemotherapeutic resistance (Wojtkowiak et al., 2011). Decreased pH in the TME provides an optimum environment for matrix metalloproteinases and cathepsins, enzymes that degrade the extracellular matrix, facilitating invasion and metastasis of cancer cells to other sites of the body (Wojtkowiak et al., 2011). Additionally, chemotherapeutics with basic pK_as can become ionized in an acidic extracellular milieu, contributing to chemotherapeutic resistance. Charged molecules are unable to passively cross the cell membrane, preventing them from reaching their intended intracellular target (Wojtkowiak et al., 2011). Pre-clinical assessment of tumor pH could provide insight on tumor status and offer an improved approach for *a priori* chemotherapeutic selection.

Cerenkov imaging has been used clinically to track radiotracers such as ^{131}I, ^{18}F-FDG and ^{68}Ga-PSMA and explored pre-clinically in combination with fluorophores, quantum dots and nanoparticles to visualize tumors and their metabolic activity (Pratt et al., 2021). pH detection using Cerenkov imaging is a novel application, studied previously in our lab with fluorinated naphthofluoresceins (Arroyo et al., 2019) and phenol- and sulfon-phthaleins (Czupryna et al., 2015). These studies were successful, but a more energetic Cerenkov emitter was of interest, in order to obtain a brighter and more

easily distinguishable pH-dependent signal. ^{68}Ga has an endpoint energy of 1,899 keV, which is higher than ^{18}F (688 keV), becoming our Cerenkov emitter of choice (Ciarrocchi and Belcari, 2017).

NFbD-Ga is a molecular construct able to provide itself with the energy needed to absorb and fluoresce, without the need for an external excitation source. Similar molecular constructs have also been studied by the Decréau group to assess CRET (Bernhard et al., 2014). The coupling of a fluorophore with a Cerenkov emitter transfers blue-weighted photons into longer wavelengths, which are less attenuated by tissue, ideal for *in vivo* applications (Thorek et al., 2013). CRET, also known as Secondary Cerenkov Induced Fluorescence Imaging (SCIFI), has been shown to have a signal to background ratio 5.7 times greater than that of fluorescence techniques (Pratt et al., 2021). NFbD-Ga promotes this energetic transfer in a pH-dependent manner, providing relevant information on tumor status.

5.2 Results

In vivo PET scans were done in a tumor bearing mouse injected intravenously with NFbD-Ga (~130 μCi) to assess probe biodistribution (Figure 5.1). NFbD-Ga did not accumulate in the tumor (red oval in Figure 5.1.A), and was observed primarily in the liver, bladder and GI tract. This mouse died around minute 105, which likely caused the sudden increase in signal from the bladder observed in Figure 5.1.B. Lack of tumor accumulation led us to continue using intratumoral injections of NFbD-Ga.

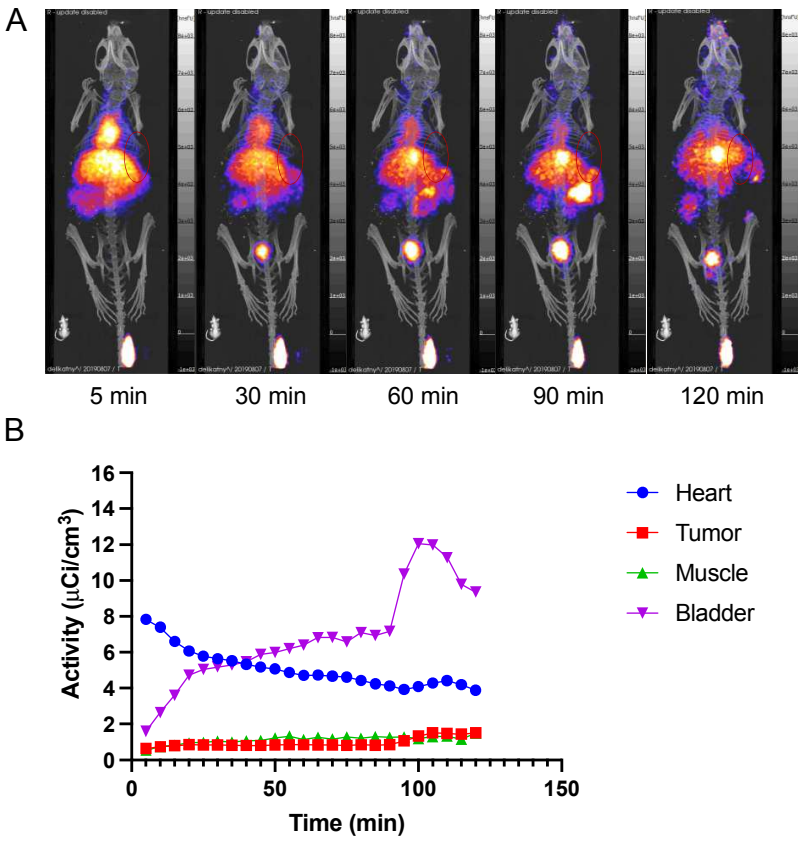

Figure 5.1. PET-Scan of tumor bearing mouse after intravenous injection of NFbD-Ga. *A.* PET scans of a tumor-bearing mouse after intravenous injection of NFbD-Ga (~130 µCi). Tumor marked as red oval. *B.* Biodistribution of NFbD-Ga as a function of time shows limited accumulation of NFbD-Ga in tumor.

Since pH determination using Cerenkov imaging depends on the pH-dependent absorption and fluorescence of NFbD, detection of SBQ and CRET *in vivo* was necessary. *In vivo* Cerenkov imaging was done after intratumoral injections of radioactive NFbD-Ga (~100 µCi) in athymic nude mice bearing 4175-Luc+ or MDA-MB-231 tumor xenografts. Figure 5.2.A is a representative Cerenkov image of 4175-Luc+ tumor bearing mice, showing SBQ and CRET at 600 and 700 nm respectively. These phenomena can be visualized with the naked eye. The image on the right, corresponding to CRET shows an increase in brightness in each of the tumors, compared to their corresponding tumors on

the left, which have a more attenuated signal (SBQ). These changes in signal are quantified in Figure 5.2.B.

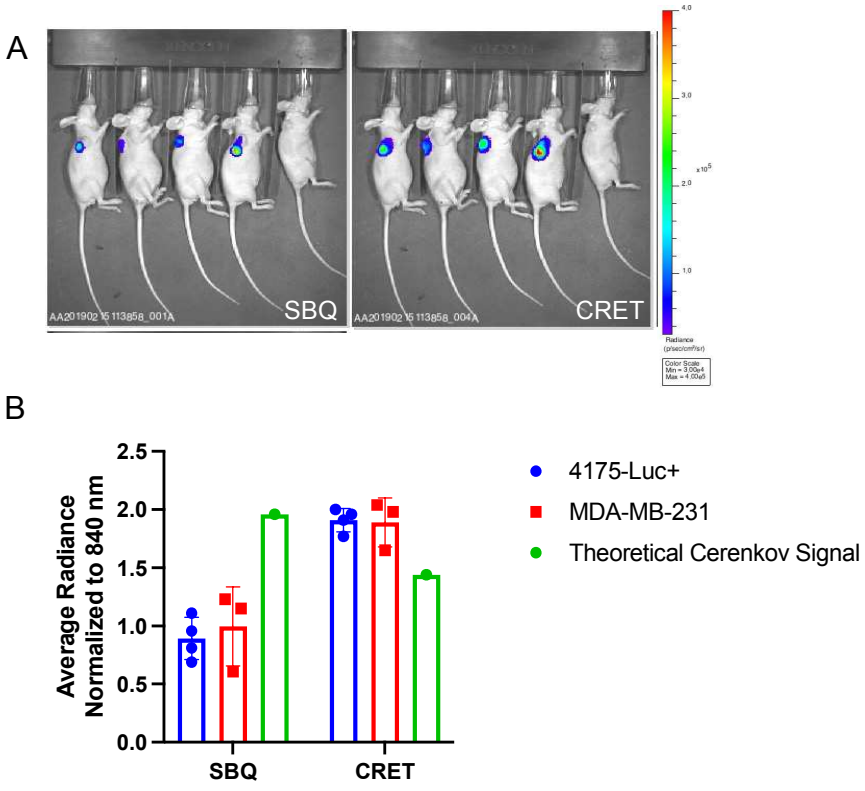

Figure 5.2. ***SBQ and CRET are observed*** **in vivo** ***with NFbD Cerenkov imaging.*** Athymic nude mice bearing 4175-Luc+ or MDA-MB-231 tumors were injected intratumorally with ~100µCi NFbD-Ga. *A*. Representative Cerenkov image of 417-Luc+ tumor bearing mice showing *in vivo* SBQ at 580 nm (left) and *in vivo* CRET at 700 nm (right). *B*. Average radiance signal normalized to 840 nm showing measured SBQ and CRET *in vivo* for 4175-Luc+ tumor bearing mice (blue bar) and MDA-MB-231 tumor bearing mice (red bar). Theoretical Cerenkov signal was calculated as $I=1/\lambda^2$, normalized to 840 nm (green bar). Unpaired t-test SBQ P-value > 0.05 and CRET P-value > 0.05.

In addition to detecting SBQ and CRET, Figure 5.2.B shows a direct Cerenkov imaging comparison of MDA-MB-231 and 4175-Luc+ cell lines. As discussed previously, these cell lines were expected to show differentiable acidification patterns, making them potential in vivo models for pH. Quantification and comparison of both

SBQ and CRET however, does not show significant differences between the cell lines. An interesting observation is that, even though the differences in signal are not significant, MDA-MB-231 shows a slightly higher SBQ signal and slightly less CRET. Considering our fluorophore, an increased SBQ signal would mean that there is less absorption by the basic form of the molecule, and therefore a lower pH. If there is less absorption, there will be less fluorescence, observed as reduced CRET. Since our proposed cell line model comparison was not as robust as expected, future experiments were performed only on 4175-Luc+ tumor xenografts.

To determine the ability of NFbD-Ga to accurately provide pH measurements, the probe was injected intratumorally (~40 μCi) into 4175-Luc+ tumor bearing mice and imaged using Cerenkov imaging (Figure 5.3.A). As seen above, SBQ and CRET were once again observed *in vivo,* and Cerenkov pH values were obtained ($pH_{Cerenkov}$ = 6.9 ± 0.2) by interpolation from *in vitro* NFbD Cerenkov pH titration curves, using CRET ratios previously described by Piwnica-Worms (Dothager et al., 2010). CRET ratios (Equation 5.1) are obtained by subtracting a quotient corresponding to the Cerenkov signal within a spectral window (i.e., CRET/SBQ), with no fluorophore present, from a quotient corresponding to Cerenkov signal within the same spectral window, in the presence of a fluorophore (Bernhard et al., 2017; Dothager et al., 2010).

$$CRET_{700\ nm} = \frac{Cerenkov+Fluorophore_{700\ nm}}{Cerenkov+Fluorophore_{600\ nm}} - \frac{Cerenkov_{700\ nm}}{Cerenkov_{600\ nm}} \qquad \text{Equation 5.1}$$

where Cerenkov+Fluorophore$_{700\ nm}$ corresponds to the CRET signal in the presence of NFbD, Cerenkov+Fluorophore$_{600\ nm}$ corresponds to SBQ signal in the presence of NFbD, and only Cerenkov corresponds to Cerenkov signal without NFbD present.

The pH values obtained from these tumors through Cerenkov imaging were validated against a well-established method for pH determination, ^{31}P-Magnetic Resonance Spectroscopy (MRS). pH values obtained from ^{31}P-MRS, were comparable to pH values obtained through Cerenkov imaging ($pH_{31\text{-}P\ MRS} = 6.92 \pm 0.04$), as seen in Figure 5.3.C. The spectra from which ^{31}P-MRS pH values were obtained are shown in Figure 5.3.D-H, where the chemical shift of 3-APP is referenced to the α-NTP resonances (depicted by blue arrows).

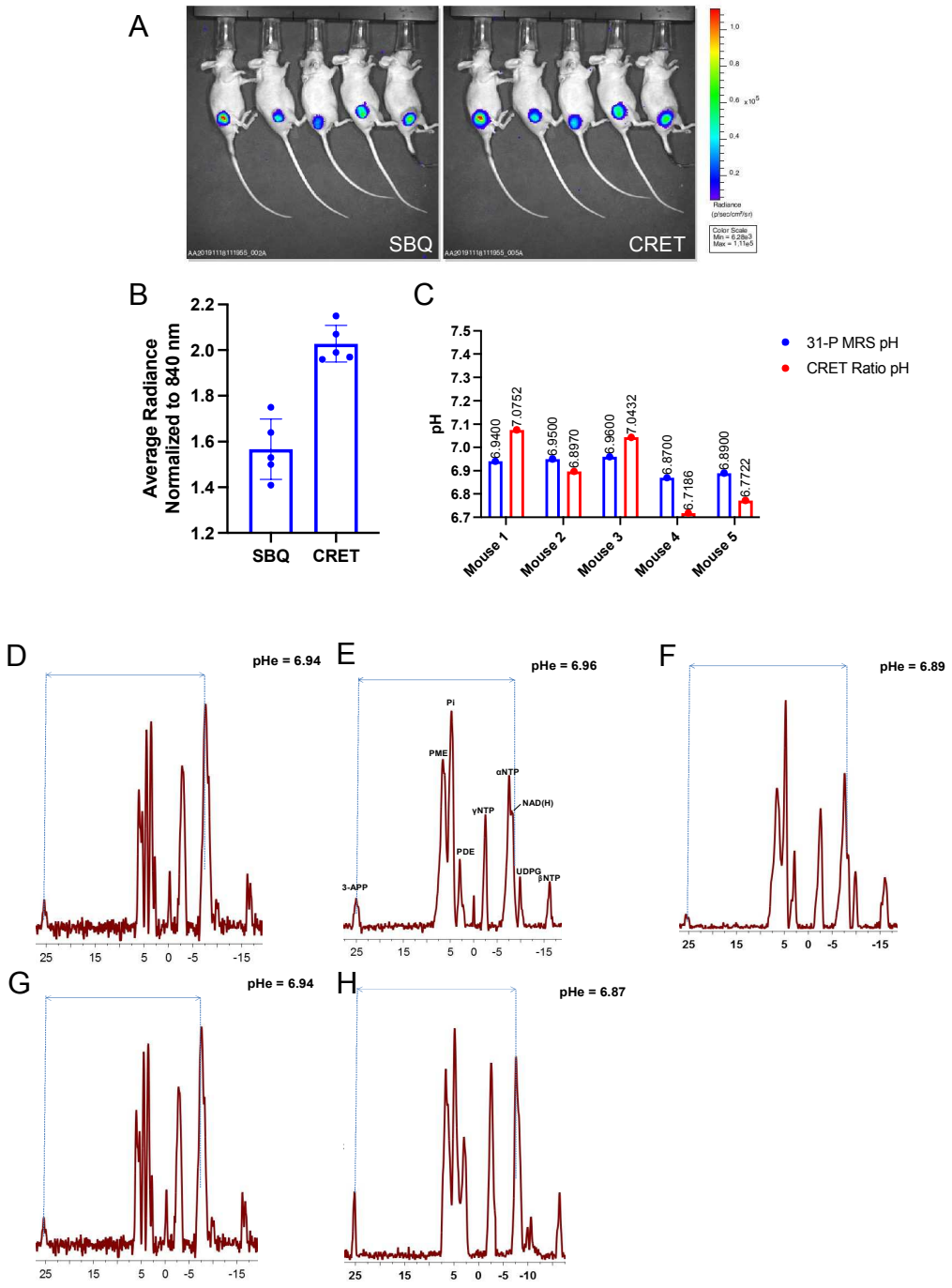

Figure 5.3. ***Validation of Cerenkov pH measurements by ^{31}P Magnetic Resonance Spectroscopy.*** *A*. Cerenkov images of SBQ (left) and CRET (right) of nude mice bearing 4175-Luc+ tumors injected intratumorally with ~40 µCi of NFbD-Ga. *B*. Average radiance signal normalized to 840 nm showing measured SBQ and CRET *in vivo*. *C*. pH values measured through Cerenkov imaging (pH = 6.9 ± 0.2) and validated with ^{31}P-MRS (pH = 6.92 ± 0.04). *D-H*. ^{31}P-MRS spectra for each mouse in *A* and its corresponding pH value.

To determine if Cerenkov imaging can detect pH changes *in vivo*, animal models for the modulation of pH were investigated. Athymic nude mice bearing 4175-Luc+ tumors were injected both intratumorally and in the muscle of the hind limb with NFbD-Ga (~35 µCi). The hypothesis of this experiment was to compare, in the same mouse, the acidic environment of the tumor to that of the muscle, which should present physiological pH of 7.4 (Jo et al., 2017). Cerenkov pH values measured for the tumor (pH = 7.3 ± 0.5) were similar to the pH values measured for muscle (pH = 7.2 ± 0.2) for these mice, indicating that additional approaches to pH modulation may be required.

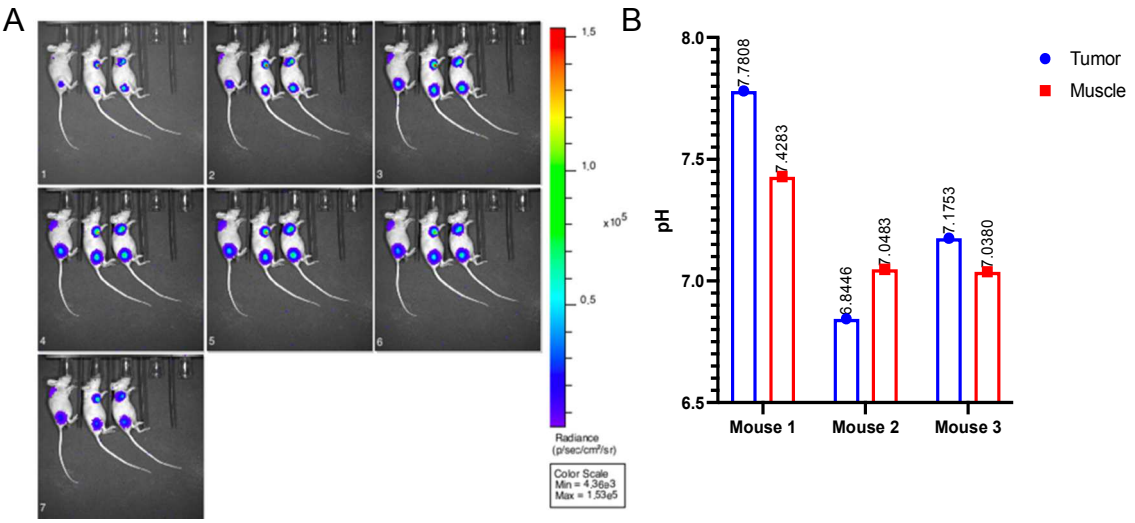

Figure 5.4. In vivo *Cerenkov imaging of 4175-Luc+ tumors with muscle as an internal control.* *A*. Cerenkov images of athymic nude mice bearing 4175-Luc+ tumors on the right shoulder, injected with ~35 µCi NFbD-Ga intratumorally and in the hind muscle (Images are shown using 580 nm, 600 nm, 620 nm, 680 nm, 700 nm, 720 nm, 840 nm emission filters). *B*. pH values measured through Cerenkov imaging for muscle (pH= 7.2 ± 0.2) and tumor (pH= 7. 3 ± 0.5), for each mouse in *A*.

In the next model for in vivo pH modulation (Zhao et al., 2021), athymic nude mice bearing 4175-Luc+ tumors were injected intratumorally with NFbD-Ga (~23 µCi) and imaged with Cerenkov imaging before and after intratumoral injections of bicarbonate (Figure 5.5.A). The pH values calculated for each tumor before bicarbonate injections (pH = 6.9 ± 0.3), are shown in Figure 5.5.B. The CRET ratio obtained from Mouse 3 before bicarbonate injections was low and did not fit the Cerenkov pH titration

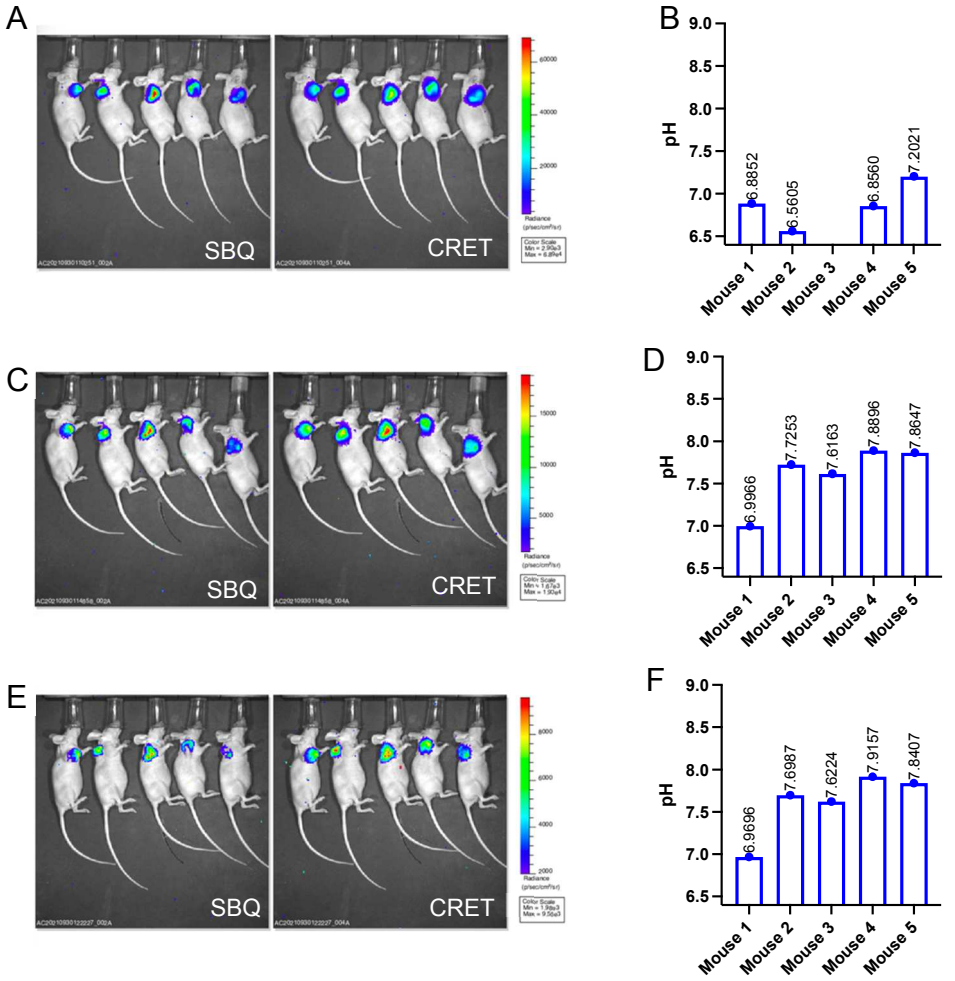

Figure 5.5. In vivo *pH modulation with intratumoral injections of sodium bicarbonate.* *A. In vivo* Cerenkov imaging of 4175-Luc+ tumor-bearing mice after intratumoral injection of naphthofluorescein (0.11 mM) and ^{68}Ga (~23 µCi), showing SBQ and CRET. *B.* Calculated Cerenkov pH values for each tumor (pH = 6.9 ± 0.3). *C. In vivo* Cerenkov imaging of mice in *A* after intratumoral injection of 10 µL sodium bicarbonate (200 mM). *D.* Calculated Cerenkov pH values for each tumor in *C,* (pH = 7.6 ± 0.4). *E. In vivo* Cerenkov imaging of mice in *A* and *B*, after intratumoral injection of 50 µL sodium bicarbonate (200 mM). *F.* Calculated Cerenkov pH values for each tumor in *E,* (pH = 7.6 ± 0.4).

curve. Each tumor was then injected intratumorally with 10 µL 200 mM sodium bicarbonate to increase pH locally, and imaged again Figure 5.5.C (Zhao et al., 2021). After bicarbonate injection, tumor pH values increased to pH= 7.6 ± 0.4 (Figure 5.5D). An additional 50 µL of bicarbonate was injected in an effort to push the system further but pH was not affected (Figure 5.5.E &F).

5.3 Discussion

This chapter describes the *in vivo* characterization of NFbD-Ga in athymic nude mice bearing triple negative breast cancer xenografts. First, PET imaging was performed to assess probe biodistribution. NFbD-Ga was observed in the liver, GI tract and bladder after intravenous injection. NFbD-Ga could be considered a large molecule, given its molecular weight, so hepatic clearance is reasonable. NFbD-Ga, however, had minimal tumor accumulation. Because of this, subsequent *in vivo* imaging experiments were conducted with intratumoral injections. In the future, NFbD targeting should be further explored to achieve higher probe accumulation in tumor after intravenous injections, to provide a more translatable approach.

For *in vivo* translation, SBQ and CRET must be detected in mice with Cerenkov imaging after injection with NFbD-Ga. Both SBQ and CRET were observed in athymic nude mice bearing 4175-Luc+ or MDA-MB-231 tumors. These changes in signal confirmed the detection of NFbD *in vivo*, particularly due to the presence of CRET. NFbD absorption occurs near the wavelength at which tissue absorbs, making SBQ subject to tissue absorption effects. On the other hand, Cerenkov-induced fluorescence is

solely due to the presence of a fluorophore. CRET is also an important phenomenon for *in vivo* pH-detection because it produces a bathochromic shift, allowing signal detection at wavelengths that are farther away from tissue absorption (Dothager et al., 2010).

As discussed in the previous chapter, the comparison between MDA-MB-231 and 4175-Luc+ tumors was intended to serve as an acidification model where 4175-Luc+ tumors exhibited increased acidification, compared to MDA-MB-231. Cerenkov imaging was done for both xenograft models after injection with NFbD-Ga and although the graph in Figure 5.2.B shows a slight difference in SBQ and CRET within the models, these were not significant. Since NFbD absorbs and fluoresces when it is in its basic or unprotonated form, our expected results were a significantly decreased SBQ signal in MDA-MB-231 tumors, and increased CRET, compared to 4175-Luc+ tumors. As clarification, increased attenuation by the basic form of the fluorophore is observed as a decrease in the signal labeled as SBQ. The photons that are being absorbed by the fluorophore will not be detected in the signal output.

To validate our Cerenkov pH values, athymic nude mice bearing 4175-Luc+ tumors were imaged using Cerenkov after NFbD-Ga injection. Cerenkov signals obtained, were used to interpolate Cerenkov pH values with previously described equation for CRET ratios, proposed by Piwnica-Worms (Dothager et al., 2010). The calculated pH values in the 4175-Luc+ tumors were 6.9 ± 0.2, which are within the expected tumor pH range (Estrella et al., 2013). ^{31}P-MRS was then performed on the same mice, yielding pH values of 6.92 ± 0.04. These were promising results since the pH values were comparable. Cerenkov pH values showed increased variation, compared to

^{31}P-MRS pH values. This could be due to the inherent resolution of the technique or to variations in intratumoral probe injection.

Muscle and tumor Cerenkov imaging was done to assess the technique's ability to detect pH changes in acidic tumor pH and the physiological pH in muscle. Muscle exhibited Cerenkov pH values of 7.2 ± 0.2, while tumors exhibited pH values of 7. 3 ± 0.5. These pH values were reasonable, but muscle pH was lower than expected. In an effort to obtain a robust pH response, tumors were injected intratumorally with sodium bicarbonate, to increase pH. Cerenkov pH values before bicarbonate injection were pH = 6.9 ± 0.3, and pH = 7.6 ± 0.4 after bicarbonate injections, showing a 0.7 pH increase. This change in pH can even be observed in the Cerenkov images in Figure 5.5.C as very bright CRET in the tumors.

5.4 Conclusion

These results demonstrate that Cerenkov imaging can detect pH changes *in vivo*, but highlight the limitations of the technique, which might not be sensitive enough to detect the discreet changes in pH expected in biological systems. Since the pH calculations are performed using ratios of CRET to SBQ, tissue absorption may affect the final results, especially at lower wavelengths. It is important to note that these studies provide proof of principle evidence for the potential of the technique, and additional fine-tuning could render this a powerful pre-clinical tool.

Chapter 6

In vitro Phantoms

6.1 Introduction

Cerenkov imaging *in vivo* poses a challenge due to Cerenkov radiation having its maximum intensity in the blue range of the spectrum, with intensity proportional to the inverse square of the wavelength, $1/\lambda^2$ (Demers et al., 2013). This spectral region is where tissue absorption and scattering occur, resulting in signal loss (Demers et al., 2013; Upputuri and Pramanik, 2019). One way to enhance *in vivo* signal is to transfer photons from these shorter, blue-weighted wavelengths to longer wavelengths, where tissue is more permeable to light. This red shift of photons can be done with fluorophores, nanoparticles, and quantum dots (Bernhard et al., 2017; Pratt et al., 2021; Thorek et al., 2014b). This approach has proven successful, but it has been observed that tissue can still cause Cerenkov signal attenuation in the presence or absence of these agents. Additional information regarding tissue effects would aid in understanding differential signal detection, particularly in agents such as NFbD, which report on tumor microenvironment.

Mathematical models for effective attenuation coefficients have been published (Habte et al., 2018). These calculations are helpful to understand how tissue absorption and scattering affect Cerenkov imaging, but these models were developed for direct comparison between PET and Cerenkov imaging. Their calculations do not consider a Cerenkov modulator, such as a fluorophore, which is the focus of this project. NFbD absorbs at 600 nm, which is in an area of the visible spectrum that is subject to signal attenuation due to tissue scattering and absorption. In order to obtain accurate pH measurements, signal contributions coming from tissue and NFbD should be properly

identified, to prevent over or underestimations of pH-dependent effects, which would ultimately affect the final readout.

To elucidate tissue effects directly affecting NFbD *in vivo* and the subsequent pH measurements obtained after Cerenkov imaging, several tissue phantoms were assessed. These phantoms included Intralipid and India ink, which represent tissue scattering and absorption media, respectively (Spinelli et al., 2014), bologna (Habte et al., 2018) and chicken (Carpenter et al., 2014; Spinelli and Boschi, 2015; Spinelli et al., 2011). Cerenkov spectra from these phantoms were evaluated, particularly at the wavelengths were SBQ and CRET occur.

6.2 Results

Phantom studies were conducted to elucidate the effects of tissue absorption and scattering on Cerenkov imaging with NFbD-Ga. Figure 6.1 shows a homogeneous phantom study using intralipid (Di Ninni et al., 2011) and India ink (Di Ninni et al., 2010), as scattering and absorption agents, respectively (Spinelli et al., 2014), with naphthofluorescein and ^{68}Ga, at basic pH. Increasing concentrations of intralipid seem to have an amplification effect for Cerenkov signal, 3% intralipid exhibiting the highest signal (Figure 6.1.A). Interestingly, SBQ and CRET were not observed. India ink, shown in Figure 6.1.B, shows a lower Cerenkov signal than intralipid, with a typical $1/\lambda^2$ Cerenkov spectrum. SBQ and CRET were not observed. Similar spectra were observed when India ink was mixed with intralipid and for the naphthofluorescein control (Figure 6.1.C). Naphthofluorescein concentration might have been too low to exhibit SBQ and CRET for this experiment.

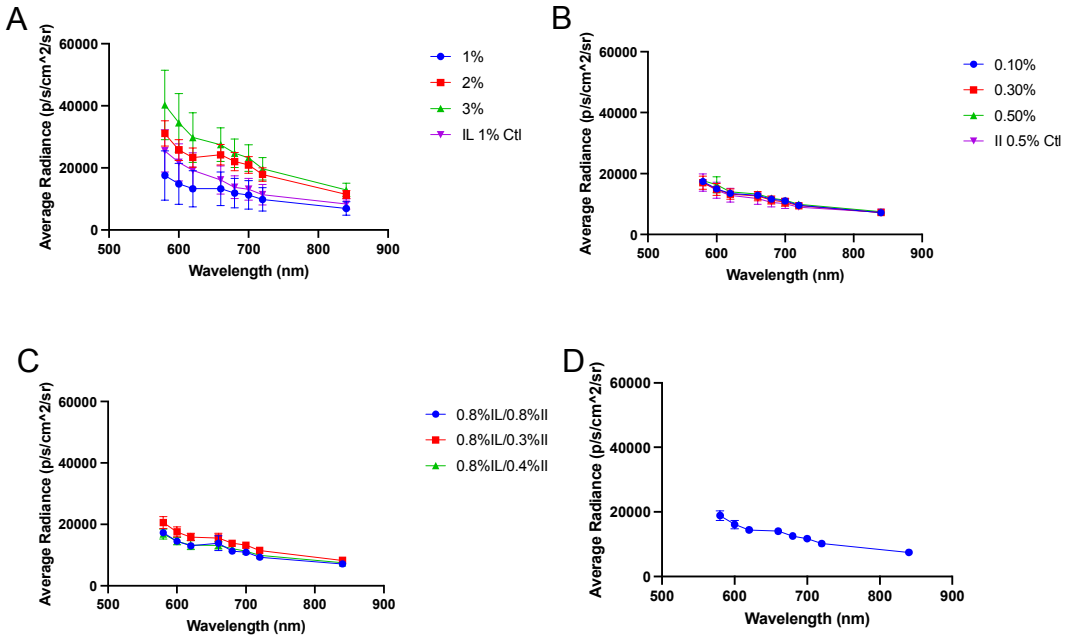

Figure 6.1. ***Intralipid and India Ink homogeneous phantom*****.** Cerenkov imaging spectrum showing average radiance as a function of wavelength, for various concentrations of *A.*intralipid. *B.* India Ink. *C.* intralipid and India Ink. *D.* naphthofluorescein control. *A-D* contain 45.8 µM naphthofluorescein, ~30 µCi/well of ^{68}Ga, pH>8, for each well, except control.

To further address the effects of tissue absorption and scattering for Cerenkov imaging of tumor pH, tissue phantom studies were conducted. Figure 6.2 shows a tissue phantom using bologna of different thicknesses to cover wells containing Cerenkov emitters. Bologna was chosen due to the apparent homogeneity of this tissue. Figure 6.2.A and 6.2.B show Cerenkov images at 600 nm, 680 nm, 700 nm, and 840 nm for a well plate containing 240 µM naphthofluorescein and ^{68}Ga (~38 µCi) at pH>8 (left columns) and ^{68}Ga (~38 µCi) at pH>8 (right columns) with and without tissue. Figures 6.2 C-D show Cerenkov spectra corresponding to each of these conditions.

In Figure 6.2.C, a typical $1/\lambda^2$ Cerenkov spectrum is observed for the ^{68}Ga control. Figure 6.2.D shows the Cerenkov spectrum with naphthofluorescein present, exhibiting SBQ and CRET. In Figures 6.2.E and F, we observe Cerenkov spectra without and with naphthofluorescein, respectively. Both spectra show similar intensities, with an attenuation followed by an increase in signal at 2.5 mm and 3 mm, even when no

naphthofluorescein is present, suggesting tissue absorption and scattering. Signal obtained from 6 mm tissue is highly attenuated.

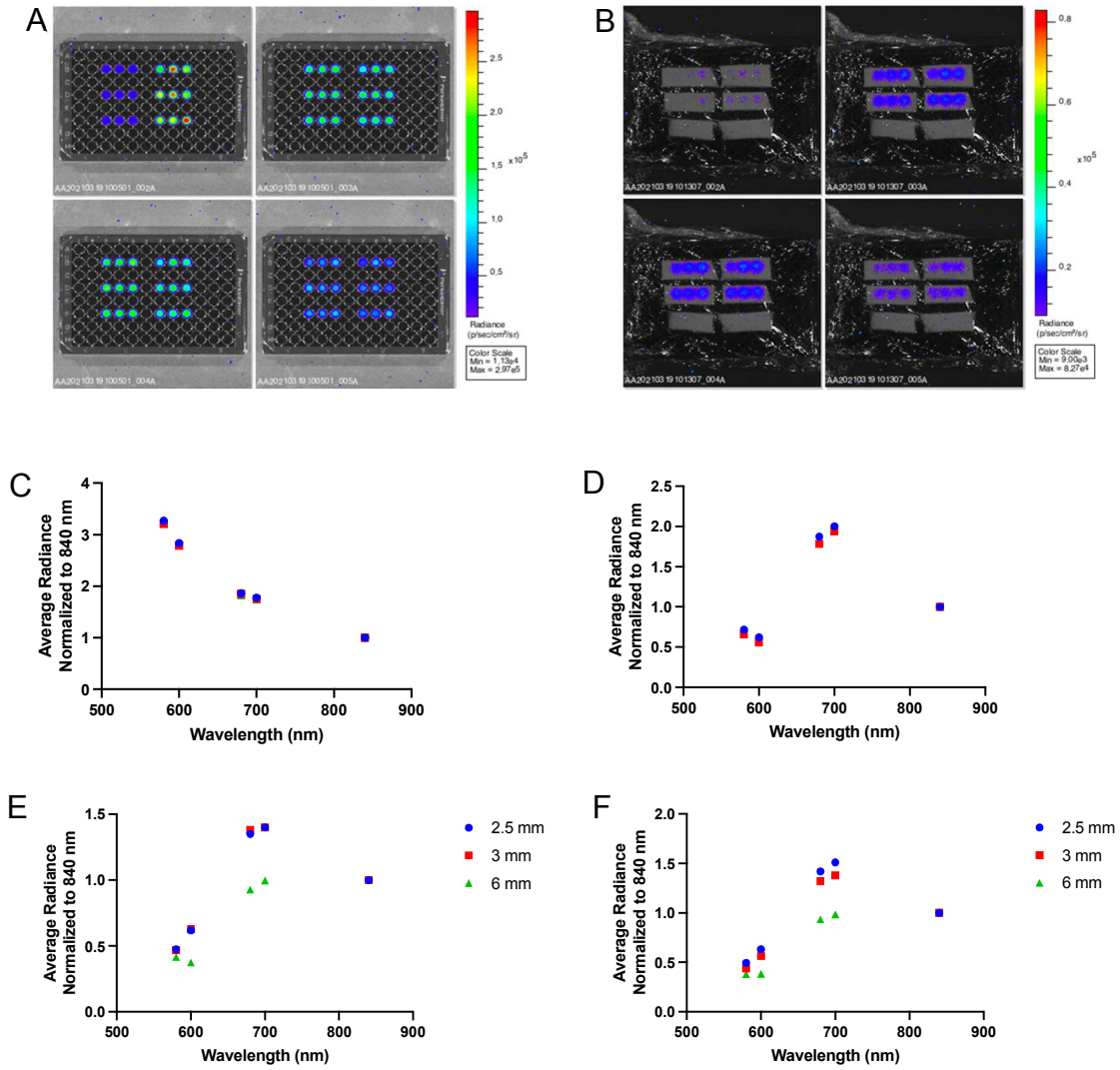

Figure 6.2. ***Effects of Bologna tissue on Cerenkov emission.*** *A-B.* Cerenkov images for a 96-well plate with and without bologna at 600 nm, 680 nm, 700 nm, and 840 nm. Cerenkov imaging spectrum showing average radiance as a function of wavelength for *C.* ~38 µCi/well of ^{68}Ga (pH>8). *D.* 240 µM naphthofluorescein and ~38 µCi/well of ^{68}Ga (pH>8). *E.* ~38 µCi/well of ^{68}Ga (pH>8), and 2.5 mm, 3 mm, or 6 mm bologna slices. *F.* 240 µM naphthofluorescein, ~38 µCi/well of ^{68}Ga (pH>8), and 2.5 mm, 3 mm, or 6 mm bologna slices.

In an effort to visualize tissue effects on a more relevant model, tumor tissue and skin tissue from tumor bearing mice were evaluated with Cerenkov imaging in a phantom model (Figure 6.3). Figure 6.3.A shows a Cerenkov image at varying wavelengths of a well-plate prepared with 240 μM naphthofluorescein and ~36 μCi ^{68}Ga at pH 4, 7.4 and 9.5. Naphthofluorescein was not present in the ^{68}Ga control. As seen in Figure 6.3.B, wells from Cerenkov imaging in Figure 6.3.A showed SBQ and CRET at pH 9.5 when taken as a ratio to 840 nm (green bars). Figure 6.3.C shows the plate in Figure 6.3.A with tissue slices over the wells, measuring ~2 mm in thickness. Tumor heterogeneity is detected as brighter spots in the same well covered with tissue. SBQ and CRET are not observed (Figure 6.3.D). In Figure 6.3.E, the same plate is covered with mouse skin, measuring ~1 mm in thickness. Less heterogeneity is observed, but no SBQ or CRET are present (Figure 6.3.E).

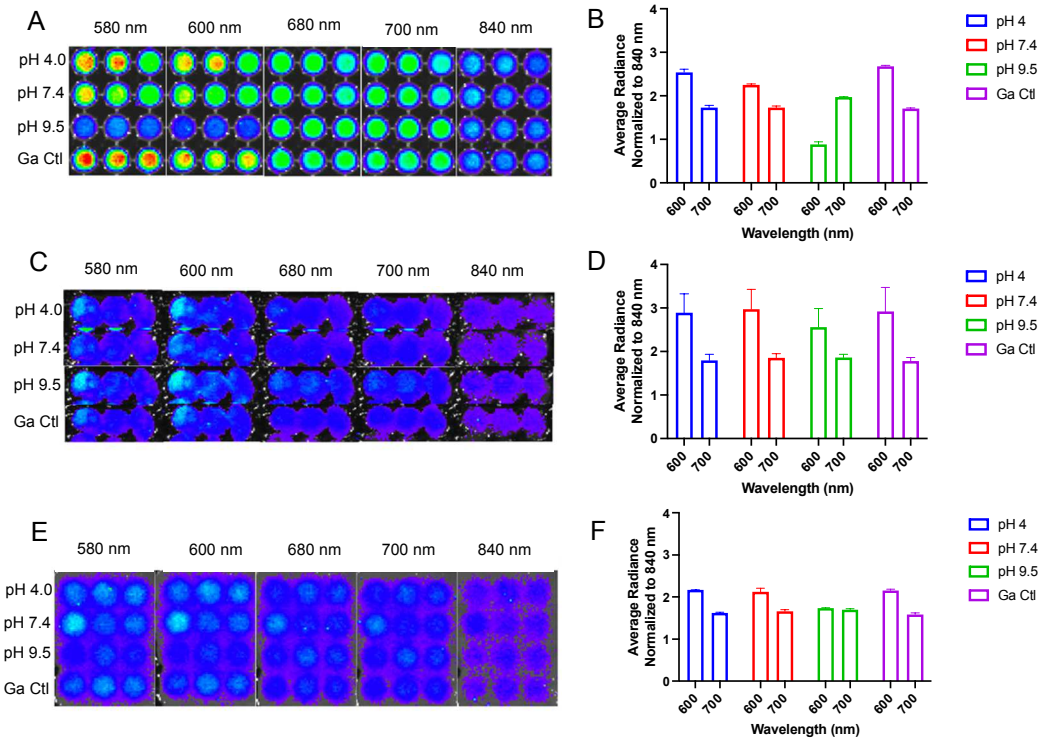

Figure 6.3. ***Phantom with mouse tumor tissue and skin tissue***. *A.* Well plate prepared with 240 µM naphthofluorescein and 36 µCi ^{68}Ga, at pH 4, 7.4 and 9.5. *B.* Cerenkov signal at SBQ and CRET for *A*, for each condition. *C.* Well-plate in *A*, with tumor tissue (~2 mm thick) over wells. *D.* Cerenkov signal at SBQ and CRET for *B*. *E.* Well-plate in *A,* with skin tissue (~1 mm) over wells. *F.* Cerenkov signal at SBQ and CRET for *E*. *B*, *D* & *F* are presented as ratios to 840 nm.

Since SBQ and CRET were not observed through skin in Figure 6.3, an experiment was conducted to determine whether skin attenuates Cerenkov signal and to what extent. In Figure 6.4, athymic nude mice bearing 4175-Luc+ tumor xenografts were injected intratumorally with NFbD-Ga (~27 µCi). These mice were imaged using Cerenkov imaging (Figure 6.4.A), and then euthanized. Skin over the tumors was removed (Figure 6.4.C), and the tumors were then excised (Figure 6.4.E) and halved (Figure 6.4.G). After each step, Cerenkov imaging was performed, and SBQ and CRET signals were plotted. In Figure 6.4.B, SBQ and CRET were observed for each mouse

after intratumoral injection of NFbD-Ga. Similarly, in Figure 6.4.D, SBQ and CRET were also observed, after skin removal, suggesting that SBQ and CRET can indeed be seen through skin. Tumor excision did not seem to increase SBQ and CRET detection, which could be due to a decrease in activity (Figure 6.4.F & H).

Because of the apparent SBQ and CRET observed in the bologna phantoms, results presented in Figure 6.4 required further investigation, which led us to our final tissue phantom using raw frozen chicken breast. Figure 6.5.A and B show Cerenkov images of a well plate prepared with 240 μM naphthofluorescein and ~22 μCi ^{68}Ga at various pH values, with or without chicken tissue. Chicken tissue was chosen because of increased tissue uniformity, in terms of heterogeneity and thickness. SBQ and CRET were observed with no chicken tissue at pH 9.5, in Figure 6.5.C (green bars). When chicken tissue was added (1 mm), SBQ and CRET were still observed at pH 9.5. This effect is also observed with 2 mm of tissue (Figure 6.5.E). Tissue effects begin to obscure SBQ and CRET at 3 mm (Figure 6.5.F).

This chicken phantom provided useful additional information. In the absence on naphthofluorescein, 1 mm of tissue attenuated 64% of the Cerenkov signal. With the addition of naphthofluorescein, signal is further attenuated to 17%. In the absence of tissue, naphthofluorescein attenuated 82% of the signal, solely corresponding to SBQ.

there was also a 10% increase in Cerenkov signal due to CRET. For this technique, the depth penetration is 3 mm.

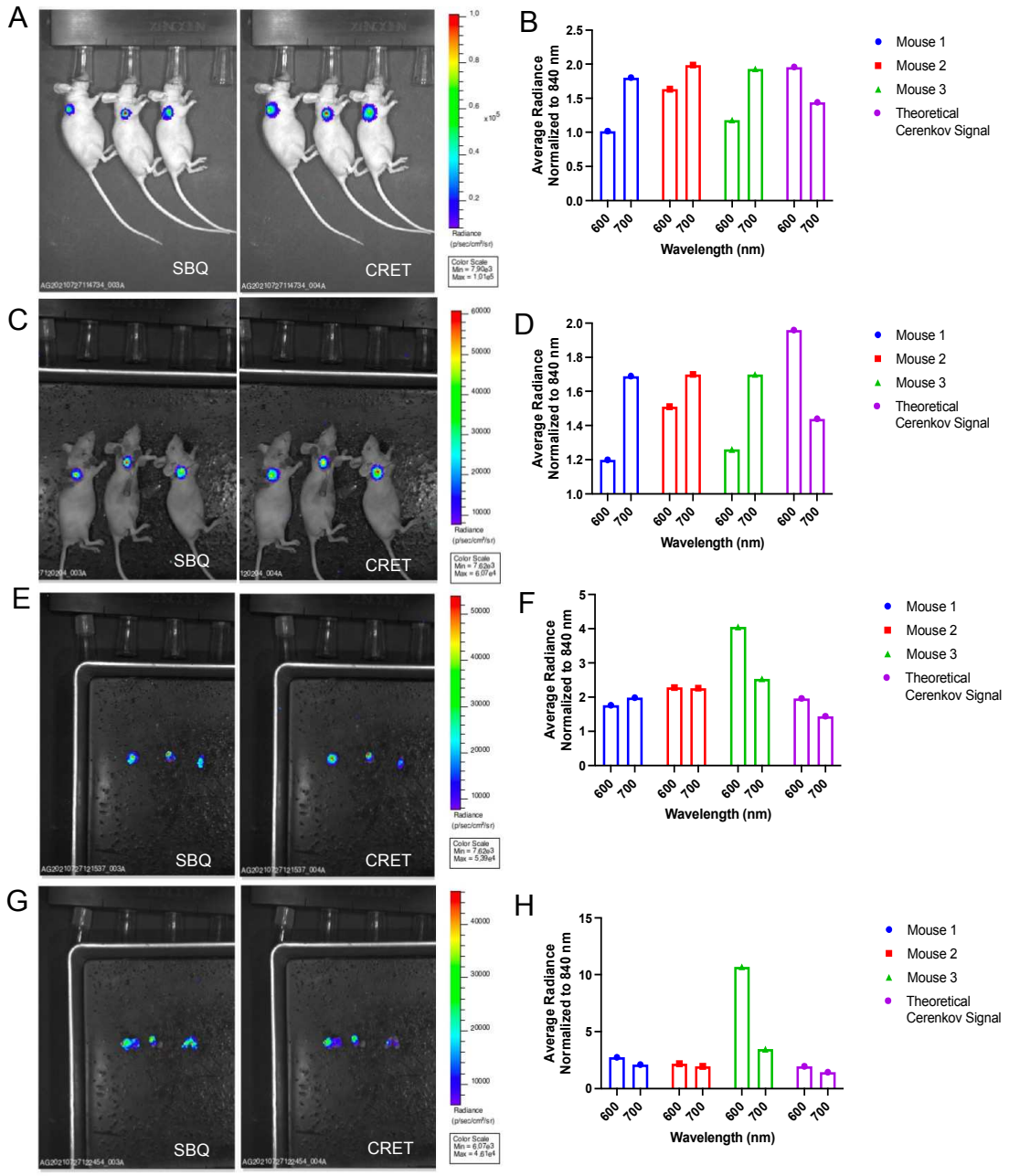

Figure 6.4. In vivo *SBQ and CRET observed through skin.* *A*. Cerenkov images of athymic nude mice bearing 4175-Luc+ tumors injected intratumorally with NFbD-Ga (~27 µCi). *B*. Quantification of SBQ and CRET spectra from these images. *C.* Cerenkov images of exposed tumors (removed skin) from euthanized mice. *D.* Quantification of SBQ and CRET. *E.* Cerenkov imaging of excised tumors. *F.* Quantification of SBQ and CRET. *G.* Cerenkov images of tumors in *E*, sliced in half, with SBQ and CRET quantified in *H.*

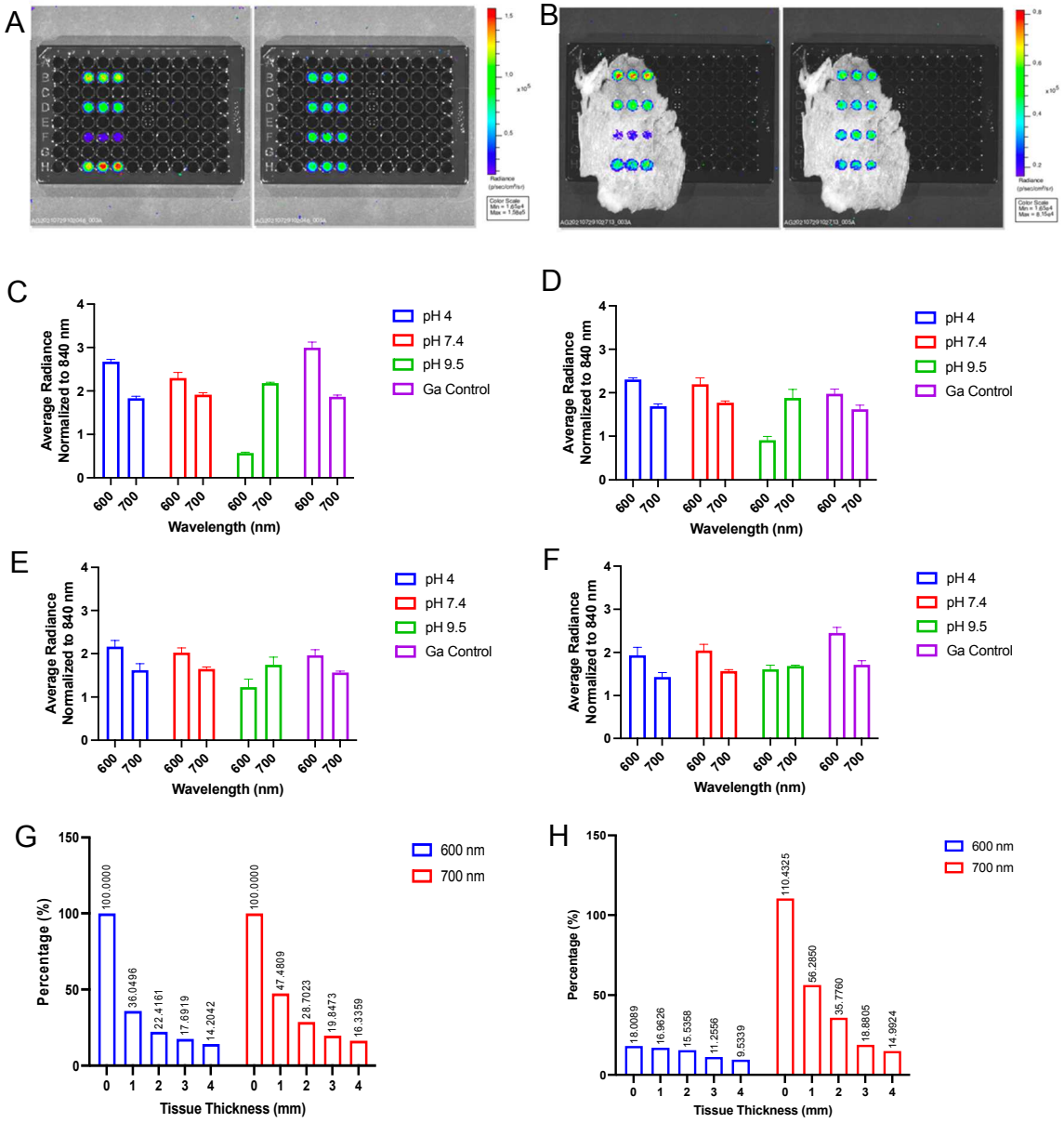

Figure 6.5. ***Effects of chicken breast tissue phantom on Cerenkov emissions.*** *A.* Cerenkov images of well plate prepared with 240 µM naphthofluorescein and ~22 µCi ^{68}Ga, at pH 4, 7.4 and 9.5 at SBQ (600 nm, left) and CRET (700 nm, right). *B.* Representative Cerenkov images of the well plate with a 1 mm chicken slice at SBQ (left) and CRET (right). *C.* Cerenkov signal at SBQ and CRET of conditions in *A*. *D.* Cerenkov signal at SBQ and CRET of conditions in *A,* with a ~1 mm slice of chicken. *E.* Quantification of Cerenkov signal at SBQ and CRET of conditions in *A,* with a ~2 mm slice of chicken. *F.* Cerenkov signal at SBQ and CRET of conditions in *A,* with a ~3 mm slice of chicken. *G.* Percent of tissue attenuation signal as a function of tissue thickness (no naphthofluorescein). *H.* Percent signal from naphthofluorescein relative to gallium control as a function of tissue thickness.

6.3 Discussion

This chapter evaluated tissue phantoms applied to our proposed technique of pH determination by Cerenkov imaging. Intralipid and India ink have been previously used to simulate tissue scattering and absorption (Alexander et al., 2021; Axelsson et al., 2011; Demers et al., 2013; Spinelli et al., 2014; Tendler et al., 2020). The homogeneous phantom presented in Figure 6.1, as Cerenkov spectra of average radiance as a function of wavelength showed an amplification of Cerenkov signal as Intralipid concentration increased. We believe this is due to an increase in refractive index, which has a linear relationship with intralipid concentration (Ding et al., 2005). The Frank-Tamm equation shows that Cerenkov intensity is proportional to refractive index, exhibiting a higher intensity within a medium with increasing refractive index (Ciarrocchi and Belcari, 2017; Mitchell et al., 2011). These spectra, however, did not exhibit SBQ or CRET, which is probably due to the low concentration of naphthofluorescein, confirmed by the absence of SBQ and CRET in the naphthofluorescein control. Since homogenous phantoms of Intralipid and India ink did not accurately reflect the effects of tissue, we abandoned this model system and switched to tissue phantoms.

It is important to note that this chapter mainly includes data obtained with naphthofluorescein mixed with ^{68}Ga. The reason for this is twofold. First, by the end of the experiments, the activity available from the ^{68}Ga generator had decreased to a point where the volume needed to obtain the required activity was very high (See Appendix). Second, imaging with the widely available naphthofluorescein parent compound was more economical compared to using the NFbD probe. Here the assumption was made that

intermolecular imaging with naphthofluorescein behaved identically to NFbD, given that it is the parent fluorophore of our probe, and that we demonstrated that the optical properties were maintained after conjugation.

The goal of using tissue phantoms was to understand how tissue effects affect SBQ and CRET, and to be able to separate the signal modulations of NFbD from that arising from tissue. In Figure 6.2, a bologna tissue phantom was presented, in which a well plate containing naphthofluorescein and ^{68}Ga at basic pH was imaged using Cerenkov with and without bologna slices of various thicknesses (2.5 mm, 3 mm and 6 mm) placed on top. A similar model was used by Habte et al. (2018). Without tissue, the Cerenkov spectra behaved as expected, with a typical $1/\lambda^2$ Cerenkov dependence when there was no naphthofluorescein present and with SBQ and CRET observed in the presence of naphthofluorescein. In the presence of bologna however, Cerenkov spectra exhibited similar characteristics with and without naphthofluorescein. Signal was attenuated at 600 nm, which is the wavelength where maximum SBQ occurs for naphthofluorescein. Tissue absorption also occurs at 600 nm (Upputuri and Pramanik, 2019). At 700 nm, where CRET occurs, there is an increase in signal, compared to 600 nm. Since this is observed in the presence and absence of naphthofluorescein, we can conclude that observed changes arise mostly from tissue effects. If tissue did not absorb near 600 nm, Figure 6.2.E would likely look similar to Figure 6.2.C. As expected, the Cerenkov signal decreased with increasing tissue thickness.

Since bologna was too opaque to be able to see SBQ and CRET from naphthofluorescein, a more realistic model of mouse tumor and skin tissue were studied (Figure 6.3). SBQ and CRET were observed at pH 9.5 from wells containing naphthofluorescein and ^{68}Ga and no tissue. SBQ and CRET were not observed with tumor tissue or skin, which could be due to both tissue effects and low ^{68}Ga activity. With this phantom, tumor heterogeneity was evident in the Cerenkov images. In Figure 6.3.C there are tumor areas in the same well that show increased brightness, corresponding to more transparent tumor tissue within the tissue slice.

To better understand the effects of skin. NFbD-Ga (~27 μCi) was injected intratumorally into tumor bearing mice and imaged using Cerenkov imaging. The mice were then euthanized., the skin over the tumor removed and Cerenkov imaging was performed again. Apparent SBQ and CRET were observed through skin and without skin, SBQ and CRET were not observed in excised tumor, even when sliced in two, although the signal did increase markedly.

The chicken phantom in Figure 6.5 provided important information regarding contributions of naphthofluorescein to SBQ and CRET. A plate was prepared with naphthofluorescein and ^{68}Ga, at various pH values and 1 mm slices of chicken breast tissue were placed over the wells and imaged, up to 3 mm tissue, where signal began to attenuate. SBQ and CRET were observed for 1 mm and 2 mm of tissue, suggesting the maximum depth penetration of this technique to be 3 mm. In addition to this, contributions of tissue attenuation to SBQ were determined. 64% of signal was attenuated

with 1 mm of tissue with no naphthofluorescein. When naphthofluorescein is added, there is a further attenuation to 17%. Impressively, when there was no tissue present, naphthofluorescein attenuated 82% of the signal. This phantom was analyzed using a 25% threshold per ROI in Living Image, because of low activity.

This chapter highlighted some factors to consider when applying this technique. Cerenkov imaging with NFbD should be directed to superficial applications, given the depth penetration of 3 mm, where tissue begins to obscure measurable signal. Achieving CRET is of utmost importance for detection of NFbD, due to its absorption wavelength being subject to tissue effects. Loss of activity plays a critical role in signal detection and differentiation, as well as probe concentration, both of which were discussed in Chapter 4. Based on these caveats, this technique may need additional optimization in order to be described as quantitative.

6.4 Conclusion

This chapter provides examples of various phantoms to assess tissue effects playing a role in SBQ and CRET detection for this project. An appropriate phantom model was developed using chicken breast. With this phantom, higher tissue uniformity was achieved, which allowed the depth penetration of the technique to be determined. Additionally, the contribution from tissue and naphthofluorescein to signal attenuation was assessed and determined.

Chapter 7

Conclusions and Future Directions

7.1 Introduction

This chapter will summarize the main takeaways and conclusions of the work presented in this thesis and provide a framework that describes the future directions of this project.

7.2 Conclusion Summary and Significance

The work presented in this thesis focused on the development, characterization and application of NFbD-Ga, a pH sensitive imaging probe, designed to report on TME acidity *in vivo*. Our approach toward this goal was systematic and each step built upon the previous one.

NFbD was successfully conjugated and chelated to ^{68}Ga. NFbD was shown to maintain the pH sensitivity and optical properties of its parent compound 5(6)-carboxynaphthofluorescein, which was vital to perform Cerenkov imaging and pH determination *in vivo.* NFbD coupling with ^{68}Ga as a Cerenkov emitter proved to provide pH-dependent selective bandwidth quenching (SBQ) and subsequent Cerenkov radiation energy transfer (CRET). This coupling was achieved intermolecularly, with ^{68}Ga mixed with NFbD, and intramolecularly, with NFbD chelated with ^{68}Ga.

Three relevant observations were obtained from these experiments. Firstly, intermolecular and intramolecular Cerenkov imaging exhibited different intensities, but identical pH dependent SBQ and CRET patterns. Intermolecular Cerenkov imaging

presented a higher signal than intramolecular Cerenkov imaging. Second, Cerenkov pK_a for intermolecular and intramolecular imaging were lower than the ones obtained through optical spectroscopy. This has been previously observed by Czupryna et al. and Arroyo et al. (Arroyo et al., 2019; Czupryna et al., 2015). The reason for this phenomenon is yet to be determined. Lastly, we observed that data normalization to 600 nm, which is the wavelength at which SBQ occurs for our probe, showed increased CRET, aiding in data visualization.

For *in vivo* pH determination, Cerenkov imaging was performed on athymic nude mice bearing triple negative breast cancer 4175-Luc+ tumors and average signal values obtained were used to interpolate pH values from *in vitro* pH titration curves. These pH values were ultimately calculated as CRET Ratios, described by Piwnica-Worms and his group (Dothager et al., 2010). Experimental pH values obtained from Cerenkov imaging were validated against ^{31}P-MRS. Data interpretation was faced with the challenge of tissue effects, which we aimed to elucidate through phantoms. Our proposed chicken tissue phantom (Carpenter et al., 2014; Spinelli and Boschi, 2011; Spinelli et al., 2011) provided valuable insight into the individual contributions of tissue and naphthofluorescein to attenuation. These studies provided insight into an application of Cerenkov imaging that could benefit from optimization, growth, and development.

This thesis aims to introduce a novel application to Cerenkov imaging, which provides functional information on the tumor microenvironment, offering an alternative for the pre-clinical assessment of acidity. As mentioned previously, acidity in the TME is

linked to invasion and metastasis and resistance to chemotherapeutics. Magnetic Resonance Imaging (MRI) techniques have been studied for measurement of TME acidity, such as chemical exchange saturation transfer (CEST) (Anemone et al., 2021; Chen and Pagel, 2015; Tang et al., 2020). Optical imaging approaches, however, are generally less expensive and provide high sensitivity (Peñate Medina et al., 2021).

7.3 Future Directions

This work can be described as proof-of-principle studies for the development of a novel application of Cerenkov imaging, namely using this technique to report on TME pH. Significant strides were achieved towards this goal, but further optimization should

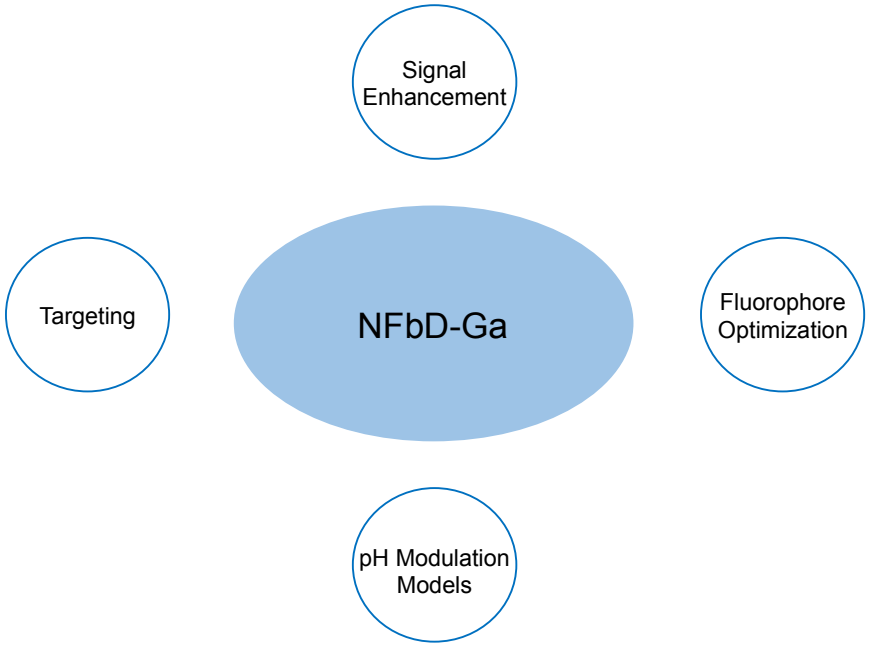

Figure 7.1. ***Summary scheme for NFbD-Ga Optimization.*** NFbD-Ga and its applications could be optimized by exploring targeting, signal enhancement and additional or modified fluorophores. This model could be explored more accurately with optimized pH modulation models.

be explored to obtain more sensitive and accurate pH measurements. Figure 7.1 provides a global summary of what we believe this optimization should entail.

Since NFbD-Ga has minimal tumor absorption, targeting alternatives should be explored to optimize delivery. The synthesis for an updated molecular scaffold for NFbD-Ga was developed by Dr. Anatoliy Popov. This scaffold consists of a trisubstituted aminotriazine, to which 5(6)-carboxynaphthofluorescein, DOTA and a targeting moiety can be linked, as seen in Figure 7.2. A moiety such as an RGD peptide, which is the main binding domain of several extracellular matrix proteins like fibronectin and fibrinogen and can bind to multiple types of integrins (Bellis, 2011), can be considered for active targeting (Agnello et al., 2021; Chadar et al., 2021; Hwang et al., 2020; Kutova et al., 2019; Mamnoon et al., 2021).

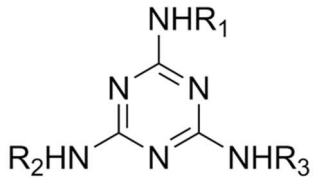

Figure 7.2. ***Proposed Structure for NFbD Targeting Scaffold.*** Trisubstituted aminotriazine capable of linking a fluorophore, a targeting moiety and a chelator.

The molecular construct in Figure 7.2 provides the flexibility to incorporate alternate fluorophores, chelators and targeting moieties, according to the desired target. This adds an avenue to consider additional pH-sensitive fluorophores that could enhance our *in vivo* Cerenkov pH measurements by presenting optical properties better suited to our proposed application. 5(6)-Carboxynaphthofluorescein was able to detect pH changes, but its pK_a is relatively high, making tumor pH measurements (pH =6.5-6.9)

challenging (Estrella et al., 2013). A fluorophore like SNARF-5F ($\lambda_{abs/ex}$= 573 nm/631 nm, EC 49,000 $M^{-1}cm^{-1}$, pK_a = 7.2), has a better pK_a for pH measurements of the TME, although its absorption and emission wavelengths are less optimal. We have previously observed CRET with SNARF-1 ($\lambda_{abs/ex}$= 576 nm/635 nm, EC 48,000 $M^{-1}cm^{-1}$), which has similar optical properties as SNARF-5F, suggesting the feasibility of this approach (Figure 7.3) (ThermoFisher, 2022a, b).

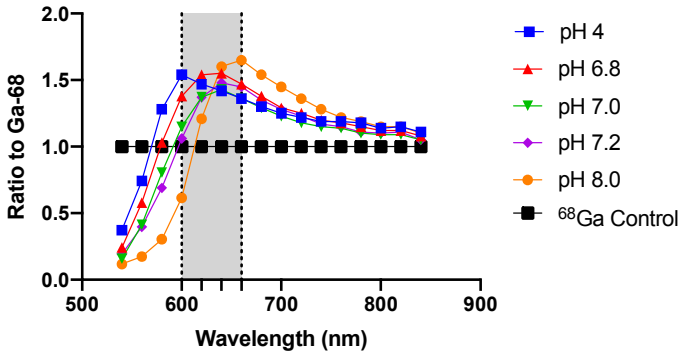

Figure 7.3. ***SNARF-1 Cerenkov Radiation Energy Transfer.*** Shaded region corresponds to CRET.

As mentioned previously, since Cerenkov radiation is blue-weighted, it exhibits higher intensities at shorter wavelengths. Incorporating a fluorophore with a large Stokes shift into our molecular construct could have the potential to transfer more photons to an area of the spectrum with enhanced tissue penetration. Such an example is presented by Jan Grimm and his group, through the use of dual-labeled nanoparticles with quantum dots and ^{89}Zr (Zhao et al., 2017). Although pH sensitivity could be a challenge, there have been reports of pH-sensitive quantum dots, providing a viable alternative (Manon et al., 2020; Tomasulo et al., 2006).

Signal enhancement of Cerenkov radiation could also be done by increasing the refractive index of the injection solution of NFbD-Ga. Cerenkov signal is proportional to the refractive index of the medium, so it is theoretically possible to modulate the intensity of the signal through adjusting the refractive index. Elucidating the optimal solution for injection, considering solvents such as saline and dextrose, could be of benefit. Additionally, Cerenkov signal can be enhanced by substituting the radioemitter ^{68}Ga to ^{90}Y, which has a higher endpoint energy (2280 keV) and a half-life of 64.1 hours. Using ^{90}Y would allow experimental procedures with extended time-points and provide a higher intensity signal.

To better understand the capabilities of NFbD-Ga to detect pH changes *in vivo*, additional pH modulation models should be elucidated. These models could include the genetic knockout of glycolytic enzymes such as LDHA using CRISPR/Cas9 to induce an alkalization effect. It has been reported that lactate secretion is not significantly affected through the knockout of either LDHA or LDHB. Both must be knocked out to see an effect (Ždralević et al., 2018). These knockouts did not affect *in vivo* tumor growth, which could allow for *in vivo* pH measurements. Pharmacological approaches for inhibiting LDH (Rai et al., 2017) or MCTs (Benjamin et al., 2018; Contreras-Baeza et al., 2019) could also be further explored.

7.4 Final Thoughts

With this thesis, we hope to introduce a novel application of Cerenkov imaging that could provide therapeutic benefit to oncologic patients. The field of Cerenkov

imaging has been developing greatly throughout the last decade. With each new discovery and application, this field demonstrates its amazing breadth and potential. Talented researchers around the world are working towards translating Cerenkov to the clinic, with clinical trials (ClinicalTrials.gov Identifier: NCT03484884) and developing imaging devices for the operating room (Ciarrocchi et al., 2021; Olde Heuvel et al., 2020; Olde Heuvel et al., 2019). These are exciting strides, that will take Cerenkov from bench to bedside.

Appendix

A.1. Regions of Interest (ROI)

Data analysis and processing is quintessential for any kind of quantitative imaging technique, including pH determination by Cerenkov imaging. Our standard processing workflow schemes are shown in Figure A.1. The Cerenkov imaging data was collected on an IVIS Spectrum and processed using the LivingImage Software from PerkinElmer. Representative images obtained on the IVIS Spectrum are shown on the left of Figure A.1, where all the mice are observed in a single image. This distance to the camera will depend on the field of view (FOV) settings determined before imaging. A larger FOV is used to take advantage of the high throughput capability of the IVIS, imaging 5 mice at once. Using LivingImage, regions of interest (ROIs) were drawn on the white light image of the tumor, followed by measurement of the Cerenkov emission within that region at different wavelengths. We found that this method led to variable results for the same ROIs in the same studies (Figure A.1.A). Test-retest reproducibility, a method for evaluating a tool's reliability to obtain reproducible results (Balagurunathan et al., 2014; Vaz et al., 2013) showed an average 10.8 ± 5.03 variability when the same tumor was measured multiple (3) times. A way to mitigate these variable results was to zoom in on the region where the ROIs were to be drawn, to minimize the detection and quantification of random pixels near the desired area. In addition, zooming in increases ROI uniformity, which is harder to distinguish with the "regular" or zoomed-out image. In Figure A.1.B, ROIs were drawn on a zoomed-in image, where only one tumor could be seen in the window, which decreased the test-retest reproducibility percent difference

to 3.58 ± 1.98. At lower magnifications, the researcher conducting the analysis could observe distinct and uniform ROIs, but the software detects some differences affected the final ROI measurement. Zooming in to the desired area allows for better construction of ROIs, so the software can measure with higher accuracy.

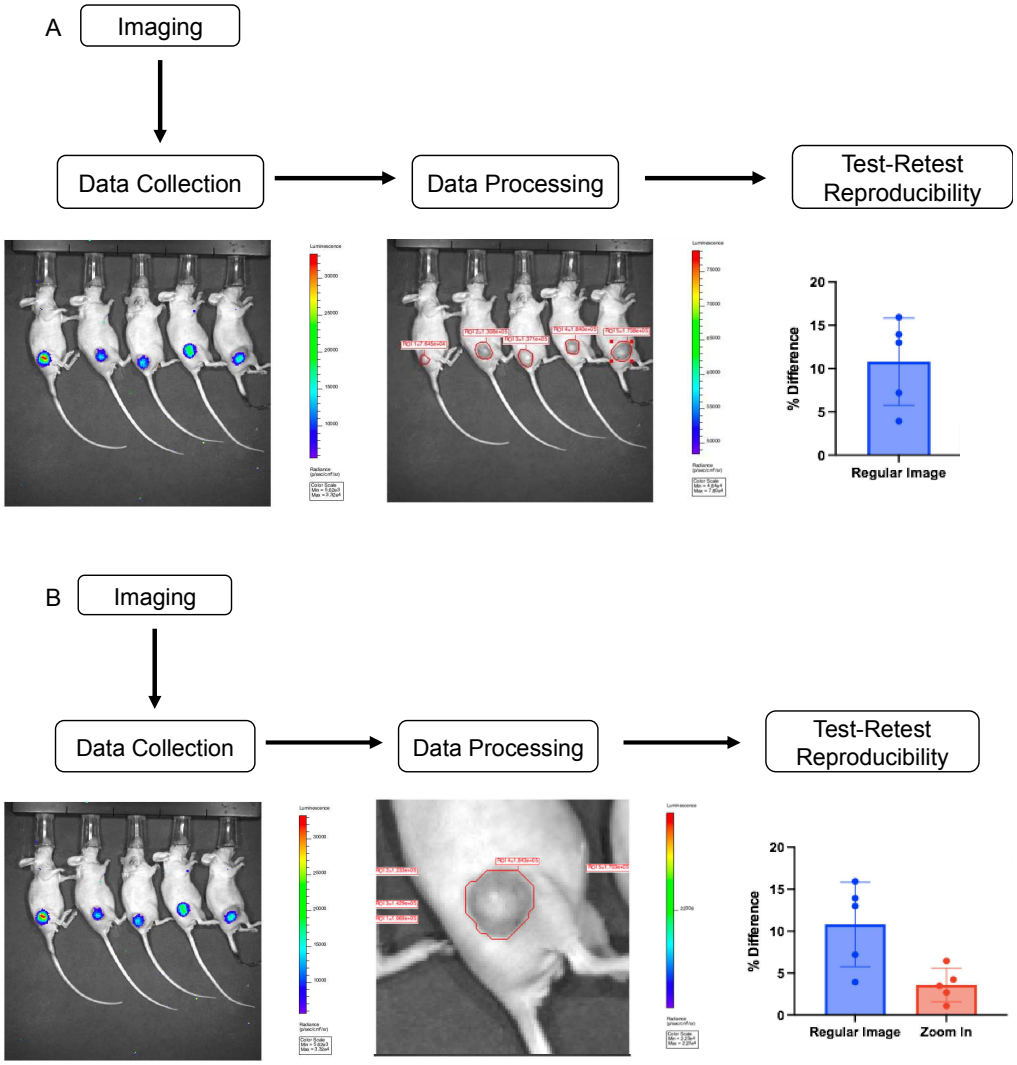

Figure A.1. ROI Test-Retest Reproducibility. *A.* Image analysis scheme after Cerenkov imaging, with ROIs drawn on image obtained from the IVIS Spectrum. *B.* Image analysis scheme after Cerenkov imaging, with ROIs drawn on zoomed in image, focusing on tumor.

A.2. Data Normalization

Cerenkov imaging is multispectral and continuous and can be detected through various filters in the visible region, allowing for the construction of Cerenkov spectra. When NFbD is added, the Cerenkov spectra become pH dependent. Obtaining Cerenkov signals from different filters allows for signal normalization to relevant wavelengths, as seen in Figure A.2. For this project, we identified 3 filters of particular importance: 600 nm, 680 nm, and 840 nm. When the signal is normalized to 600 nm, it is normalized to SBQ. This normalization amplifies pH dependent CRET, aiding in visualization (Figure A.2.B). This normalization also corresponds to the first term in the CRET Ratio equation (Dothager et al., 2010), seen below.

$$\mathrm{CRET}_{700\ \mathrm{nm}} = \frac{\mathrm{Cerenkov{+}Fluorophore}_{700\ \mathrm{nm}}}{\mathrm{Cerenkov{+}Fluorophore}_{600\ \mathrm{nm}}} - \frac{\mathrm{Cerenkov}_{700\ \mathrm{nm}}}{\mathrm{Cerenkov}_{600\ \mathrm{nm}}}$$

The isosbestic point for NFbD is 680 nm, which is why it is considered a relevant filter for normalization, since it is the point where the measurements are pH independent (Jo et al., 2017). Finally, normalization to 840 nm has been done in our previous Cerenkov studies (Arroyo, 2019; Arroyo et al., 2019), which is the longest wavelength measured, outside of the range of fluorescence and where the maximum tissue penetration of light occurs.

Normalization to each of these wavelengths produces changes in Cerenkov spectra that affect the fit of the pH titration curves, which are used to interpolate pH

values. Figure A.2.E-H show representative pH titration curves of NFbD (~74 μCi) normalized to each of the aforementioned wavelengths. The figure legends include the pK_a value, obtained from GraphpadPRISM as the $LogIC_{50}$ after "Sigmoidal, 4PL, X is log(concentration)" analysis, and the corresponding R^2 value (goodness of fit), which was highest at 600 nm normalization.

As previously mentioned, pH determination *in vivo* was done using CRET Ratio calculations, as proposed by Piwnica-Worms, which can potentially correct for tissue effects by subtracting independent Cerenkov signal at SBQ and CRET wavelengths. pH titration curve constructed with CRET Ratios is presented in Figure A.2.I, which shows similar pK_a and R^2 values to 600 nm normalization.

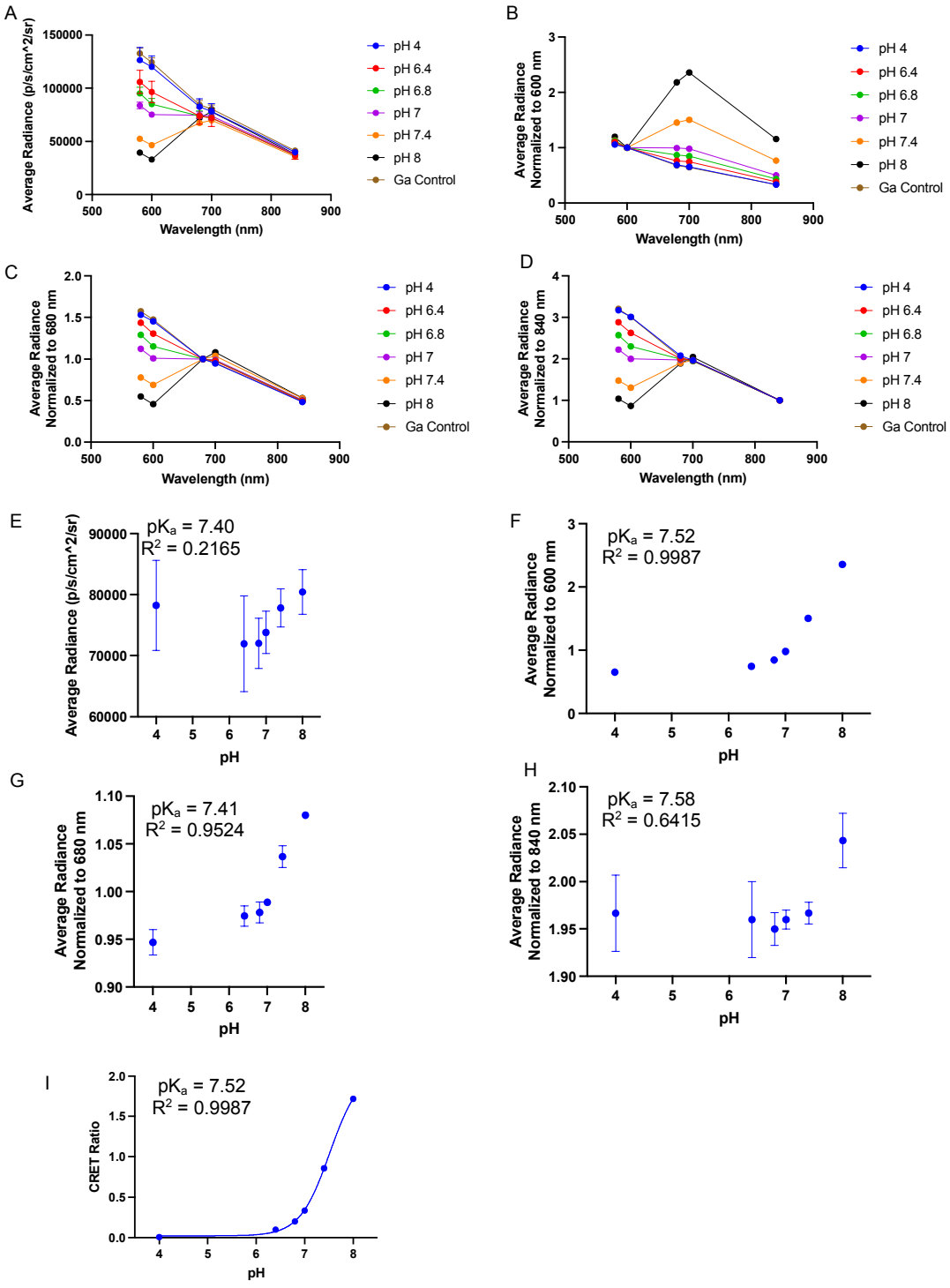

Figure A.2. Cerenkov spectra and pH titration curves. *A-D.* Cerenkov spectra of average radiance signal as a function of wavelength (NFbD ~74 µCi). *A.* Average radiance signal presented without normalization. *B-D.* normalized to 600 nm, 680 nm, and 840 nm, respectively. *E-H.* Corresponding Cerenkov pH titration curves for *A-D*. *I.* Cerenkov pH titration curve calculated using the CRET Ratio equation. Some error bars are smaller than the data points.

A.3. Cerenkov imaging of ^{68}Ga in mice

Imaging of ^{68}Ga was done with mice bearing 4175-Luc+ tumor xenografts, immediately after euthanasia. ^{68}Ga (~40 μCi) was injected intratumorally in each mouse and *in vivo* Cerenkov spectra were obtained (Figure A.3). These data were used as an average for the *in vivo* Cerenkov signal with no NFbD, to calculate CRET ratios *in vivo*, using the Piwnica-Worms method (Dothager et al., 2010).

In Figure A.3 these data are presented as average radiance with no normalization (Figure A.3.A), normalized to 600 nm filter (Figure A.3.b), normalized to 680 nm filter (isosbestic point) (Jo et al., 2017) in Figure A.3.d and normalized to 840 nm (Figure A.3.e). In each of these normalizations, Mice 1 and 4 have decreased signal at 600 nm and show a signal increase at 680 nm, while Mice 2 and 3 do not exhibit this signal difference. This is an important observation, particularly because we have observed similar signal patterns previously in bologna phantoms (Chapter 6). Additionally, Cerenkov imaging at 580 nm show that Mice 2 and 3 have the brightest tumors. Since these tumors were injected with the same activity of ^{68}Ga, it is possible that these changes in signal correspond to depth of injection. A shallower injection would result in less tissue attenuation effects. This was evaluated with the tissue phantoms in Chapter 6, where it was shown that this technique was optimal for superficial applications, given its low depth penetration. Differences in depth of injection provided valuable information, but this variation could be overcome with stereotactic injection systems.

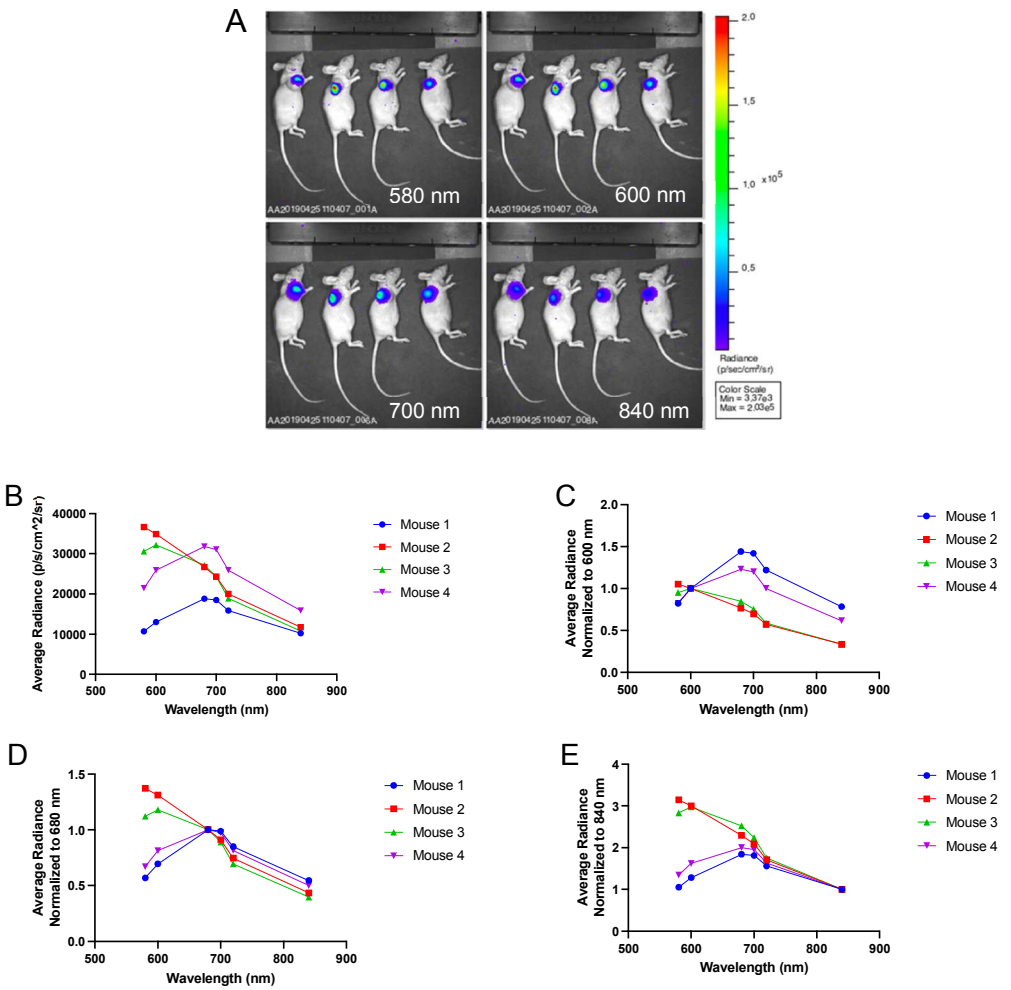

Figure A.3. Mice imaging of ^{68}Ga. *A.* Cerenkov images of euthanized mice bearing 4175-Luc+ tumor xenografts, after ~40 µCi injection of ^{68}Ga. *B-E.* Cerenkov spectra for each mouse in *A*, presented as average radiance as a function of wavelength, normalized to signal obtained at 600 nm filter, 680 nm filter and 840 nm filter or no normalization.

A.4 ^{68}Ga Generator

Throughout this project, the activity obtained from the ^{68}Ga generator exponentially decreased, affecting the number, nature and type of experiments that could be performed. This was challenging, not only because of the decrease in activity but also because of the nature of our Cerenkov emitter, ^{68}Ga, which has a half-life of 68 minutes. This short half-life made it difficult to perform long experiments and to combine other nuclear modalities such as PET scans, prior to or following Cerenkov imaging. In Figure A.4, we present a graph plotting activity obtained from rinsing the generator as a function of time. The red bar represents the period of COVID shutdowns, where experiments were paused. This decrease in activity meant that many post shutdown experiments had to be performed using direct injections of ^{68}Ga and naphthofluorescein, rather than NFbD-^{68}Ga.

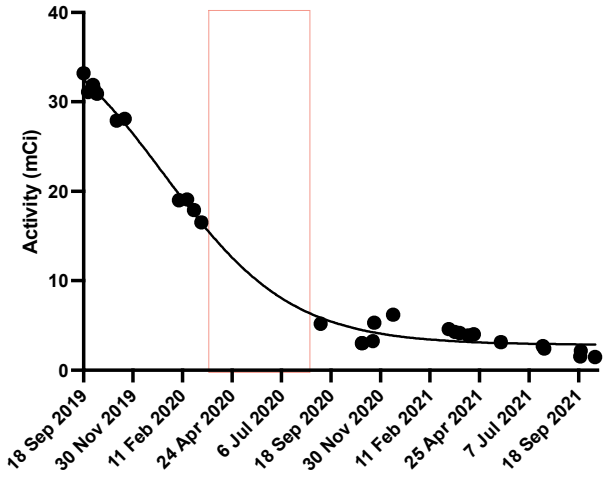

Figure A.4. Activity decrease from ^{68}Ga generator. Activity obtained from generator rinse as a function of time shows exponential decrease in activity.

A.5 Nuclear Magnetic Resonance (NMR)

NMR was done in combination with MALDI-TOF for probe characterization on a Bruker DMX 500. 10 mg of NFbD were dissolved in 600 µL of deuterated water buffered to pH 14 using NaOD. NFbD exhibited aromatic signals, consistent with naphthofluorescein, within the previously observed range of 6.34 ppm - 8.37 ppm (Arroyo et al., 2019). The assignment of these signals, based on our previous publication, is (δ, ppm): 8.35-8.15 (m, 2H, H8 + H6), 7.82-7.30 (m, 2H, H4'+H5'+H6'+H7'), 7.10-6-92, m, 2H, H2+H12), 6.71-6.22 (m, 5H, H7'+H5+H9+H4+H10).

Aliphatic signals were also observed, corresponding to DOTA (3.3 ppm) and the aliphatic linker (1.2 ppm – 1.4 ppm). This area contains signals of solvents and reagents (3.15 -methanol, 3.23 and 0.98 -ethanol, 2.31 and 0.81 triethylamine and 2.45-acetonitrile). Numerous conformations of DOTA (Aime et al., 1997; Csajbók et al., 2004; Kubíček et al., 2010) in NFbD broaden the signals, producing overlapping peaks. A broad multiplet 3.1-2.9, 6H corresponds to NCH2CO2-. Broad multiplets 2.85-2.2 and 2.19-1.7, 14H are resonances of C(O)NCH2 and NCH2CH2N; and broad mutiplets 1.53-1.0, 4H correspond to C(O)NHCH2CH2CH2CH2NHC(O) (Audras et al., 2017).

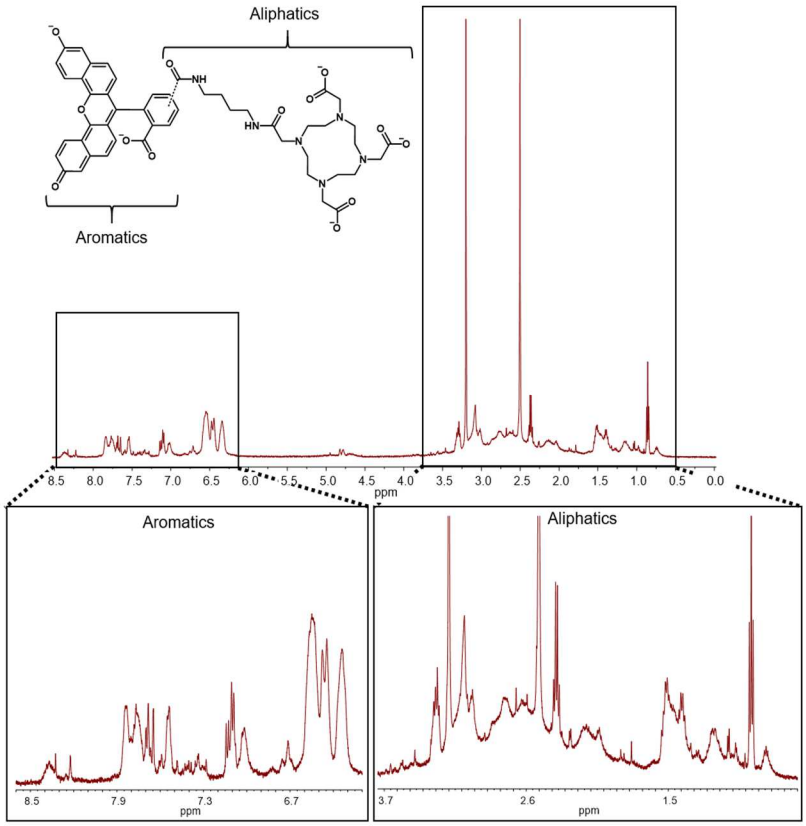

Figure A.5. ^{1}H-NMR spectrum of NFbD (500 MHz, pH 14, D_2O). NFbD has numerous conformations resulting in overlapping signals in the spectrum. Aromatic signals from naphthofluorescein were consistent with the range previously observed (6.34 - 8.37 ppm) (Arroyo et al., 2019). Aliphatic protons were observed between 1.2 and 3.3 ppm with the signals at 3.3 ppm and from 1.2 to 1.4 ppm assigned to the amino acetic acids of DOTA and the central hydrogens of the aliphatic linker respectively.

A.6 Ex Vivo *Protein Immunoblot*

LDHA/LDHB expression had been evaluated *in vitro* with metastatic triple negative breast cancer cell lines MDA-MB-231 and 4175-Luc+. Results showed increased LDHA expression in 4175-Luc+ cell lines, compared to MDA-MB-231 cell lines (Arroyo, 2019). To assess LDHA and LDHB expression in tumors, protein immunoblots (commonly known as Western blots) were performed *ex vivo*. MDA-MB-231 and 4175-Luc+ tumor xenografts were excised from athymic nude mice. These tumors were then homogenized and lysed to perform protein immunoblotting. LDHA and LDHB expression was evaluated against β-tubulin, a housekeeping protein (Figure A.6).

Data suggested that there were no consistent expression patterns of LDHA or LDHB for MDA-MB-231 or 4175-Luc+ tumors, which could be due to tumor xenograft heterogeneity. Although these tumors are expected to develop in a similar fashion, it is likely that they are distinguishable, even when corresponding to the same cell line, particularly because they are injected in individual mice (1 tumor/mouse). Additionally, the tumor microenvironment adds a layer of complexity that is not present *in vitro*, which could relate to *in vitro* LDHA and LDHB expression patterns not translating *in vivo* (Boix-Montesinos et al., 2021). It is also relevant to note that these studies presented some challenges in terms of antibody binding and noise, and future studies should focus on immunohistochemical staining for evaluating expression of these proteins.

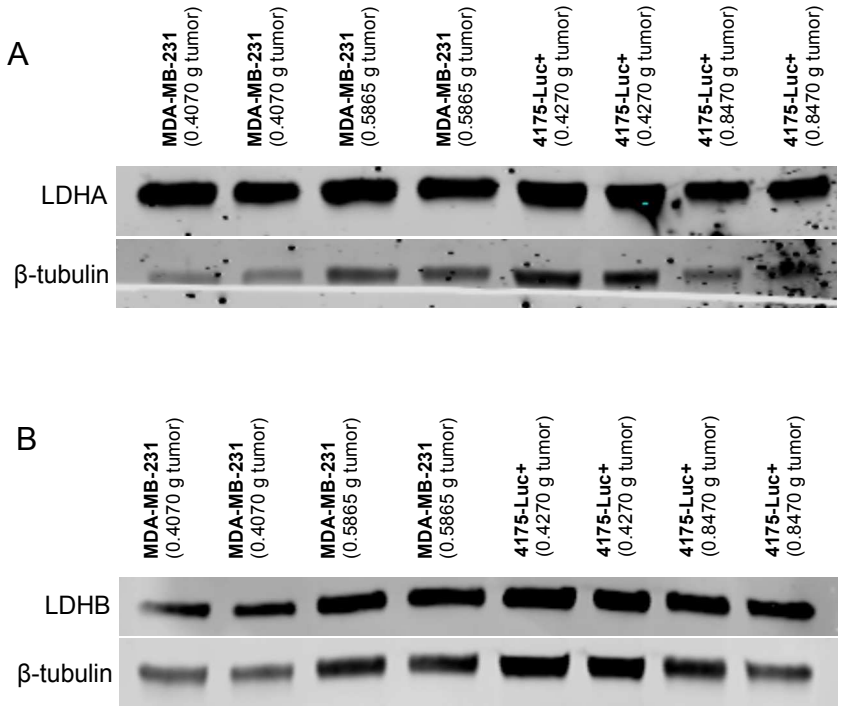

***Figure A.6. Protein Immunoblot for LDHA and LDHB* ex vivo.** Protein immunoblots compared to β-tubulin for 4 tumors, 2 corresponded to MDA-MB-231 xenografts and 2 corresponded to 4175-Luc+ xenografts, samples were loaded in duplicate. *A.* LDHA immunoblot evaluated against β-tubulin. No observable differences between cell lines are detected. *B.* LDHB immunoblot evaluated against β-tubulin. No observable differences between cell lines are detected.

Bibliography

(2022a). Breast Cancer Statistics | How Common Is Breast Cancer? (@cancer.org).

(2022b). MCF7 | ATCC.

(2022c). MDA-MB-231 | ATCC.

(2022d). Naphthofluorescein fluorescence 61419-02-1.

(2022e). The Nobel Prize in Physics 1958.

(2022f). T-47D | ATCC.

Abumanhal-Masarweh, H., Koren, L., Zinger, A., Yaari, Z., Krinsky, N., Kaneti, G., Dahan, N., Lupu-Haber, Y., Suss-Toby, E., Weiss-Messer, E., et al. (2019). Sodium bicarbonate nanoparticles modulate the tumor pH and enhance the cellular uptake of doxorubicin. Journal of Controlled Release *296*, 1-13.

Agnello, L., Tortorella, S., d'Argenio, A., Carbone, C., Camorani, S., Locatelli, E., Auletta, L., Sorrentino, D., Fedele, M., Zannetti, A., et al. (2021). Optimizing cisplatin delivery to triple-negative breast cancer through novel EGFR aptamer-conjugated polymeric nanovectors. Journal of Experimental & Clinical Cancer Research *40*, 239.

Aime, S., Botta, M., Fasano, M., Marques, M.P.M., Geraldes, C.F.G.C., Pubanz, D., and Merbach, A.E. (1997). Conformational and Coordination Equilibria on DOTA Complexes of Lanthanide Metal Ions in Aqueous Solution Studied by 1H-NMR Spectroscopy. Inorganic Chemistry *36*, 2059-2068.

Alexander, D.A., Nomezine, A., Jarvis, L.A., Gladstone, D.J., Pogue, B.W., and Bruza, P. (2021). Color Cherenkov imaging of clinical radiation therapy. Light: Science & Applications *10*.

Alves, F., Bode, J., Cimalla, P., Hilger, I., Hofmann, M., Jaedicke, V., Koch, E., Licha, K., Rademakers, T., Razansky, D., et al. (2017). Optical Imaging. In Small Animal Imaging: Basics and Practical Guide. F. Kiessling, B.J. Pichler, and P. Hauff, eds. (Cham: Springer International Publishing), pp. 403-490.

Anders, C., and Carey, L.A. (2008). Understanding and treating triple-negative breast cancer. Oncology (Williston Park) *22*, 1233-1243.

Anemone, A., Consolino, L., Conti, L., Irrera, P., Hsu, M.Y., Villano, D., Dastrù, W., Porporato, P.E., Cavallo, F., and Longo, D.L. (2021). Tumour acidosis evaluated in vivo by MRI-CEST pH imaging reveals breast cancer metastatic potential. British Journal of Cancer *124*, 207-216.

Applications, A.A. (2022). Full Prescribing Information NETSPOT.

Arlauckas, S.P., Kumar, M., Popov, A.V., Poptani, H., and Delikatny, E.J. (2017). Near infrared fluorescent imaging of choline kinase alpha expression and inhibition in breast tumors. Oncotarget *8*, 16518-16530.

Arranz, A., and Ripoll, J. (2015). Advances in optical imaging for pharmacological studies. Frontiers in Pharmacology *6*.

Arroyo, A. (2019). Activatable Probes for the Imaging of Biological Parameters Using Cerenkov Radiation. In Pharmacology (ProQuest: University of Pennsylvania), p. 124.

Arroyo, A.D., Guzman, A.E., Kachur, A.V., Popov, A.V., and Delikatny, E.J. (2021). Development of 18F-Labeled Resazurin Derivatives for the Detection of Tumor Metabolic Activity Using Cerenkov Imaging. Frontiers in Physics *9*.

Arroyo, A.D., Guzman, A.E., Kachur, A.V., Saylor, S.J., Popov, A.V., and Delikatny, E.J. (2019). Development of fluorinated naphthofluoresceins for Cerenkov imaging. J Fluor Chem *225*, 27-34.

Audras, M., Berthon, L., Berthon, C., Guillaumont, D., Dumas, T., Illy, M.-C., Martin, N., Zilbermann, I., Moiseev, Y., Ben-Eliyahu, Y., et al. (2017). Structural Characterization of Am(III)- and Pu(III)-DOTA Complexes. Inorganic Chemistry *56*, 12248-12259.

Axelsson, J., Davis, S.C., Gladstone, D.J., and Pogue, B.W. (2011). Cerenkov emission induced by external beam radiation stimulates molecular fluorescence. Med Phys *38*, 4127-4132.

Bagguley, D., Cumberbatch, M., Lawrentschuk, N., and Murphy, D.G. (2020). Cerenkov Luminescence Imaging for surgical margins in radical prostatectomy: a surgical perspective. J Nucl Med.

Balagurunathan, Y., Kumar, V., Gu, Y., Kim, J., Wang, H., Liu, Y., Goldgof, D.B., Hall, L.O., Korn, R., Zhao, B., et al. (2014). Test–Retest Reproducibility Analysis of Lung CT Image Features. Journal of Digital Imaging *27*, 805-823.

Baranyai, Z., Tircsó, G., and Rösch, F. (2020). The Use of the Macrocyclic Chelator DOTA in Radiochemical Separations. European Journal of Inorganic Chemistry *2020*, 36-56.

Barbosa, A.M., and Martel, F. (2020). Targeting Glucose Transporters for Breast Cancer Therapy: The Effect of Natural and Synthetic Compounds. Cancers *12*, 154.

Beattie, B.J., Thorek, D.L., Schmidtlein, C.R., Pentlow, K.S., Humm, J.L., and Hielscher, A.H. (2012). Quantitative modeling of Cerenkov light production efficiency from medical radionuclides. PLoS One *7*, e31402.

Bellis, S.L. (2011). Advantages of RGD peptides for directing cell association with biomaterials. Biomaterials *32*, 4205-4210.

Benjamin, D., Robay, D., Hindupur, S.K., Pohlmann, J., Colombi, M., El-Shemerly, M.Y., Maira, S.-M., Moroni, C., Lane, H.A., and Hall, M.N. (2018). Dual Inhibition of the Lactate Transporters MCT1 and MCT4 Is Synthetic Lethal with Metformin due to NAD+ Depletion in Cancer Cells. Cell Reports *25*, 3047-3058.e3044.

Bernhard, Y., Collin, B., and Decreau, R.A. (2014). Inter/intramolecular Cherenkov radiation energy transfer (CRET) from a fluorophore with a built-in radionuclide. Chem Commun (Camb) *50*, 6711-6713.

Bernhard, Y., Collin, B., and Decreau, R.A. (2017). Redshifted Cherenkov Radiation for in vivo Imaging: Coupling Cherenkov Radiation Energy Transfer to multiple Forster Resonance Energy Transfers. Sci Rep *7*, 45063.

Birks, J.B. (1976). Fluorescence Quantum Yield Measurements. J Res Natl Bur Stand A Phys Chem *80A*, 389-399.

Boix-Montesinos, P., Soriano-Teruel, P.M., Armiñán, A., Orzáez, M., and Vicent, M.J. (2021). The past, present, and future of breast cancer models for nanomedicine development. Advanced Drug Delivery Reviews *173*, 306-330.

Boschi, F., Calderan, L., D'Ambrosio, D., Marengo, M., Fenzi, A., Calandrino, R., Sbarbati, A., and Spinelli, A.E. (2011). In vivo (1)(8)F-FDG tumour uptake measurements in small animals using Cerenkov radiation. Eur J Nucl Med Mol Imaging *38*, 120-127.

Carpenter, C.M., Ma, X., Liu, H., Sun, C., Pratx, G., Wang, J., Gambhir, S.S., Xing, L., and Cheng, Z. (2014). Cerenkov luminescence endoscopy: improved molecular sensitivity with beta--emitting radiotracers. J Nucl Med *55*, 1905-1909.

Čerenkov, P.A. (1937). Visible Radiation Produced by Electrons Moving in a Medium with Velocities Exceeding that of Light. Physical Review *52*, 378-379.

Chadar, R., Afsana, and Kesharwani, P. (2021). Nanotechnology-based siRNA delivery strategies for treatment of triple negative breast cancer. International Journal of Pharmaceutics *605*, 120835.

Chen, L.Q., and Pagel, M.D. (2015). Evaluating pH in the Extracellular Tumor Microenvironment Using CEST MRI and Other Imaging Methods. Advances in Radiology *2015*, 206405.

Chiorazzo, M.G. (2016). Activatable fluorophores for the molecular imaging of cytosolic phospholipase A2 in breast cancer.

Chiorazzo, M.G., Bloch, N.B., Popov, A.V., and Delikatny, E.J. (2015). Synthesis and Evaluation of Cytosolic Phospholipase A2 Activatable Fluorophores for Cancer Imaging. Bioconjugate Chemistry *26*, 2360-2370.

Ciarrocchi, E., and Belcari, N. (2017). Cerenkov luminescence imaging: physics principles and potential applications in biomedical sciences. EJNMMI Phys *4*, 14.

Ciarrocchi, E., Saponaro, S., Bartoli, F., Cataldi, A.G., Vitali, S., Erba, P.A., and Belcari, N. (2021). In-vitro Study for Cerenkov Luminescence Imaging Application in Hepatic Metastasectomy. Frontiers in Physics *9*.

Contreras-Baeza, Y., Sandoval, P.Y., Alarcón, R., Galaz, A., Cortés-Molina, F., Alegría, K., Baeza-Lehnert, F., Arce-Molina, R., Guequén, A., Flores, C.A., et al. (2019). Monocarboxylate transporter 4 (MCT4) is a high affinity transporter capable of exporting lactate in high-lactate microenvironments. Journal of Biological Chemistry *294*, 20135-20147.

Costa, E., Ferreira-Gonçalves, T., Chasqueira, G., Cabrita, A.S., Figueiredo, I.V., and Reis, C.P. (2020). Experimental Models as Refined Translational Tools for Breast Cancer Research. Scientia Pharmaceutica *88*.

Csajbók, É., Bányai, I., and Brücher, E. (2004). Dynamic NMR properties of DOTA ligand: variable pH and temperature 1H NMR study on [K(HxDOTA)](3−x)− species. Dalton Transactions, 2152-2156.

Czupryna, J., Kachur, A.V., Blankemeyer, E., Popov, A.V., Arroyo, A.D., Karp, J.S., and Delikatny, E.J. (2015). Cerenkov-specific contrast agents for detection of pH in vivo. J Nucl Med *56*, 483-488.

Dai, X., Cheng, H., Bai, Z., and Li, J. (2017). Breast Cancer Cell Line Classification and Its Relevance with Breast Tumor Subtyping. Journal of Cancer *8*, 3131-3141.

Daniel LJ Thorek, R.R., Wassifa A Bacchus, Jaeseunh Hahn, Julie Rothberg, Bradley J Beattie, Jan Grimm (2012). Cerenkov Imaging- A new modality for molecular imaging. American Journal of Nuclear Medicine and Molecular Imaging *2*, 163-173.

Das, S., Thorek, D.L., and Grimm, J. (2014). Cerenkov imaging. Adv Cancer Res *124*, 213-234.

DeBerardinis, R.J., and Chandel, N.S. (2020). We need to talk about the Warburg effect. Nature Metabolism *2*, 127-129.

DeBerardinis, R.J., Lum, J.J., Hatzivassiliou, G., and Thompson, C.B. (2008). The Biology of Cancer: Metabolic Reprogramming Fuels Cell Growth and Proliferation. Cell Metabolism *7*, 11-20.

Demers, J.L., Davis, S.C., Zhang, R., Gladstone, D.J., and Pogue, B.W. (2013). Cerenkov excited fluorescence tomography using external beam radiation. Opt Lett *38*, 1364-1366.

Desvaux, E., Courteau, A., Bellaye, P.S., Guillemin, M., Drouet, C., Walker, P., Collin, B., and Decreau, R.A. (2018). Cherenkov luminescence imaging is a fast and relevant preclinical tool to assess tumour hypoxia in vivo. EJNMMI Res *8*, 111.

Di Ninni, P., Martelli, F., and Zaccanti, G. (2010). The use of India ink in tissue-simulating phantoms. Opt. Express *18*, 26854-26865.

Di Ninni, P., Martelli, F., and Zaccanti, G. (2011). Effect of dependent scattering on the optical properties of Intralipid tissue phantoms. Biomed. Opt. Express *2*, 2265-2278.

Ding, H., Lu, J.Q., Jacobs, K.M., and Hu, X.-H. (2005). Determination of refractive indices of porcine skin tissues and Intralipid at eight wavelengths between 325 and 1557 nm. J. Opt. Soc. Am. A *22*, 1151-1157.

Dothager, R.S., Goiffon, R.J., Jackson, E., Harpstrite, S., and Piwnica-Worms, D. (2010). Cerenkov radiation energy transfer (CRET) imaging: a novel method for optical imaging of PET isotopes in biological systems. PLoS One *5*, e13300.

Estrella, V., Chen, T., Lloyd, M., Wojtkowiak, J., Cornnell, H.H., Ibrahim-Hashim, A., Bailey, K., Balagurunathan, Y., Rothberg, J.M., Sloane, B.F., et al. (2013). Acidity Generated by the Tumor Microenvironment Drives Local Invasion. Cancer Research *73*, 1524-1535.

Feng, Z., Tang, T., Wu, T., Yu, X., Zhang, Y., Wang, M., Zheng, J., Ying, Y., Chen, S., Zhou, J., et al. (2021). Perfecting and extending the near-infrared imaging window. Light: Science & Applications *10*, 1-18.

Fokong, S., Jayapaul, J., and Kiessling, F. (2014). 4.07 - Multimodal Optical Imaging Probes. In Comprehensive Biomedical Physics. A. Brahme, ed. (Oxford: Elsevier), pp. 73-83.

Frank, I.M., and Tamm, I. (1937). Coherent visible radiation of fast electrons passing through matter. Physics-Uspekhi *93*, 388-393.

Gerweck, L.E., Vijayappa, S., and Kozin, S. (2006). Tumor pH controls the in vivo efficacy of weak acid and base chemotherapeutics. Mol Cancer Ther *5*, 1275-1279.

Habte, F., Natarajan, A., Paik, D.S., and Gambhir, S.S. (2018). Quantification of Cerenkov Luminescence Imaging (CLI) Comparable With 3-D PET Standard Measurements. Mol Imaging *17*, 1536012118788637.

Hamaguchi, R.E.O., Narui, R., and Wada, H. (2020). Effects of Alkalization Therapy on Chemotherapy Outcomes in Metastatic or Recurrent Pancreatic Cancer. Anticancer Research *40*, 873.

Han, J., and Burgess, K. (2010). Fluorescent Indicators for Intracellular pH. Chemical Reviews *110*, 2709-2728.

Hanahan, D. (2022). Hallmarks of Cancer: New Dimensions. Cancer Discovery *12*, 31-46.

Hanahan, D., and Weinberg, A., Robert (2011). Hallmarks of Cancer: The Next Generation. Cell *144*, 646-674.

Hanahan, D., and Weinberg, R.A. (2000). The Hallmarks of Cancer. Cell *100*, 57-70.

Harbeck, N., Penault-Llorca, F., Cortes, J., Gnant, M., Houssami, N., Poortmans, P., Ruddy, K., Tsang, J., and Cardoso, F. (2019). Breast cancer. Nature Reviews Disease Primers *5*, 1-31.

Hashim, A.I., Zhang, X., Wojtkowiak, J.W., Martinez, G.V., and Gillies, R.J. (2011). Imaging pH and metastasis. NMR in Biomedicine *24*, 582-591.

Holland, J.P., Normand, G., Ruggiero, A., Lewis, J.S., and Grimm, J. (2011). Intraoperative imaging of positron emission tomographic radiotracers using Cerenkov luminescence emissions. Mol Imaging *10*, 177-186, 171-173.

Hwang, J., Sullivan, M.O., and Kiick, K.L. (2020). Targeted Drug Delivery via the Use of ECM-Mimetic Materials. Frontiers in Bioengineering and Biotechnology *8*.

Jablonski, A. (1933). Efficiency of Anti-Stokes Fluorescence in Dyes. Nature *131*, 839-840.

Jafary, F., Ganjalikhany, M.R., Moradi, A., Hemati, M., and Jafari, S. (2019). Novel Peptide Inhibitors for Lactate Dehydrogenase A (LDHA): A Survey to Inhibit LDHA Activity via Disruption of Protein-Protein Interaction. Scientific Reports *9*, 1-13.

Jaffe, H.H., and Miller, A.L. (1966). The fates of electronic excitation energy. Journal of Chemical Education *43*, 469.

Jelley, J.V. (1955). Cerenkov radiation and its applications. British Journal of Applied Physics *6*, 227-232.

Jennings, R.E. (1962). ČERENKOV RADIATION. Science Progress (1933-) *50*, 364-375.

Jimenez-Mancilla, N., Isaac-Olive, K., Torres-Garcia, E., Camacho-Lopez, M., Ramirez-Nava, G., and Mendoza-Nava, H. (2019). Theoretical and experimental characterization of emission and transmission spectra of Cerenkov radiation generated by 177Lu in tissue. J Biomed Opt *24*, 1-10.

Jo, J., Lee, C.H., Kopelman, R., and Wang, X. (2017). In vivo quantitative imaging of tumor pH by nanosonophore assisted multispectral photoacoustic imaging. Nature Communications *8*.

Kachur, A.V., Arroyo, A.D., Bryan, N.W., Saylor, S.J., Popov, A.V., and Delikatny, E.J. (2017). Synthesis of pH indicators for Cerenkov imaging by electrophilic substitution of bromine by fluorine in an aromatic system. J Fluor Chem *200*, 146-152.

Kachur, A.V., Popov, A.V., Karp, J.S., and Delikatny, E.J. (2013a). Direct fluorination of phenolsulfonphthalein: a method for synthesis of positron-emitting indicators for in vivo pH measurement. Cell Biochem Biophys *66*, 1-5.

Kachur, A.V., Sardelis, D., Bentzley, C., Popov, A.V., Delikatny, E.J., and Karp, J. (2013b). Synthesis and characterization of fluorinated derivatives of cresolsulfonphthalein. J Fluor Chem *145*, 112-117.

Kao, J., Salari, K., Bocanegra, M., Choi, Y.L., Girard, L., Gandhi, J., Kwei, K.A., Hernandez-Boussard, T., Wang, P., Gazdar, A.F., et al. (2009). Molecular profiling of breast cancer cell lines defines relevant tumor models and provides a resource for cancer gene discovery. PloS one *4*.

Kolosenko, I., Avnet, S., Baldini, N., Viklund, J., and De Milito, A. (2017). Therapeutic implications of tumor interstitial acidification. Seminars in Cancer Biology *43*, 119-133.

Kroemer, G., and Pouyssegur, J. (2008). Tumor Cell Metabolism: Cancer's Achilles' Heel. Cancer Cell *13*, 472-482.

Kubíček, V., Havlíčková, J., Kotek, J., Tircsó, G., Hermann, P., Tóth, É., and Lukeš, I. (2010). Gallium(III) Complexes of DOTA and DOTA−Monoamide: Kinetic and Thermodynamic Studies. Inorganic Chemistry *49*, 10960-10969.

Kutova, O.M., Guryev, E.L., Sokolova, E.A., Alzeibak, R., and Balalaeva, I.V. (2019). Targeted Delivery to Tumors: Multidirectional Strategies to Improve Treatment Efficiency. Cancers *11*, 68.

L'Annunziata, M.F. (2016). Chapter 16 - Cherenkov Radiation. In Radioactivity (Second Edition). M.F. L'Annunziata, ed. (Boston: Elsevier), pp. 547-581.

Lavis, L.D. (2022). Tailoring fluorescent molecules for biological applications - ProQuest. (University of Wisconsin-Madison).

Lavis, L.D., and Raines, R.T. (2008). Bright Ideas for Chemical Biology. ACS Chemical Biology *3*, 142-155.

Le Guern, F., Mussard, V., Gaucher, A., Rottman, M., and Prim, D. (2020). Fluorescein Derivatives as Fluorescent Probes for pH Monitoring along Recent Biological Applications. Int J Mol Sci *21*, 9217.

Lewis, D.Y., Mair, R., Wright, A., Allinson, K., Lyons, S.K., Booth, T., Jones, J., Bielik, R., Soloviev, D., and Brindle, K.M. (2018). [(18)F]fluoroethyltyrosine-induced Cerenkov Luminescence Improves Image-Guided Surgical Resection of Glioma. Theranostics *8*, 3991-4002.

Li, C., Chen, G., Zhang, Y., Wu, F., and Wang, Q. (2020). Advanced Fluorescence Imaging Technology in the Near-Infrared-II Window for Biomedical Applications. Journal of the American Chemical Society *142*, 14789-14804.

Liu, Y., Yu, G., Tian, M., and Zhang, H. (2011). Optical probes and the applications in multimodality imaging. Contrast Media & Molecular Imaging *6*, 169-177.

Lohrmann, C., Zhang, H., Thorek, D.L., Desai, P., Zanzonico, P.B., O'Donoghue, J., Irwin, C.P., Reiner, T., Grimm, J., and Weber, W.A. (2015). Cerenkov Luminescence Imaging for Radiation Dose Calculation of a (9)(0)Y-Labeled Gastrin-Releasing Peptide Receptor Antagonist. J Nucl Med *56*, 805-811.

Luker, G.D., and Luker, K.E. (2008). Optical Imaging: Current Applications and Future Directions. Journal of Nuclear Medicine *49*, 1.

Luo, S.W., Lingyu, M., Ziyuan, W., Huiwen, H., Huilin, C., Zhaojun, D., Yuyang, L., Qin, S., Tsung-Hsien, C., Chong, C., et al. (2021). Lactate Dehydrogenase-A (LDH-A) Preserves Cancer Stemness and Recruitment of Tumor-Associated Macrophages to Promote Breast Cancer Progression.

Mamnoon, B., Loganathan, J., Confeld, M.I., De Fonseka, N., Feng, L., Froberg, J., Choi, Y., Tuvin, D.M., Sathish, V., and Mallik, S. (2021). Targeted polymeric nanoparticles for drug delivery to hypoxic, triple-negative breast tumors. ACS applied bio materials *4*, 1450-1460.

Manon, D., Xiangzhen, X., Nicolas, L., and Thomas, P. (2020). pH-sensitive shortwave infrared quantum dots for In vivo pH mapping (Conference Presentation). In Proc.SPIE.

Manzo-Merino, K.G.d.l.C.-L., Leonardo Josué, C.-M., Diego, O.R.-H., Alejandro, G.-C., and Joaquín (2019). Lactate in the Regulation of Tumor Microenvironment and Therapeutic Approaches.

Martin, M.M., and Lindqvist, L. (1975). The pH dependence of fluorescein fluorescence. Journal of Luminescence *10*, 381-390.

Mathupala, S.P., Ko, Y.H., and Pedersen, P.L. (2006). Hexokinase II: Cancer's double-edged sword acting as both facilitator and gatekeeper of malignancy when bound to mitochondria. Oncogene *25*, 4777-4786.

Minn, A.J., Gupta, G.P., Siegel, P.M., Bos, P.D., Shu, W., Giri, D.D., Viale, A., Olshen, A.B., Gerald, W.L., and Massagué, J. (2005). Genes that mediate breast cancer metastasis to lung. Nature *436*, 518-524.

Mitchell, G.S., Gill, R.K., Boucher, D.L., Li, C., and Cherry, S.R. (2011). In vivo Cerenkov luminescence imaging: a new tool for molecular imaging. Philos Trans A Math Phys Eng Sci *369*, 4605-4619.

Ntziachristos, V. (2006). Fluorescence Molecular Imaging. Annual Review of Biomedical Engineering *8*, 1-33.

Olde Heuvel, J., de Wit-van der Veen, B.J., van der Poel, H.G., Bekers, E.M., Grootendorst, M.R., Vyas, K.N., Slump, C.H., and Stokkel, M.P.M. (2020). (68)Ga-PSMA Cerenkov luminescence imaging in primary prostate cancer: first-in-man series. Eur J Nucl Med Mol Imaging.

Olde Heuvel, J., de Wit-van der Veen, B.J., Vyas, K.N., Tuch, D.S., Grootendorst, M.R., Stokkel, M.P.M., and Slump, C.H. (2019). Performance evaluation of Cerenkov luminescence imaging: a comparison of (68)Ga with (18)F. EJNMMI Phys *6*, 17.

Ooi, A.T., and Gomperts, B.N. (2015). Molecular Pathways: Targeting Cellular Energy Metabolism in Cancer via Inhibition of SLC2A1 and LDHA. Clinical Cancer Research *21*, 2440.

Ottobrini, C.M., Alessia Lo, D., Cecilia, D., Giovanni, L., and Luisa (2016). Optical imaging probes in oncology. 7.

Pavlova, Natalya N., and Thompson, Craig B. (2016). The Emerging Hallmarks of Cancer Metabolism. Cell Metabolism *23*, 27-47.

Peñate Medina, T., Kolb, J.P., Hüttmann, G., Huber, R., Peñate Medina, O., Ha, L., Ulloa, P., Larsen, N., Ferrari, A., Rafecas, M., et al. (2021). Imaging Inflammation – From Whole Body Imaging to Cellular Resolution. Frontiers in Immunology *12*.

Pérez-Tomás, R., and Pérez-Guillén, I. (2020). Lactate in the Tumor Microenvironment: An Essential Molecule in Cancer Progression and Treatment. Cancers *12*.

Po, H.N., and Senozan, N.M. (2001). The Henderson-Hasselbalch Equation: Its History and Limitations. Journal of Chemical Education *78*, 1499.

Pratt, E.C., Tamura, R., and Grimm, J. (2021). Chapter 22 - Cerenkov Imaging. In Molecular Imaging (Second Edition). B.D. Ross, and S.S. Gambhir, eds. (Academic Press), pp. 383-395.

Radić, N., and Prkić, A. (2022). Historical remarks on the Henderson-Hasselbalch equation: its advantages and limitations and a novel approach for exact pH calculation in buffer region. Reviews in Analytical Chemistry *31*, 93-98.

radioactivity.eu.com (2022). Radioactivity : Cherenkov Effect.

Rai, G., Brimacombe, K.R., Mott, B.T., Urban, D.J., Hu, X., Yang, S.-M., Lee, T.D., Cheff, D.M., Kouznetsova, J., Benavides, G.A., et al. (2017). Discovery and Optimization of Potent, Cell-Active Pyrazole-Based Inhibitors of Lactate Dehydrogenase (LDH). Journal of Medicinal Chemistry *60*, 9184-9204.

Rattigan, Y.I., Patel, B.B., Ackerstaff, E., Sukenick, G., Koutcher, J.A., Glod, J.W., and Banerjee, D. (2012). Lactate is a mediator of metabolic cooperation between stromal carcinoma associated fibroblasts and glycolytic tumor cells in the tumor microenvironment. Exp Cell Res *318*, 326-335.

Robertson, R., Germanos, M.S., Li, C., Mitchell, G.S., Cherry, S.R., and Silva, M.D. (2009). Optical imaging of Cerenkov light generation from positron-emitting radiotracers. Phys Med Biol *54*, N355-365.

Senga, S.S., and Grose, R.P. (2021). Hallmarks of cancer—the new testament. Open Biology *11*, 200358.

Soubret, A., and Ntziachristos, V. (2006). Optical Imaging and Tomography. In Textbook of in vivo Imaging in Vertebrates, pp. 149-181.

Spinelli, A.E., and Boschi, F. (2011). Unsupervised analysis of small animal dynamic Cerenkov luminescence imaging. J Biomed Opt *16*, 120506.

Spinelli, A.E., and Boschi, F. (2015). Novel biomedical applications of Cerenkov radiation and radioluminescence imaging. Phys Med *31*, 120-129.

Spinelli, A.E., Ferdeghini, M., Cavedon, C., Zivelonghi, E., Calandrino, R., Fenzi, A., Sbarbati, A., and Boschi, F. (2013). First human Cerenkography. J Biomed Opt *18*, 20502.

Spinelli, A.E., Kuo, C., Rice, B.W., Calandrino, R., Marzola, P., Sbarbati, A., and Boschi, F. (2011). Multispectral Cerenkov luminescence tomography for small animal optical imaging. Opt Express *19*, 12605-12618.

Spinelli, L., Botwicz, M., Zolek, N., Kacprzak, M., Milej, D., Sawosz, P., Liebert, A., Weigel, U., Durduran, T., Foschum, F., et al. (2014). Determination of reference values for optical properties of liquid phantoms based on Intralipid and India ink. Biomed. Opt. Express *5*, 2037-2053.

Tang, Y., Xiao, G., Shen, Z., Zhuang, C., Xie, Y., Zhang, X., Yang, Z., Guan, J., Shen, Y., Chen, Y., et al. (2020). Noninvasive Detection of Extracellular pH in Human Benign and Malignant Liver Tumors Using CEST MRI. Frontiers in Oncology *10*.

Tendler, I.I., Hartford, A., Jermyn, M., LaRochelle, E., Cao, X., Borza, V., Alexander, D., Bruza, P., Hoopes, J., Moodie, K., et al. (2020). Experimentally Observed Cherenkov Light Generation in the Eye During Radiation Therapy. International Journal of Radiation Oncology*Biology*Physics *106*, 422-429.

ThermoFisher (2022a). 5-(and-6)-Carboxy SNARF™-1.

ThermoFisher (2022b). SNARF™-5F 5-(and-6)-Carboxylic Acid.

Thews, O., Gassner, B., Kelleher, D.K., Schwerdt, G., and Gekle, M. (2006). Impact of extracellular acidity on the activity of P-glycoprotein and the cytotoxicity of chemotherapeutic drugs. Neoplasia *8*, 143-152.

Thorek, D., Robertson, R., Bacchus, W.A., Hahn, J., Rothberg, J., Beattie, B.J., and Grimm, J. (2012). Cerenkov imaging - a new modality for molecular imaging. Am J Nucl Med Mol Imaging *2*, 163-173.

Thorek, D.L., Ogirala, A., Beattie, B.J., and Grimm, J. (2013). Quantitative imaging of disease signatures through radioactive decay signal conversion. Nat Med *19*, 1345-1350.

Thorek, D.L., Riedl, C.C., and Grimm, J. (2014a). Clinical Cerenkov luminescence imaging of (18)F-FDG. J Nucl Med *55*, 95-98.

Thorek, D.L.J., Das, S., and Grimm, J. (2014b). Molecular Imaging Using Nanoparticle Quenchers of Cerenkov Luminescence. Small *10*, 3729-3734.

Tomasulo, M., Yildiz, I., and Raymo, F.M. (2006). pH-Sensitive Quantum Dots. The Journal of Physical Chemistry B *110*, 3853-3855.

Upputuri, P.K., and Pramanik, M. (2019). Photoacoustic imaging in the second near-infrared window: a review. Journal of Biomedical Optics *24*, 040901.

Valeur, B., and Berberan-Santos, M.N. (2011). A Brief History of Fluorescence and Phosphorescence before the Emergence of Quantum Theory. Journal of Chemical Education *88*, 731-738.

Vander Heiden, M.G., Cantley, L.C., and Thompson, C.B. (2009). Understanding the Warburg effect: the metabolic requirements of cell proliferation. Science *324*, 1029-1033.

Vaz, S., Falkmer, T., Passmore, A.E., Parsons, R., and Andreou, P. (2013). The Case for Using the Repeatability Coefficient When Calculating Test–Retest Reliability. PLoS ONE *8*, e73990.

Warburg, O., Wind, F., and Negelein, E. (1927). THE METABOLISM OF TUMORS IN THE BODY. J Gen Physiol *8*, 519-530.

Webb, B.A., Chimenti, M., Jacobson, M.P., and Barber, D.L. (2011). Dysregulated pH: a perfect storm for cancer progression. Nature Reviews Cancer *11*, 671-677.

Welsh, J. (2013). Chapter 40 - Animal Models for Studying Prevention and Treatment of Breast Cancer. In Animal Models for the Study of Human Disease. P.M. Conn, ed. (Boston: Academic Press), pp. 997-1018.

Wojtkowiak, J.W., Verduzco, D., Schramm, K.J., and Gillies, R.J. (2011). Drug Resistance and Cellular Adaptation to Tumor Acidic pH Microenvironment. Molecular Pharmaceutics *8*, 2032-2038.

Ždralević, M., Brand, A., Di Ianni, L., Dettmer, K., Reinders, J., Singer, K., Peter, K., Schnell, A., Bruss, C., Decking, S.-M., et al. (2018). Double genetic disruption of lactate dehydrogenases A and B is required to ablate the "Warburg effect" restricting tumor growth to oxidative metabolism. Journal of Biological Chemistry *293*, 15947-15961.

Zhao, M., Wang, J., Lei, Z., Lu, L., Wang, S., Zhang, H., Li, B., and Zhang, F. (2021). NIR□II pH Sensor with a FRET Adjustable Transition Point for In Situ Dynamic Tumor Microenvironment Visualization. Angewandte Chemie International Edition *60*, 5091-5095.

Zhao, Y., Shaffer, T.M., Das, S., Perez-Medina, C., Mulder, W.J., and Grimm, J. (2017). Near-Infrared Quantum Dot and (89)Zr Dual-Labeled Nanoparticles for in Vivo Cerenkov Imaging. Bioconjug Chem *28*, 600-608.